공학박사 학위논문

Photosynthesis inspired hybrid pathway for sustainable carbon dioxide cycle

지속 가능한 이산화탄소 순환을 위한 광합성 모방의 하이브리드 시스템 개발

2019년 2월

서울대학교 대학원

재료공학부

김 영 혜

Abstract

Photosynthesis inspired hybrid pathway for sustainable carbon dioxide cycle

Younghye Kim

Department of Materials Science and Engineering

The Graduate School

Seoul National University

In nature, all free energy utilized by biological systems comes from solar energy that is trapped by photosynthesis. Annually, 4.2×10^{17} kJ of solar energy is harvested by photosynthesis and used in the production of oxygen and glucose from water and carbon dioxide (CO_2). This enables to fix atmospheric CO_2 on the ground as a carbon building block of hydrocarbon and therefore, contributes to sustain the equilibrium of the global carbon cycle. However, since the industrial revolution era, imprudent use of fossil fuel and the resulted CO_2 emission has destroyed the balance in global carbon cycle. To restore the natural energy circulation, new artificial energy storage pathway should be developed. In this

thesis, designating natural photosynthesis as a model system, artificial energy harvesting/conversion systems are newly developed. Each system is inspired from the sequential energy conversion steps in photosynthesis: (1) light harvesting, (2) electron transfer and (3) carbon fixation.

Although the biological system has elaborate design and superior functionality for energy harvesting, it should be reformed to be adopted in artificial devices. First, due to the delicate nature of biomaterials such as proteins, stable synthetic materials should additionally support or replace the biomaterials. Moreover, the final energy or fuel produced from the photosynthetic reaction should be aimed to operate engines rather than metabolize organisms. To build up new strategy for these issues, we have firstly studied previous research on the development of artificial photosynthesis. The representative examples of artificial photosynthesis systems are presented in Chapter 2 which includes the development of artificial light harvesting complexes, artificial electron transfer system and electrochemical CO_2 fixation. After learning lessons from the previous studies, we have designed three novel energy conversion pathways inspired from photosynthesis for the production of valuable fuels. The respective systems are specifically presented in Chapter 3, Chapter 4 and Chapter 5.

Photosynthesis initiates by light absorption at photosynthetic proteins, photosystem. The protein is comprised of light harvesting complex and reaction center where light harvesting complex absorbs solar light and transfer the photon energy to reaction center. Here, the effective construction of dye assembly in photosystem determines the overall light absorption property and photo-energy transfer efficiency. Inspired from the elaborate alignment of these dye assembly, we

newly developed porphyrin-dye based light harvesting complex on the silica-coated gold nanoparticle templates. To precisely align dyes in atomic level, peptoid scaffolds were used which carry out a role of branch on the nanoparticle surface. The intermolecular distance between porphyrins were controlled from 6 Å to 12 Å which is in the range of chlorophyll distance in natural light harvesting complex. We also utilized surface plasmon effect of gold nanoparticle core to amplify the fluorescence of dye. As a result, the fluorescence could be enhanced up to ~20 times at the optimal condition which facilitated to analyze optical property of light harvesting complex more precisely. In detail, distinctive fluorescence spectra were observed from different porphyrin intermolecular alignments. This indicates the developed light harvesting complex can be used as platform for the investigation of intermolecular energy transfer in dye assemblies.

Followed by light absorption, collected light energy is consumed in electron excitation at the reaction centers. The excited electrons are then transferred via Z-scheme which is composed of two photosystem proteins and participates in the water oxidation at photosystem II and NADP reduction at photosystem I. By using step-wise excitation of electrons, the overall redox process can be derived by low-energy light in visible-IR range. In artificial Z-scheme, semiconductors are used instead of photosystems which can replace the role of photocatalyst. The semiconductor materials are selected based on the energy level for the desired redox reaction and efficient electron transfer. In this thesis, newly developed hybrid Z-scheme of photosystem I and semiconductor is demonstrated. The hybrid Z-scheme was constructed in all-solid-system by using Au or Ag mediator to conjugate photosystem I and $BiVO_4$. The system produced hydrogen from water

under visible light. The hydrogen evolution activity and stability of the photocatalytic reaction was both enhanced significantly compared to the case of single excitation system of photosystem I using chemical reductant. We believed that our hybrid Z-scheme exhibited the high performance due to the stable hybrid structure between the inorganic template and protein.

In photosynthesis, CO_2 fixation for glucose synthesis occurs lastly by using electrochemical energy produced from light dependent reaction. In artificial electrochemical devices, CO_2 can be directly reduced by applied potential. As a result, it can be directly converted into valuable fuels or inserted into hydrocarbon feedstocks by carboxylation to make value-added fuels. In this thesis, inspired from the carbon fixation in photosynthesis, new platform for the carboxylation of unsaturated hydrocarbon substrate using CO_2 presented. Instead of using chemical reductant as natural system, electrochemical method was used for stable, fast and mass production of fuel. As a result, site-selective carboxylic acids were produced from the carboxylation of unsaturated hydrocarbons such as styrenes, dienes and α-olefins by using CO_2 and water as carbon and proton source. We envision that the electrochemical platform will aid to open new carbon fixation pathway by producing valuable hydrocarbon fuels from CO_2 and water.

In conclusion, hybrid energy pathway for sustainable carbon fuel cycle was developed in this thesis. The design and concept of system is based on natural photosynthesis, but the virtual construction was modified and upgraded by using hybrid materials from both biological and synthetic materials. Consequently, we could achieve synergetic effect from the hybrid system in the aspect of amplified activity and stability of the complex or device compared to the biological system.

This study will aid understanding the underlying material science in photosynthesis and further exploit the desired fuel production reactions. We also envision that this study will be extended to excellent artificial photosynthesis where the light reaction and dark reaction are combined together.

Key words: Artificial photosynthesis, Photosynthesis, Water splitting, CO_2 conversion, Carbon Cycle, Electrochemistry

Student Number: 2013-20587

Contents

List of Tables

List of Figures

Chapter 1. Introduction

1.1 Global Carbon cycle

Carbon dioxide (CO_2) is the representative greenhouse gas which has the largest contribution to the global climate change. Over the past century, the concentration of CO_2 have dramatically increased and accelerated global warming. Indeed, according to the Global monitoring division from Earth system research laboratory (www.esrl.noaa.gov/gmd), concentration of CO_2 have increased by 40% from 278 ppm in 1750 to 406.99 ppm in 2018 with the growth rate of 2 ppm/year in the last 10 years. The atmospheric CO_2 amount recorded since 1960 is shown in **Figure 1.1**. As it is turned out that the dramatic rise of CO_2 has been resulted from human activities since the industrial revolution, movements to reduce the CO_2 emission has emerged in international society.

The first climate agreement was Kyoto Protocol set in 2008. The countries under Kyoto Protocol complied the target by reducing CO_2 emissions or through use of the Kyoto Protocol's "flexible mechanisms" by which industrialized countries can earn emission credits from emissions reduction projects in participating developing countries and economies in transition (EITs). In December 2015, Paris agreement was adopted in the international community. Here, climate agreement was extended to both developed and developing countries. However, it is still far insufficient to stop the catastrophic change resulted from CO_2 only by reducing the emission quantity.

On earth, natural carbon cycle exists which can maintain the balance of the carbon in ecological system. **Figure 1.2** shows simplified scheme of carbon cycle before (black arrow) and after (red arrow) the industrial era.[1] The most of the carbon in the atmosphere is gaseous CO_2, and it can be fixed on the ground by changing the form into hydrocarbons or minerals. Through various pathways in carbon cycle, the amount of carbon in the atmosphere, ocean and ground keep a balance. However since the industrialization, tremendous amount of carbon has been newly emitted to the atmosphere and induced severe imbalance of the carbon cycle. Particularly, the contribution of carbon emission from the fossil fuel is significantly massive, where 7.8×10^{15} g of carbon are annually generated.[2] While the usage of carbon fuel has been developed dramatically, new pathway for carbon storage from atmosphere to the ground has been never developed.

In the natural carbon cycle, photosynthesis is the only existing carbon storage pathway that can directly convert gaseous CO_2 into hydrocarbons on the ground. This process captures the largest amount of gaseous carbon among the overall pathways on earth including ocean gas exchange. Photosynthesis is powerful strategy to fix the carbon not only due to its large contribution but also because it can produce valuable fuels. In this regard, it is an excellent model system for developing new carbon storage pathway. The lessons from the photosynthesis can provide insights to construct artificial energy conversion systems in the aspect of material design, structure engineering and mechanistic study.

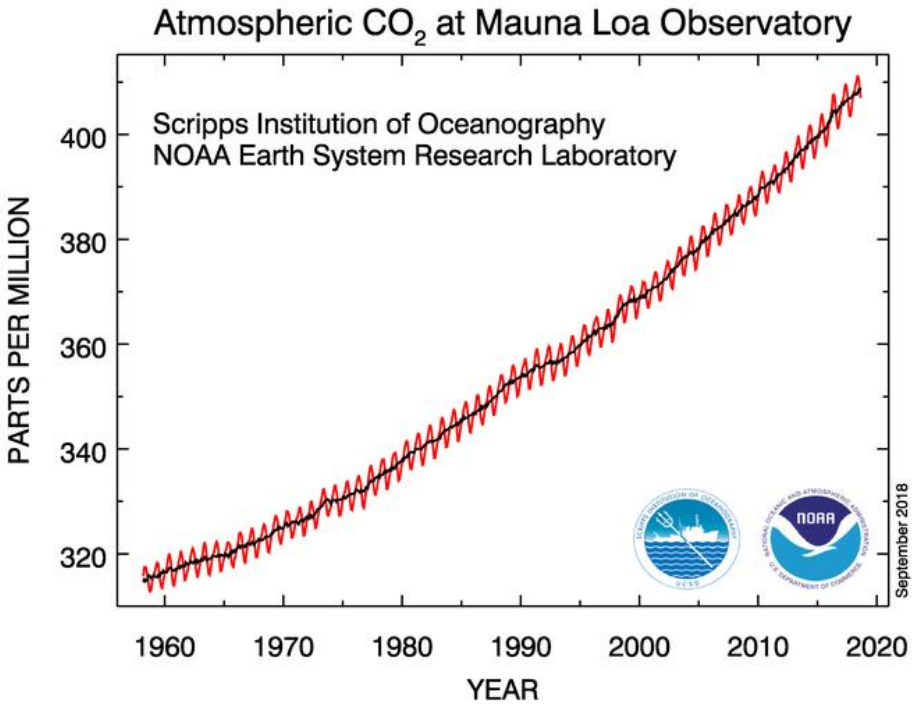

Figure 1.1. Monthly mean atmospheric carbon dioxide at Mauna Loa Observatory, Hawaii. The red curve is carbon dioxide data (red curve), measured as the mole fraction in dry air and the black curve represents the seasonally corrected data. Reprint from

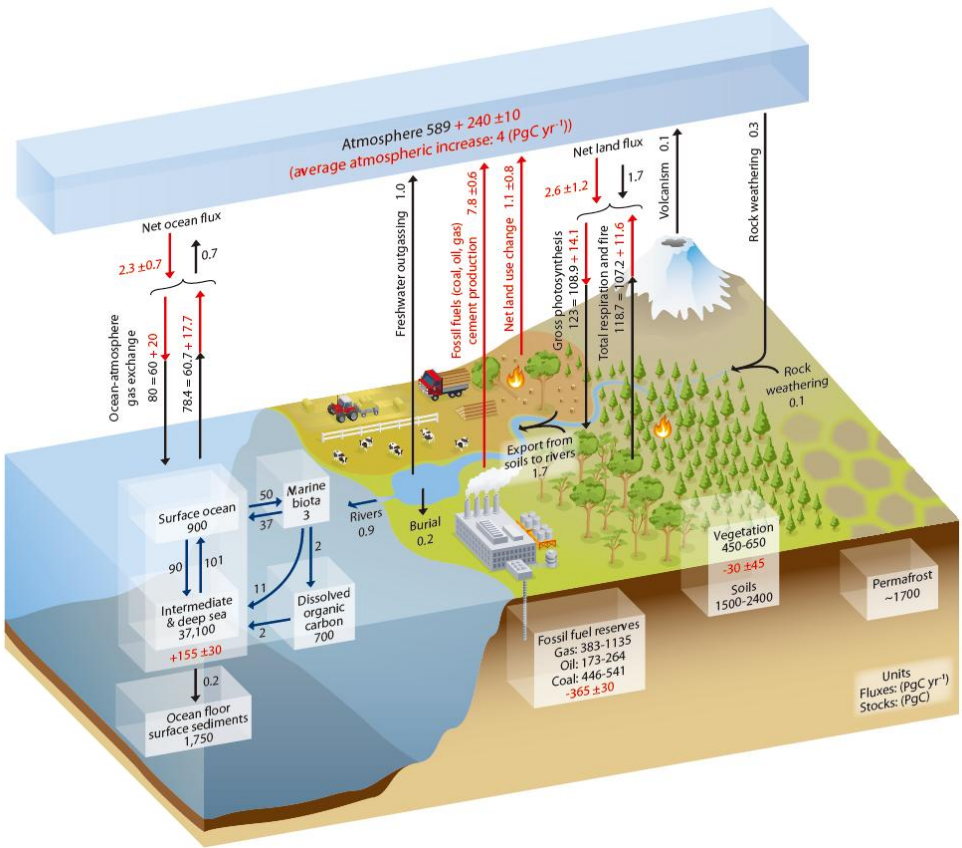

Figure 1.2. The scheme of carbon cycle. The black numbers and arrows indicate reservoir mass and exchange fluxes estimated for the time prior to the Industrial Era. The red numbers and arrows indicate annual fluxes averaged over the 2000-2009 time period.

1.2 Role of photosynthesis in sustainable energy storage

Photosynthesis is the only existing light-driven energy harvesting and conversion process in nature. The annual energy trapped by photosynthesis is approximately 4.2 x 10^{17} kJ where the energy is mostly used in fixation of CO_2 to hydrocarbon fuels. The process carry out in living organisms as plants, cyanobacteria and some primitive bacteria. Plants and cyanobacteria undergo oxygenic photosynthesis, the most typical photosynthetic reaction. Here, glucose and oxygen are produced from CO_2 and water under sunlight. Few bacteria species as green sulfur bacteria, purple bacteria, acidobacteria and heliobacteria perform anoxygenic photosynthesis where H_2S or other organic compounds are utilized instead of water, thus do not evolve oxygen during photosynthesis.[3] In this thesis, photosynthesis mainly indicates oxygenic photosynthesis.

The net photosynthesis can be expressed as follows.

$$6CO_2 + 6H_2O + \text{light energy} \rightarrow C_6H_{12}O_6 + 6O_2$$

This process occurs in two steps: the light dependent reaction and the dark reaction. The light dependent reaction occurs in the thylakoid membrane and produces a reducing power (Reduced nicotinamide adenine dinucleotide phosphate, NADPH) and phosphate bond energy (adenosine triphosphate, ATP) under sunlight. The generated biochemical energy is utilized in dark reaction to capture CO_2 through Calvin cycle and produce glucose.

From the perspective of an energy cycle, photosynthesis can be divided by three sequential processes: light harvesting, electron transfer and carbon storage.

Figure 1.3 shows the simplified scheme of the processes. Through these energy transformations, the overall photosynthesis can be described as the process of energy conversion from light, through electrical energy and chemical energy, to hydrocarbon fuel. In plants, the chloroplast is the principle organelle that conducts net photosynthesis. Its interior consists of piled thylakoid membranes where the photosynthetic proteins that participate in the light reaction are tightly embedded, and the exterior is called the stroma, where the dark reaction takes place. The systematically constructed organs connects each energy converting processes effectively.

The efficiency of each energy conversion steps are also reported.[4] First, 37% of sunlight is harvested as useful photon energy, 76% of photon energy is converted to biochemical energy through electrical energy, and 32% of biochemical energy is used to synthesize glucose from CO_2. Taken together, the net efficiency of photosynthesis in plant is approximately 5.4%, however, each energy conversion process has appreciable efficiency. Each reaction steps of photosynthesis will be described in detail in the following parts.

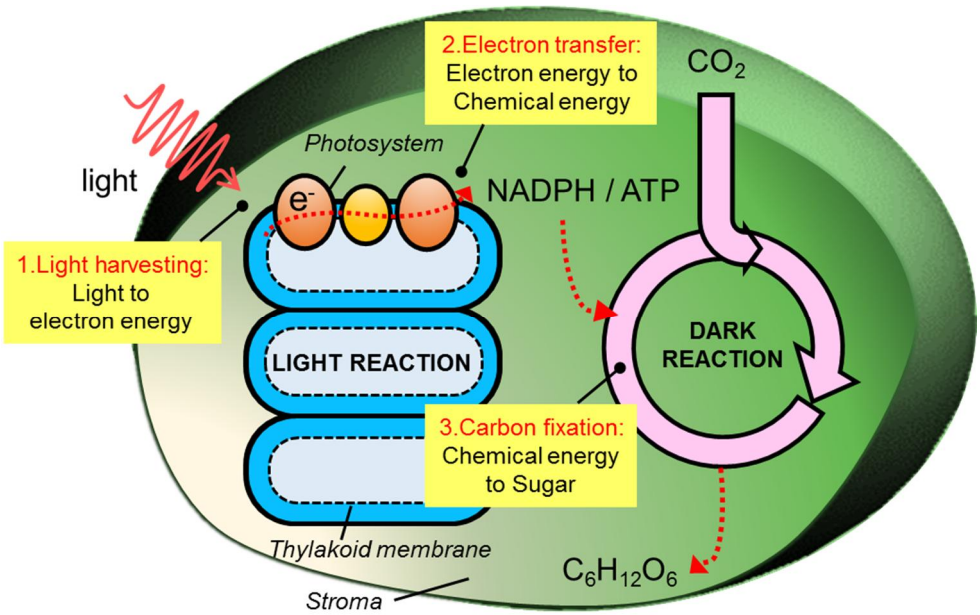

Figure 1.3. Scheme of three steps in photosynthesis: light harvesting, electron transfer and carbon fixation

1.3 Light dependent reaction

Light dependent reaction takes place via series of photosynthetic proteins packed in the thylakoid membrane. Photosynthetic proteins are composed of reaction center (RC) and light harvesting complex (LHC). Here, LHCs absorb solar light and concentrate this energy to RCs. Then at the RC, the positive and negative charge is separated across the thylakoid membrane where the hole participates in water oxidation and excited electrons are consumed in NADP reduction. The composition and type of RC and LHC varies from species to species. As illustrated in **Figure 1.4**, plants, cyanobacteria and anoxygenic photosynthetic bacteria have different types of or compositions of photosynthetic proteins. Plants have two types of RCs, photosystem I (PSI) and photosystem II (PSII), and two types of LHCs, light harvesting complex I (LHCI) and light harvesting complex II (LHCII). Cyanobacteria have the same RC as plants, PSI and PSII, but a large LHC, which is called a phycobilisome. Anoxygenic photosynthetic bacteria have only one type of RC called bacterial RC and generally two types of LHCs called light harvesting complex I (LHI) and light harvesting complex II (LHII).

The light harvesting process is the first step in photosynthesis which directly leads to charge separation at the reaction center photosystems. The antenna of the photosynthetic system has evolved to absorb sufficient sunlight and effectively concentrate the collected energy in the reaction center. The ingeniously arranged natural pigments supported by a large protein complex teach us an essential lesson for a well-made light harvesting system. In nature, the overall light harvesting takes place in a light harvesting complex that is mainly composed of organic pigments. Because the main output of solar irradiance is in the visible and

near IR region, the absorbance spectrum of photosynthetic pigments mostly falls within this range. Nature has chosen chlorophyll as a prime building block of the light harvesting complex, and it exhibits optimized absorption properties for the solar spectrum, supported by other accessory pigments. The pigments collectively assemble into the light harvesting complex and ultimately play a role as an antenna, transferring energy to the reaction center to induce charge separation.

Chlorophyll is the major photosynthetic pigment in the natural light harvesting complex. It has a porphyrin ring with a magnesium ion at its center, and its absorption spectrum is tuned depending on the substituents of the structure and the chemical bond saturation. Chlorophyll a is the main component in universal organisms, and it also acts as a primary donor pair for the reaction center of photosystems. The absorption range of chlorophyll encompasses most of the spectrum of visible light but shows an absence of absorption between 500 nm and 600 nm, which makes the pigment green. This 'green gap' is filled by other accessory pigments such as carotenoids and phycobilins.[5]

When the pigments reach the excitation state by absorption, the excited energy is immediately transferred to other adjacent pigments and ultimately collected in the reaction center. To retain the optimal energy pathway, the pigment molecules are positioned to keep a proper arrangement with nearby molecules. The classical mechanism for excited energy transfer is based on Forster resonance energy transfer (FRET), which is derived from electric dipole-dipole interactions between molecules. Herein, an exciton from a donor molecule hops to an adjacent acceptor at a speed proportional to R^6 (R, distance between two pigments). However, recent studies have repeatedly raised the objection that the extremely fast

energy transfer cannot rely solely on FRET. Additionally, Engel et al. observed crucial evidence of quantum coherence for the energy transfer in the antenna of green sulfur bacteria in 2007.[6] Since then, quantum coherence has been suggested as a rational strategy for efficient energy transfer in the photosynthetic antenna. Coherently oscillating excitons can travel over molecules as a huge wave and provide very fast energy transfer in less than 1 ps.[7] There is still a need to clarify the energy transfer mechanism in the photosynthetic antenna, but the distinct lesson is that three-dimensional arrangement of the pigments regulates the intermolecular force that controls the net energy transfer.

In biological system, protein is the template of the antenna that supports the pigments in the complex. Therefore, the pigments can be stably fixed into the desired arrangement for the optimal energy absorption and transfer. Integrated with protein, chlorophylls maintain an average neighbor distance of 1 nm and form a particular shape and size of the light harvesting complex that avoids quenching but facilitates energy transfer.[8] The protein scaffold also dominates the net absorption wavelength. By organizing the pigments diversely with a specific protein scaffold, the absorption wavelength can be easily tuned, and this is one of the survival strategies of photosynthetic organisms to secure sufficient light in varying situations. The branched residues of the protein scaffold can directly interact with pigments by the formation of hydrogen bonds or the stabilization of the pigment.[9] Thus, the interaction of the proteins and the pigments is the main factor in the construction of the light harvesting complex in nature.

The ultimate function of the light reaction of photosynthesis is to convert light energy into chemical energy that can be used in the metabolism of the

organism. Following the photo-induced charge separation in the reaction center of the photosystems, the excited electrons move through the photosystem and generate a chemical reductant. Although the electron transfer pathway is vary between oxygenic and anoxygenic photosynthesis as illustrated in **Figure 1.5**, the final product from both process is the biochemical reductant. The electron-to-chemical energy conversion model has inspired the development of various electrochemical energy devices adapted to man's demand.

In oxygenic photosynthesis, the step-wise excitation of electrons occurs in two consecutive RCs called photosystems, derived from light harvesting. These photosystems are membrane-intrinsic proteins that are composed of 10-20 subunits. The electrons excited from photosystem II (PSII) transfer to photosystem I (PSI) by electron mediators, including quinones and cytochromes, and are re-excited in PSI to be used in the reduction of $NADP^+$ into NADPH. The two-step excitation enables the electrochemical energy conversion from only water and mild visible light (680 nm for PSII excitation, 700 nm for PSI excitation).[10] The electron transport chain is called the Z-scheme, a typical electron pathway comprising step-wise excitation using relatively low energy.

Z-schematic electron transport takes place in the thylakoid membrane, where all photosystems and electron carriers are contiguously inserted. Herein, the adjacent carriers possess a suitable redox potential to accept and pass over the electrons so that they can travel through the long distance of the thylakoid membrane.[10] Because protein has a particular position that accepts and donates electrons, unlike isotropic inorganic materials, the alignment direction of the protein and carrier molecules also affects the electron transfer efficiency.

ATP is another essential source of biochemical energy produced via the Z-scheme along with NADPH. While $NADP^+$ directly accepts an excited electron via the Z-scheme, ATP synthesis is derived from the proton gradient over the thylakoid membrane generated during the electron transport. Protons are generated during the water oxidation at the Mn cluster of PSII and during the redox electron transfer at plastoquinone.[11, 12] Because the protons are only released to the interior side of membrane, the accumulated protons induce a pH gradient, acidic interior and basic stroma, which is the driving force of proton pumping at ATP synthase.[13] Finally, ATP is synthesized using the proton pumping and utilized as biochemical energy with NADPH in the dark reaction to produce final hydrocarbon fuel.

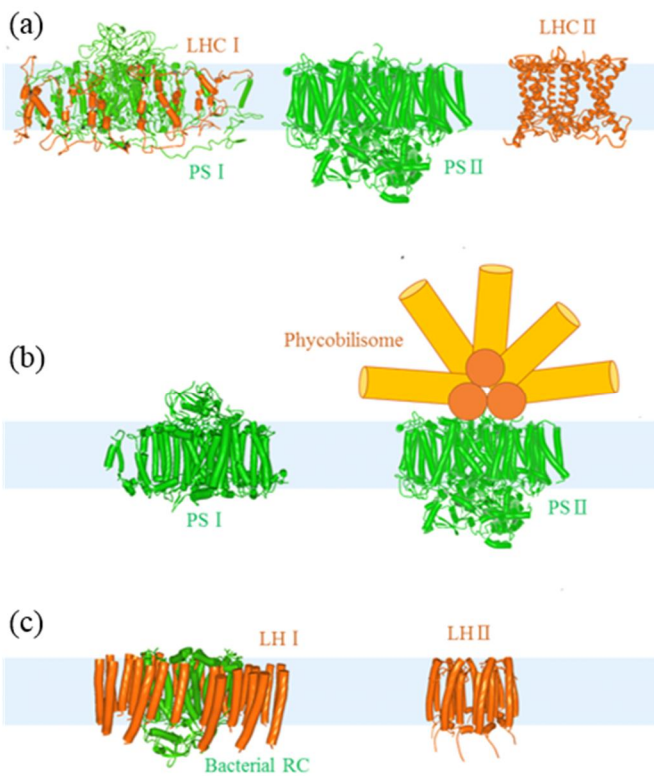

Figure 1.4. Type of reaction centers and light harvesting complex proteins in (a) plants, (b) cyanobacteria and (c) anoxygenic photosynthetic bacteria.

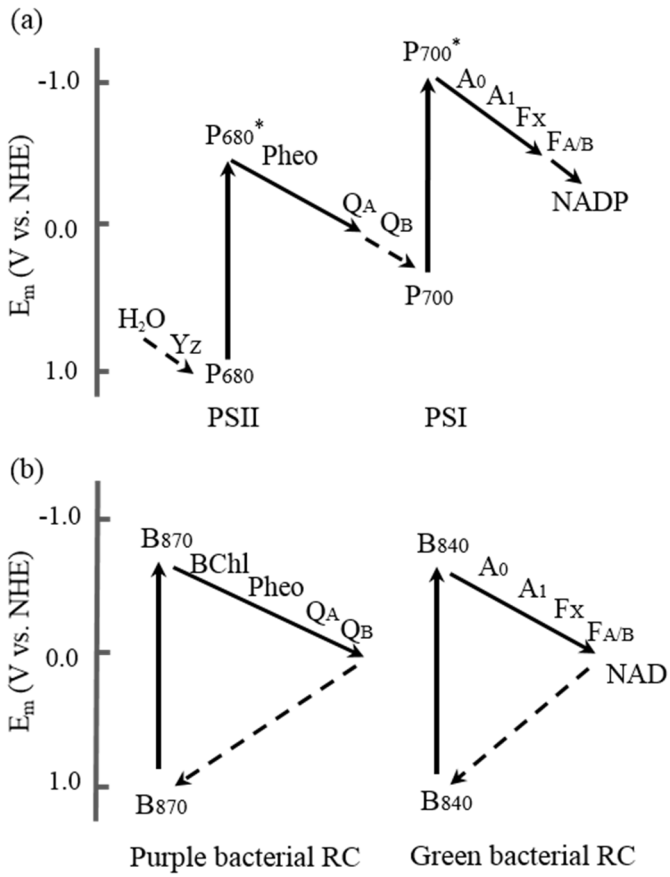

Figure 1.5. The redox potential diagram of electron transfer cofactors in reaction centers of (a) oxygenic photosynthesis and (b) anoxygenic photosynthesis.

1.4 Dark reaction

Concurrently with the light dependent reaction in the thylakoid membrane, the dark reaction proceeds in the stromal region. As it directly utilizes the biochemical energy produced from the light reaction (NADPH and ATP), it also occurs during the daytime, although it is called the 'dark' reaction. The net reaction consists of three cyclic sequential steps: carbon fixation, reduction and regeneration of ribulose. Overall, it is called the 'Calvin cycle', in which three carbon dioxide and five water molecules are converted into a 3-carbon sugar, a half molecule of glucose ($3CO_2$ + 6NADPH + $5H_2O$ + 9ATP → glyceraldehyde-3-phosphate (G3P) + $2H^+$ + 6NADP+ + 9ADP + $8P_i$). The simplified scheme of Calvin cycle is presented in **Figure 1.6**.

Carbon fixation is the first process in the Calvin cycle, in which the carboxylation of a 5-carbon compound, ribulose, into a 6-carbon compound proceeds by the insertion of CO_2. Herein, an enzyme called Rubisco facilitates CO_2 binding and induces carboxylation at its active site.[14] The detailed structure of the active site and the form of intermediate are illustrated in **Figure 1.7**.[15] Due to the effective binding of enediolate intermediate on the active site of Ribulose, the reactivity with CO_2 can be enhanced. The intermediate then underdoes carboxylation reaction at the unsaturated carbon bond and form new carboxylate group which finally leads to 6-carbon product (**Figure 1.8**). This compound immediately splits into two 3-carbon compounds due to its structural instability and is chemically reduced by ATP and NADPH in the following steps. The water molecules are also utilized as proton source during the cyclic processes. Finally, the reduced form of the carbons is regenerated into ribulose, the 5-carbon starting

compound for carbon fixation, through several chemical synthetic processes, which completes the cycle.

The fixation of CO_2 by Rubisco is indispensable for the production of almost every form of bioenergy, but at the same time, it is the limiting step in the Calvin cycle. Rubisco is one of the most abundant enzymes existing on earth and is the primary contact point for fixing inorganic carbon. Despite its significant function, the efficiency is low, limiting that of the net cycle. Because its active site also accepts oxygen as a substrate and catalyzes photorespiration, the net carboxylation is suppressed.[14, 16] Thus, the activity is highly sensitive to the cellular gas concentration and is also regulated by other factors including temperature, water stress and ion concentration.

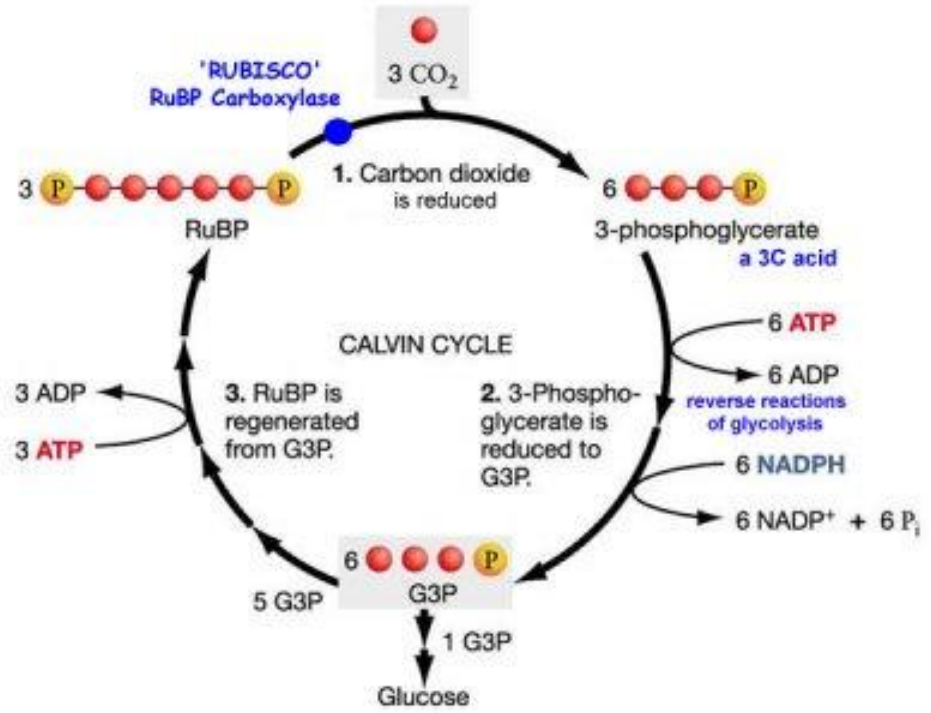

Figure 1.6. Calvin cycle.

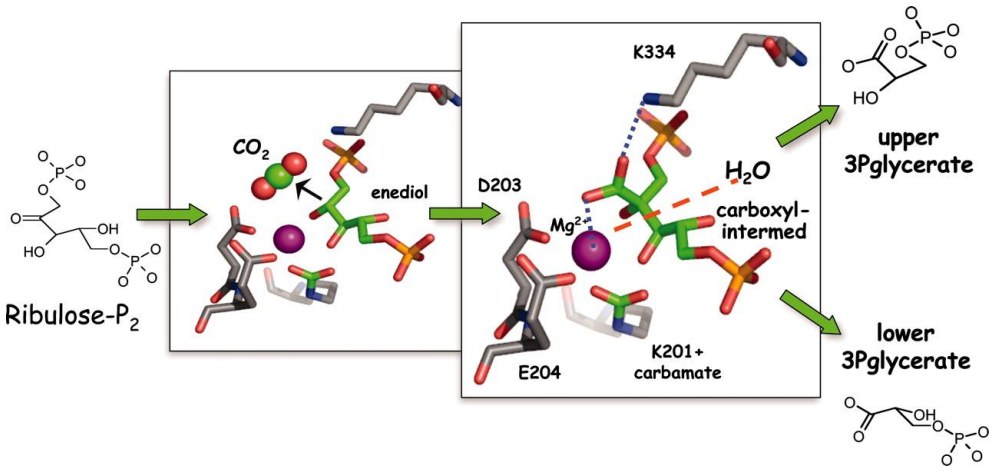

Figure 1.7. Carbon fixation at Rubisco in Calvin cycle.[15]

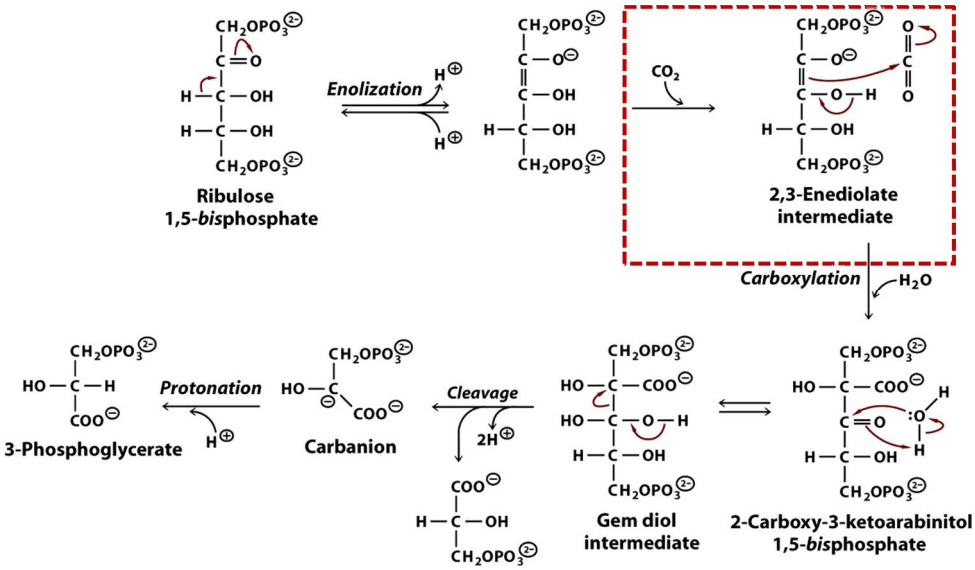

Figure 1.8. Carboxylation process in Calvin cycle.

1.5 Scope of the thesis

From the natural photosynthesis, valuable lessons can be achieved in the aspect of material engineering and energy transformation. First, biological system utilizes elaborately structured protein as a main material to stabilize overall system and facilitate desired catalytic reactions. Light harvesting complex is one of the good example. The chlorophyll pigment molecules are precisely organized inside the protein scaffold to form effective conformation for energy transfer. This conformation is designed in few angstrom (Å) scale which in the intermolecular distance and alignment determines the efficiency of the energy transfer. Oxygen evolving complex (OEC) is another example where the water oxidation take place. The OEC is composed of manganese atoms and located inside the PSII.[12] Its outstanding oxygen evolving activity has attracted numerous researchers studying water splitting catalysts. Until now, many works have been progressed in the basis of mimicking the structure of OEC to develop synthetic oxygen evolution reaction catalysts.

Next, sequential energy transformation processes occur during photosynthesis: Light to electrical energy, electrical energy to chemical energy and finally to hydrocarbon fuel synthesis. Each step is an excellent model for sustainable energy cycle which can be applied to artificial devices. Dye sensitized solar cell is one of the representative light-to-electron energy conversion system inspired from the light dependent reaction of photosynthesis.[17] Moreover, the Z-schematic electron transfer via photosystems enabled to develop artificial Z-scheme for water splitting, CO_2 reduction and chemical pollutant clarification.[18]

However, although these fascinating features in natural photosynthesis can give inspirations, adopting the lessons to artificial device is still challenging. Whereas natural system is based on organic materials and aimed to precise metabolism reactions, we should develop practical and mass scale energy device using organic/inorganic materials. To overcome the differentials, new strategy in designing the system is necessary.

In the thesis, three energy harvesting/conversion system are developed inspired from the three energy harvesting/conversion process in natural photosynthesis. Prior to the main researches, in the following Chapter 2, previous works on the development of artificial photosynthetic systems are introduced. The trends in the respective area are organized along with the important issues in the aspect of material science and energy conversions. Then three main topics are presented: Light harvesting (Chapter 3), Z-scheme electron transfer (Chapter 4) and CO_2 conversion (Chapter 5). Chapter 3 and 4 are on the basis of light dependent reaction and Chapter 5 is on the basis of dark reaction. Each part describes the important lessons adopted from the natural photosynthesis. Moreover, novel strategies in designing systems are developed using organic/inorganic hybrid materials which could overcome critical challenges of previous systems.

Reference

1. Ciais, P. et al. in Climate Change 2013: The Physical Science Basis. Contribution of Working Group I to the Fifth Assessment Report of the Intergovernmental Panel on Climate Change 465-570 (Cambridge University Press, 2014).
2. Agency, I.E. CO2 Emissions from Fuel Combustion 2017. (2017).
3. Allen, J.P. & Williams, J.C. in Photosynthetic Protein Complexes 275-293 (Wiley-VCH Verlag GmbH & Co. KGaA, 2008).
4. Hall, D.O., Rao, K. & Biology, I.o. Photosynthesis. (Cambridge University Press, 1999).
5. Croce, R. & van Amerongen, H. Natural strategies for photosynthetic light harvesting. *Nat Chem Biol* **10**, 492-501 (2014).
6. Engel, G.S. et al. Evidence for wavelike energy transfer through quantum coherence in photosynthetic systems. *Nature* **446**, 782-786 (2007).
7. Hildner, R., Brinks, D., Nieder, J.B., Cogdell, R.J. & van Hulst, N.F. Quantum Coherent Energy Transfer over Varying Pathways in Single Light-Harvesting Complexes. *Science* **340**, 1448-1451 (2013).
8. Amunts, A., Drory, O. & Nelson, N. The structure of a plant photosystem I supercomplex at 3.4 angstrom resolution. *Nature* **447**, 58-63 (2007).
9. Wientjes, E., Roest, G. & Croce, R. From red to blue to far-red in Lhca4: How does the protein modulate the spectral properties of the pigments? *Bba-Bioenergetics* **1817**, 711-717 (2012).
10. Blankenship, R. Origin and early evolution of photosynthesis.

Photosynthesis Research **33**, 91-111 (1992).

11. Zouni, A. et al. Crystal structure of photosystem II from Synechococcus elongatus at 3.8 angstrom resolution. *Nature* **409**, 739-743 (2001).
12. Biesiadka, J., Loll, B., Kern, J., Irrgang, K.D. & Zouni, A. Crystal structure of cyanobacterial photosystem II at 3.2 angstrom resolution: a closer look at the Mn-cluster. *Phys Chem Chem Phys* **6**, 4733-4736 (2004).
13. Elston, T., Wang, H. & Oster, G. Energy transduction in ATP synthase. *Nature* **391**, 510-513 (1998).
14. Bowes, G. Growth at elevated CO_2: photosynthetic responses mediated through Rubisco. *Plant, Cell & Environment* **14**, 795-806 (1991).
15. Gutteridge, S. & Pierce, J. A unified theory for the basis of the limitations of the primary reaction of photosynthetic CO_2 fixation: Was Dr. Pangloss right? *P Natl Acad Sci USA* **103**, 7203-7204 (2006).
16. Spreitzer, R.J. & Salvucci, M.E. Rubisco: structure, regulatory interactions, and possibilities for a better enzyme. *Annual review of plant biology* **53**, 449-475 (2002).
17. O'Regan, B. & Grätzel, M. A low-cost, high-efficiency solar cell based on dye-sensitized colloidal TiO_2 films. *Nature* **353**, 737 (1991).
18. Zhou, P., Yu, J. & Jaroniec, M. All-Solid-State Z-Scheme Photocatalytic Systems. *Adv Mater* **26**, 4920-4935 (2014).

Chapter 2. Artificial photosynthesis mimetic system

2.1 Introduction

Natural photosynthesis have recently received attention as a model system for solar energy absorption and conversion systems. Many pioneering works have been intensively making progress in mimicking or reengineering natural photosynthesis and designing artificial systems for a sustainable energy supply. Each sequential energy conversion process from light to biomass inspired new energy collection, transport and conversion system. Notwithstanding the numerous lessons of nature that provide inspiration for new developments, the features of natural photosynthesis need to be reengineered to meet man's demands.

Photosynthesis consists of various reaction stages carried over through several energetic and electronic interactions. Thus, each system that handles a specific reaction should be designed to collaborate inside the network. The photosystem is surrounded by a light harvesting complex in the thylakoid membrane to effectively accept absorbed light. Moreover, its electron-emitting direction is directed toward the stromal side to facilitate the direct use of the chemical product in the dark reaction in the stroma. Nature has also evolved to optimize its system to operate the reactions in the given condition. Photosynthesis is sensitively regulated by various conditions on earth, and the structure of the system is continually reconstructed. In this way, nature acquires a sophisticated design skill using the tools of biomaterials, mostly photosynthetic proteins, and provides significant lessons for various energy systems.

Various approaches to mimic or modify natural photosynthesis have been developed. Protein is a desirable functional material as a catalyst or electron/energy carrier but requires particular handling. In photosynthesis mimetic research, developing a practical biomaterial based on a protein or peptide has been attempted.[1] Furthermore, the materials should be integrated into an artificial system that is mostly constructed in the hybrid form of organic/inorganics.[2, 3] The key lessons from photosynthesis are classified into three energy conversion steps: (1) light harvesting, (2) electron transfer, and (3) carbon fixation. In this chapter, novel strategies to realize a photosynthesis-inspired energy system are presented together with an introduction to recently demonstrated examples.

2.2 Artificial antenna for light harvesting

Inspired by the photosynthetic antenna system, an artificial light harvesting system has been developed using various approaches. Among the interesting features discovered in nature, two strategies developed through evolution have incentivized the design of novel light harvesting systems: (1) tuning the optical properties of the antenna by organizing the chromophore molecules in a particular arrangement and (2) engineering the structure of the light harvesting complex to enable effective energy transfer toward the reaction center. The following are some previous works applying lessons from the natural antenna.

2.2.1 Chromophore assembly

In the design of the light harvesting complex, selecting a proper chromophore or combination of chromophores primarily determines the light absorption property. Porphyrin dye is the typical chromophore used in engineered light harvesting complexes in which chlorophyll is also included. It has a pyrrole subunit connected to a heterocyclic structure, usually with a metal ion inserted at the center of the ring. In addition to porphyrin, various chromophores are utilized according to the given situation, as the natural antenna uses some carotenoids to fill the green gap of chlorophylls. Then, to fabricate the net assembly as a light harvesting complex, an alternative to substitute for the protein support in nature is required. First, introducing a manufactured organic and/or inorganic template is a promising strategy to tighten the chromophores into the desired structure. The self-assembly of chromophores can also be induced by providing particular conditions

without needing to actively introduce the molecule into the scaffold. The two methods can be synergized by appropriate simultaneous utilization.

A metal template can be a stable framework for the chromophores in artificial light harvesting systems. Furumaki et al. reported the formation of bacteriochlorophyll aggregates on gold nanorods in 2014.[4] The bacterial chromophores could be finely aggregated by forming hydrogen bonds to the hydroxylated gold surface. The observed spectroscopic properties were similar to those of the natural bacterial light harvesting complex, despite the difference in the mesoscopic structure. In another approach, Grill et al. utilized a gold surface as an activation template throughout the chromophore assembly process.[5] Herein, porphyrin formed a covalently bound molecular nanostructure on the gold surface that provides an essential support for the porphyrins to be connected.

An organic template including peptides, organic molecules, and polymers can also efficiently stabilize chromophores. In the artificial antenna, covalent bonding on the organic scaffold can be used to fix the chromophores in the desired arrangement, whereas the natural chromophores interact with protein residues mainly by dipole interactions or hydrogen bonds. In 2013, Kang et al. introduced a helical peptoid for the fine regulation of the porphyrin arrangement.[6] On a peptoid scaffold, several porphyrins can be conjugated in a specific arrangement during the peptoid synthesis step. The intermolecular distance, orientation and number of porphyrins were easily controlled by arranging the desired sequence. This approach presents a practical method to regulate an elaborate structure on the molecular scale.

A metal-organic framework (MOF) is an organic/inorganic hybrid

platform that enables the organization of chromophores into a desired arrangement.[7] Chromophores can be hierarchically integrated into a crystalline MOF scaffold, thereby facilitating the study of both short- and long-range energy interactions through crystallographic analysis. Recent works on MOF-based light harvesting structures have demonstrated their feasibility for energy transfer studies.[8] Hupp and coworkers developed porphyrin-based MOF layers that show significant energy transfer.[9, 10] In a 2013 report, a MOF constructed from zinc-metalated porphyrins showed long-range and anisotropic energy migration (**Figure 2.1** (a)). The authors attributed the remarkable energy transfer to enhanced pi conjugation in the MOF. Particularly, assigning directionality to the energy transfer is a significant issue in both natural and artificial light harvesting to effectively concentrate the photo-energy in the reaction center.

Inducing a self-assembled complex without the aid of a template has also been used in manufacturing an artificial chromophore assembly. In the case of metal-inserted chromophore molecules, the metal-ligand interaction can form highly stabilized supramolecules with structural integrity. A construction strategy using coordination chemistry for multi-chromophore supramolecular assemblies has been developed as a convenient method to control the intermolecular arrangement.[11]

Self-assembly has also received attention in the structural design of an entire antenna complex with a larger scope. For instance, a cyclic architecture of a chromophore assembly can be manufactured. In an approach using self-assembly, several reports have shown that porphyrins can be automatically organized into cyclic architectures of controllable size.[12] Because the cyclic structure of the light

harvesting antenna complex has been considered a key for efficient energy transfer in purple bacteria, the effective energy transfer mechanism on highly symmetric cyclic structures has been studied in several examples. One unique structure of a self-assembled supramolecule is the nanorod-shaped antenna of metal chlorides, first reported by Wurthner and coworkers in 2005.[13] Recently, Shoji et al. reported nanotube-structured supramolecules of metal chlorophyll derivatives.[14] In this work, magnesium, zinc, and cadmium chlorophyll derivatives synthesized from natural chlorophyll a were self-assembled from a hydrophobic solution into nanotubes 5 nm in diameter (**Figure 2.1** (b)).

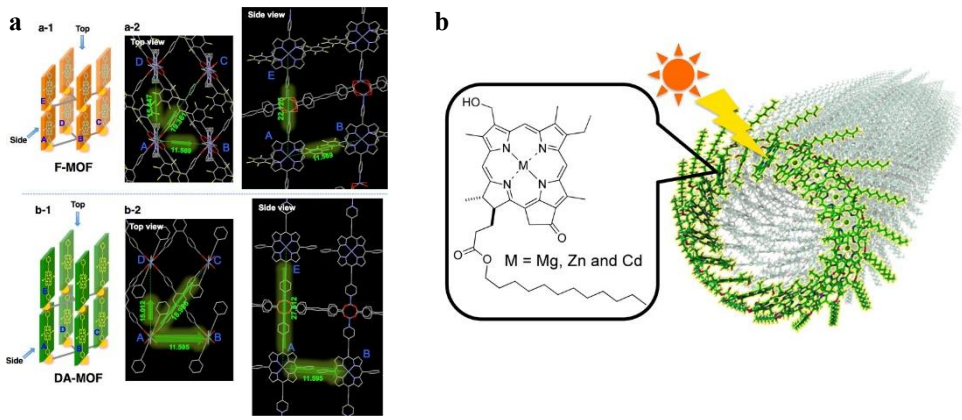

Figure 2.1. Schematic representation for artificial antenna. (a) Porphyrin based MOFs. (b) Nanotube constructed by synthetic metal chlorophyll derivatives.

2.2.2 Antenna-reaction center hybridized light harvesting complex

The absorbed photon energy from the antenna should be collected at the reaction center for the following electrochemical energy conversion. Thus, the net light harvesting system is constructed as an integrated hybrid form of an antenna and a reaction center to facilitate cooperative interaction. The configuration of the energy donor and acceptor is the essential factor to drive excitons in the preferred direction. The design of light harvesting complex can be engineered by using various scaffolds and bridging methods to integrate the energy donor and acceptor.

At the molecular scale, linking molecules covalently stretched from the primary donor to the final acceptor can form an energy bridge. The size and shape of the antenna-reaction center supramolecule can vary from a dyad of a chromophore and an acceptor molecule to a hierarchical dendrimer-shaped complex. Recent examples of light harvesting systems for excitation energy transfer and conversion are organized in several reviews.[15-17]

In more advanced light harvesting systems analogous to massive photosynthetic proteins, copious chromophores are integrated peripherally oriented to the reaction center. In 2016, Ning et al. reported a porphyrin-based nanohybrid light harvesting complex using a gold-porphyrin core-shell hybrid aligned on carbon nanotubes.[18] The entire structural design was inspired from the antenna-reaction center cooperated complex embedded within the thylakoid membrane (**Figure 2.2** (a)). Woller et al., moreover, inserted the accepter into a lipid bilayer and attached donor dyes embedded in a DNA scaffold.[19] In the hybrid system, the DNA-donor complex and acceptor porphyrin play the roles of the antenna and

reaction center, respectively, conceptually inspired from the natural light harvesting system (**Figure 2.2** (b)). Likewise, massive light harvesting complexes have been developed by introducing diverse hybrid materials from biomaterials to inorganics.

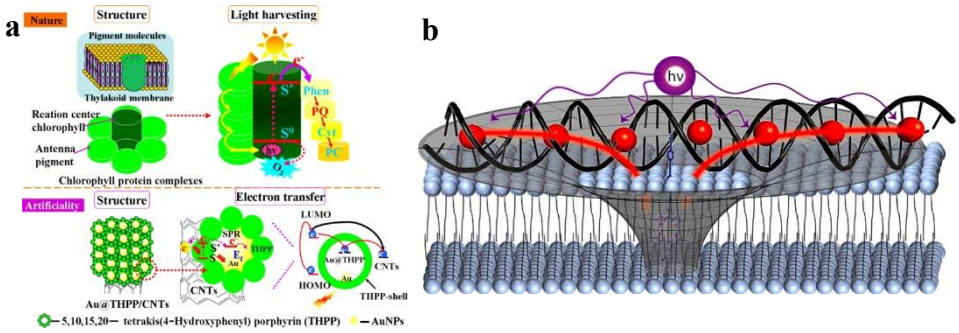

Figure 2.2. Schematic representation for artificial light harvesting complex. (a) Porphyrin-based nanohybrid light harvesting complex. (b) DNA-porphyrin assembly for light harvesting.

2.3 Artificial electron transfer system for energy conversion

The ultimate function of the light reaction of photosynthesis is to convert light energy into chemical energy that can be used in the metabolism of the organism. Following the photo-induced charge separation in the reaction center of the photosystems, the excited electrons move through the photosystem and generate a chemical reductant. The electron-to-chemical energy conversion model has inspired the development of various electrochemical energy devices adapted to man's demand.

2.3.1 Utilization of photosynthetic protein in hybrid system

Photosynthetic proteins have recently received attention as biomaterials for solar energy absorption and conversion systems. In photosystems, the step of charge separation induced from absorbed photon exhibits ~100%. Such a high efficiency results from the collaborative reaction of light harvesting and light-induced charge separation in these protein. To construct the protein, light-absorbing pigments and cofactors are three-dimensionally aligned in a favorable orientation and distance for electron transfer.

Many pioneering works have been intensively making progress in hybridizing photosynthetic proteins with synthetic materials to utilize the protein in photoelectric system. The synergistic combination of proteins and synthetic materials can provide new opportunities in the development of new hybrid materials. Especially, semiconductor/photosynthetic protein hybrid systems have

been recently developed. In the semiconductor/photosynthetic protein hybrid system, the tunable energy level of the semiconductor and flexible band bending at the interface with the protein allow for switchable and controllable electron and/or energy flow. Compared with metal, semiconductors have the advantage of tunability of their band structures, the ability to absorb light and the wide availability of the conjugation method. Thus, a biomolecular/semiconductor composite can nurture the strength over traditional semiconductor materials.

In this hybrid system, the interaction occurs through two different communicating methods: (1) the electron transfer between semiconductor electrodes and photosynthetic protein and (2) the energy transfer between semiconductor quantum dots and photosynthetic protein. Here, the main issues in designing the system are the hybrid methods of proteins to inorganic surfaces at the nanoscale and relative energy band position of materials, which deeply affect the total efficiency of system and the direction of electron and/or energy flow. The simplified linking methods between the proteins and synthetic substrates are depicted in **Figure 2.3**. Through the electron/energy transfer at the interface of a semiconductor /photosynthetic protein hybrid complex, we envision potential applications such as photoelectrochemical cells, optical biosensors and nanostructured photoelectronic devices (**Figure 2.4**).

The main challenge in operating the constructed hybrid system is determining how to maintain the long-term stability of the protein. Remarkable advances in the performance of photosynthetic protein hybrid systems have been reported but are limited to demonstrating transient efficiencies of less than a few minutes. Long-term stability tests have yet to be addressed and require in-depth

understanding of the optimal conditions of the protein, including the surfactant or lipid membrane surrounding the protein, the hydrophobic interaction between materials, and the aligned orientation and density of the protein assembly. One excellent approach to address the challenging requirements of stabilization is to mimic the natural membrane system. . Possible concrete future progress being made towards the design of the optimized condition for proteins involves developing an artificial lipid membrane, encapsulating the bio-hybrid system into a gel and inducing self-assembly of proteins. Another challenge for practical application is to translate laboratory-scale studies into industrial applicable research. Thus, techniques in mass production and simplicity in fabrication should also be addressed in addition to stable and high performance.

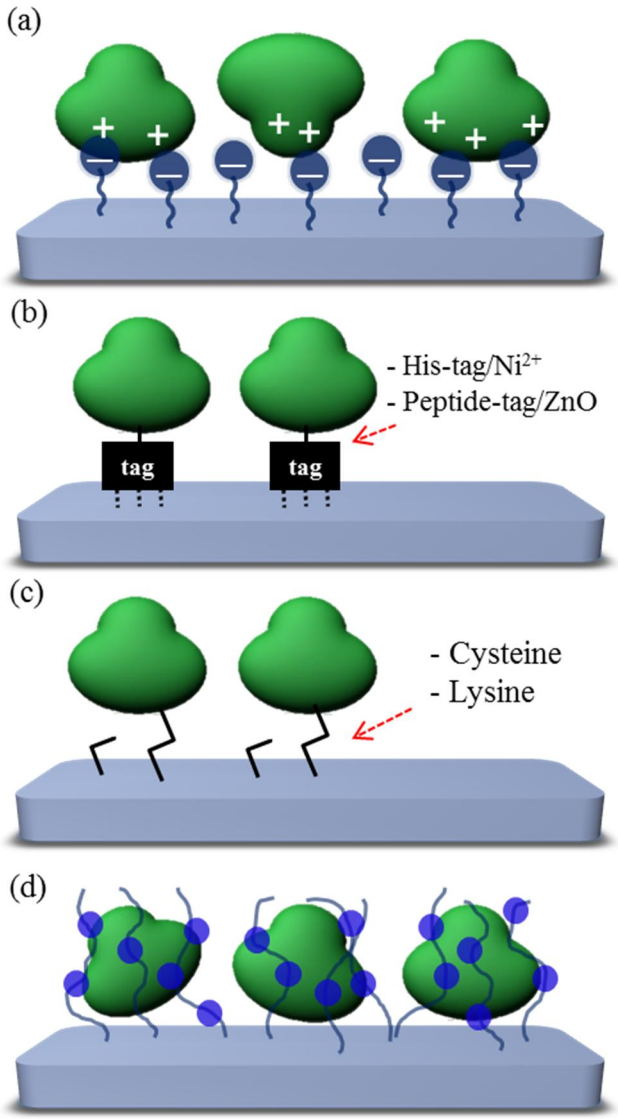

Figure 2.3. The linking methods between proteins and synthetic substrates. (a) electrostatic adsorption, (b) affinity tag binding, (c) covalent binding and (d) plugging.

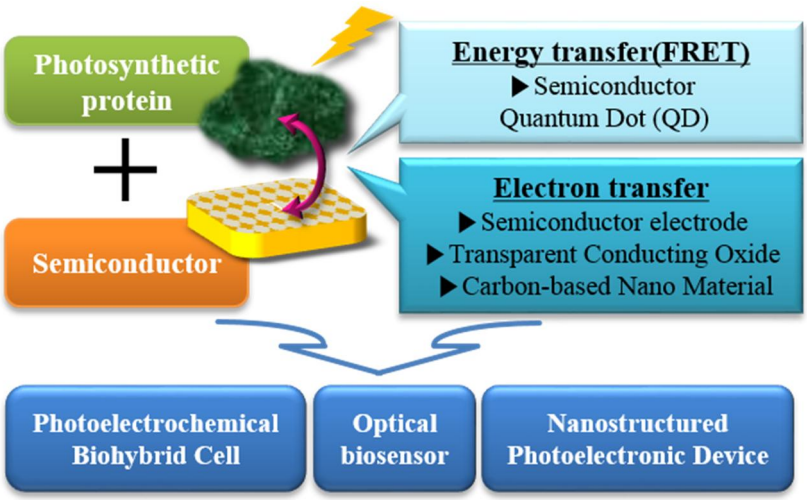

Figure 2.4. Scheme of photosynthetic protein/semiconductor hybrid system.

2.3.2 Photo-electrode for electrochemical reaction

Inspired by the electrochemical energy conversion in the photosystem, an artificial photo-electrode for the redox chemical reaction has been developed. In the artificial inorganic electrode, a semiconductor typically excites electrons up to its band gap in analogy to the photo-excitation of the photosystem. The semiconductor itself, or with the aid of cocatalysts, sequentially catalyzes the desired redox reaction, as the excited electron reduces $NADP^+$ at the end of the photosystem. The typical semiconductor photo-electrode utilized in the artificial electrochemical cell includes silicon, hematite, and titanium dioxide. According to their specific energy band positions and catalytic properties, electrodes can be applied for water splitting,[20-22] carbon dioxide reduction,[23] and other chemical reactions.

As a very direct approach to adapt photosynthetic electrochemical energy conversion, the photosystem protein itself can be used as an electrode material. The photosystem's modified photo-electrode is promising due to its higher energy conversion efficiency (the charge separation efficiency of PSI is ~100% [24]) and lower recombination rate compared to that of a semiconductor. However, challenges remain, such as the instability of the photosystems on the electrode and the inefficient transport of photo-electrons from the photosystem to the electrode. Many efforts have been focused on the development of a proper platform to trap the photosystem and transfer charges, and a conducting polymer is often proposed as an electrode material that can fulfill these requirements. Nafion, for example, has been reported for its ability to encapsulate a photosystem while permitting electron transfer.[25] Attributed to its unique selective conductivity for cations, photo-

excited electrons can be carried by positively charged electron transfer mediators, such as methyl viologen. On the other hand, a polyaniline-based photo-electrode has also been suggested.[26] Polyaniline can be synthesized on the electrode surface in the form of a three-dimensional network, which can trap photosystems and directly transfer excited electrons through a chain-hopping mechanism.

Inspired by the directional electron transfer of the photosystem owing to its anisotropic nature, controlling the orientation of the photosystem has been of growing significance in enhancing the efficiency of the photo-electrode. While the electron-hole pair generation in semiconductors is isotropic, the photosystem possesses a precise site of electron emission. Thus, researchers have tried to utilize this feature by aligning photosystems to orient the excited electrons directly toward to the electrode. Kato et al. introduced carboxylic acid functionalized ITO as a supporting electrode for PSII to control the orientation of the protein alignment (**Figure 2.5**).[27] As the functional group was negatively charged, the positively charged stromal side of PSII was selectively bound to the electrode by electrostatic interaction. This led to direct electron transfer from the electron donor site on the stromal side to the ITO electrode. The linkage was further stabilized by amide bond formation via EDC coupling, which resulted in a greatly enhanced photocurrent and stability of the electrode.

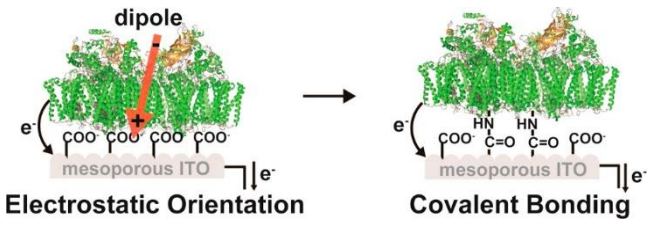

Figure 2.5. Immobilization of PSII on carboxylated ITO electrode via electrostatic immobilization (left) and covalent immobilization (right).

2.3.3 Z-schematic fuel production system

Along with the development of artificial photoelectrodes inspired by photosystems, mimics of the full Z-scheme have also been demonstrated. In the artificial Z-scheme, semiconducting materials can replace two photosystems, or photosynthetic proteins can be directly utilized like in the case of photoelectrodes. The photoactive materials are selected based on the proper energy level for the desired redox reactions and integrated into one system that can facilitate the electron transfer between the reaction centers. For the stable connection of materials and smooth transfer of electrons, proper electron mediators between the two reaction centers are introduced in the most of cases. By developing step-wise excitation in Z-scheme, the required light energy can be reduced compared to the single excitation system. Thus, in case of water splitting, the wavelength of light can be shifted from UV to visible region when the photocatalytic system is designed in Z-scheme. The final design of the Z-scheme is typically classified into one of two types depending on the electron mediator materials: redox ion pairs and electron-conducting metals.

When redox ion pairs are applied as electron mediators in the artificial Z-scheme, the two reaction centers are physically divided and interact via the redox reaction of the ions. Electron loss resulting from the unintended reverse reaction and the narrow pH window are typical drawbacks of the system that limit the electron transfer efficiency.[28] The Rogner group selected an Os-based redox hydrogel as an electron mediator and designed a serially connected bio-photovoltaic cell by using PSI and PSII as photoelectrodes (**Figure 2.6**).[29] The system also mimicked the ATP synthesis process of the Z-scheme along with

electron transfer, generating light to electrical energy conversion driven by the potential difference in the Z-schematic electron flow. Furthermore, the photovoltaic properties, such as power output and energy conversion efficiency, can also be enhanced by tuning the redox potential of each electron mediator for the two photoelectrodes.[30]

Electron-conducting metals are also utilized as electron mediators, providing a direct electron pathway between the two reaction centers. In contrast to redox ion pairs, two reaction centers can be physically combined by ohmic contact to form an all-solid-state system with low contact resistance. Thus, the distance of electron transfer can be reduced compared to the non-contacting systems. Moreover, the electron loss from the reverse reaction can be hampered, and a wide pH window can be achieved.[28] All-solid-state has been typically applied in designing the Z-scheme of two semiconductors. The first example of all-solid-state Z-scheme was TiO_2-Au-CdS system which was reported in 2006.[31] The photocatalytic activity was enhanced than two-component systems because the Au mediator promoted the separation of generated charge carriers from two semiconductors. Ag nanoparticles are also used as efficient mediator due to its surface plasmon resonance (SPR) effect.[32, 33] This enabled to utilize visible light effectively in Z-scheme systems.

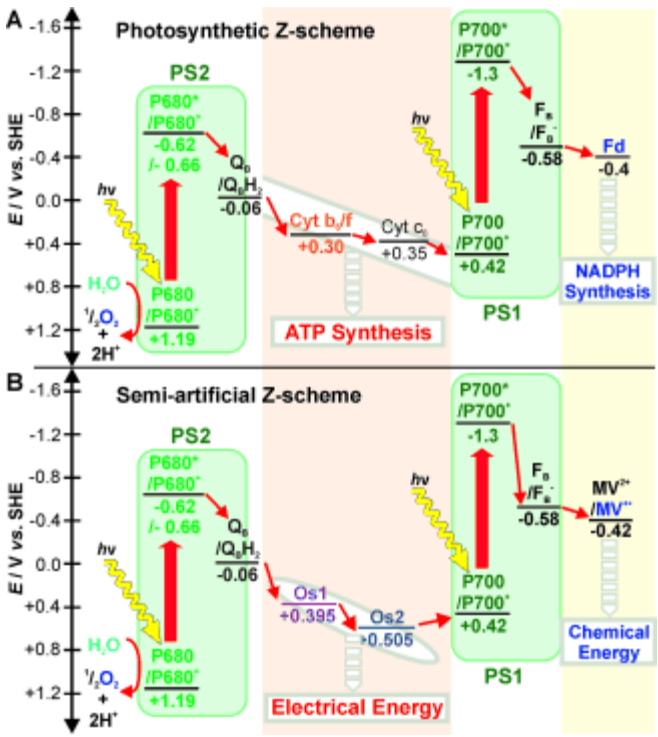

Figure 2.6. Electron transfer pathway of artificial Z-schematic system using redox ion pairs as a mediator.

2.4 Electrochemical carbon dioxide fixation

Carbon fuel is the ultimate practical energy source for both living organisms and machine engines. Nature utilizes CO_2 from the atmosphere as an infinite carbon source and produces sugar such as glucose and sucrose via the photosynthetic dark reaction. The products from photosynthesis become the foundation of the hydrocarbon source on the ground which is essential building block for organisms. Furthermore, after sedimentation underneath the ground, the hydrocarbons are converted into valuable coal. On the other hand, the amount of the coal has been rapidly depleted after industrialization and is expected to lead to a drastic carbon energy deficiency soon. At this stage, a novel carbon storage pathway inspired by carbon fixation in photosynthesis can be a smart solution to secure a stable route for energy production.

Inspired by natural photosynthesis, many studies have been conducted on utilizing carbon dioxide in fuels.[34-36] One of the main approaches is to replace rubisco with other efficient catalysts. By substituting the enzyme with artificially designed catalysts, the overall efficiency of the carbon fixation can be largely improved.

2.4.1 Direct electrochemical reduction reaction of carbon dioxide

Recently, the electrochemical conversion of carbon dioxide has gained much attention as an artificially developed carbon fixation system.[35, 37, 38] This is because it can be operated by renewable energy in moderate conditions such as at

room temperature and easily manipulated for scale-up in industry. In the electrochemical reduction of carbon dioxide, the gas dissolved in the electrolyte reacts with protons and electrons under an electrical potential and is converted into products such as carbon monoxide, formate, and methanol. This method operates in a similar manner to photosynthesis, as both of them require applied energy, protons and catalysts in moderate conditions. Therefore, this section will focus mainly on the electrochemical conversion of carbon dioxide into other carbon fuels.

One approach is to electrochemically reduce carbon dioxide using a homogeneous catalyst. Homogeneous catalysts refer to catalytically active molecules homogeneously dissolved in an electrolyte. A great deal of molecules have been explored as electrocatalysts for carbon fixation.[39-44] Most of them involve transition metals such as Pd,[40, 41] Ru[42] and Re[39, 43, 44] which are too expensive to be used frequently. Additionally, these systems exhibit low reactivity and a short lifetime due to their chemically unstable nature.

There have been a number of studies performed to overcome these disadvantages of homogeneous catalysts. The Kubiak group studied the homogeneous catalysis of carbon dioxide using bipyridine carbonyl catalysts with metal ions.[43, 45, 46] When they substituted for the rhenium in a Re(bpy-R)$(CO)_3$X scaffold with manganese (**Figure 2.7** (a)), which is more abundant, their new catalysts exhibited activity toward carbon dioxide reduction with the addition of Brönsted acids.[46] Mn(bpy-*t*Bu)$(CO)_3$Br operated at a lower overpotential compared to Re catalysts with great Faradaic efficiency to produce carbon monoxide. The Mn catalysts did not show catalytic activity without weak Brönsted acids, which may be attributed to the protonation of a M-CO_2 adduct and the eventual activation of

the reduction process.

Savéant and co-workers investigated catalysts based on metalloporphyrins.[37, 47] They focused on iron(0) tetraphenylporphyrins with various functional groups as shown in Fig. 6a. Similar to the above-mentioned observation by the Kubiak group, the Savéant group also revealed that a local proton source enhances the catalytic activity of iron(0) porphyrins.[47] Additionally, they discovered that the presence of phenolic OH groups accelerates the catalytic reaction because of the resulting high local concentration of protons.

Another approach is to design heterogeneous catalysts that are active for the reduction of carbon dioxide. Heterogeneous catalysts include not only electrodes with catalytic molecules deposited on them but also electrodes themselves. Generally, transition metals that are known to reduce carbon dioxide, such as Au,[48, 49] Ag [50, 51] or Cu,[52-54] have been used as electrodes. Despite their natural ability to catalyze the carbon dioxide reduction, a large number of studies have been devoted to improving their reactivity.

Recently, Nam and co-workers demonstrated that Au nanoparticles with a concave rhombic dodecahedral (concave RD) shape can show superior electrocatalytic activity for the conversion of carbon dioxide to carbon monoxide (**Figure 2.7** (b)).[55] Nanoparticles were synthesized by using 4-aminothiophenol as a shape modifier and were drop-casted on carbon paper for the evaluation of their electrochemical performance. HRTEM images showed that the Au nanoparticles contained various high-index facets such as (331), (221), and (553). The prepared electrode exhibited improved reactivity and selectivity toward the electroreduction

of carbon dioxide compared to typical polycrystalline Au electrodes, a known catalyst for the production of carbon monoxide from carbon dioxide. Thus, it has been proposed that the high activity of the concave RD was achieved by the higher-index facets on its surface.

The Kanan group introduced oxide-derived metal electrodes, which have a high catalytic ability for the reduction of carbon dioxide.[56, 57] In 2012, they first reported an oxide-derived Au electrode that was fabricated by electrochemically reducing a previously oxidized Au electrode.[57] The resulting electrode showed the formation of Au nanoparticles and a highly selective activity to reduce carbon dioxide into carbon monoxide with a very low overpotential. Although the group proposed that the oxide-derived Au electrode stabilizes $CO_2^{\cdot-}$ better than polycrystalline Au, a clear mechanistic understanding is still not available (**Figure 2.7** (c)).

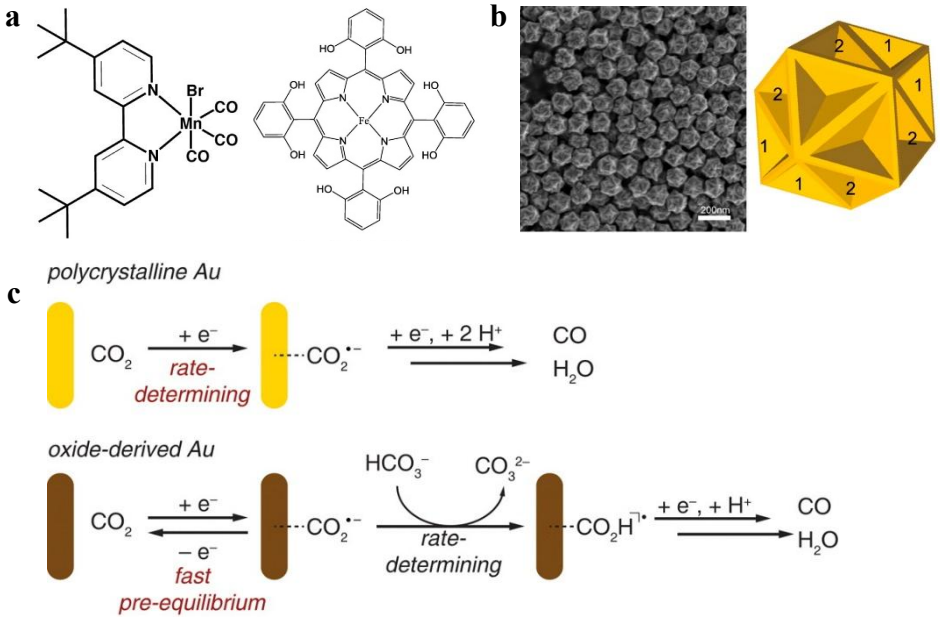

Figure 2.7. (a) Homogeneous catalysts for the reduction of carbon dioxide. (left) Mn(bpy-tBu)$(CO)_3$Br and (right) Iron 5,10,15,20-tetrakis(2',6'-dihydroxylphenyl)-porphyrin. (b) Morphology of concave RD nanoparticles. SEM image (left) and the corresponding model (right). (c) Mechanistic model for the reduction of carbon dioxide to carbon monoxide on polycrystalline Au and oxide-derived Au.

2.4.2 Carboxylation reaction using carbon dioxide

Despite the recent development of various catalysts, the current technologies of the carbon dioxide electrochemical reduction have unresolved challenges. Among them, one of the most difference compared to the carbon fixation in Calvin cycle of photosynthesis is that the final product is limited to low-carbon fuels as C_1 and C_2. In natural photosynthesis, carboxylation on C_5 substrate forms C_6 products. However, most of the artificial electrocatalysts for carbon dioxide conversion are not suitable for C-C coupling between C_1 products. Therefore, carboxylation reaction of hydrocarbon feedstocks using carbon dioxide as a one-carbon building block is an attractive route for the synthesis of high-carbon fuels.

In natural carbon cycle, CO_2 fixation occurs by carboxylation of hydrocarbon substrate catalyzed by Rubisco.[58, 59] Recently, the strategy of CO_2 insertion to the hydrocarbon feedstocks has been adopted in the organic synthesis such as production of carboxylic acids,[60-68] (poly)carbonates[69-78] and alcohols. In **Figure 2.8**, representative examples of artificial CO_2 insertion reactions for organic synthesis are shown.[79] Some of these protocols have been industrialized for the practical applications.

However, the utilization of CO_2 is still challenging and the reactions are limited to only few examples because the gas is thermodynamically and kinetically inert.[79] Consequently, most of studies on CO_2 insertion rely on the chemical carboxylation using highly reactive organometallic nucleophiles in severe condition which includes high temperature, high pressure and strong reductants.

Electrochemical approaches have also reported which can avoid the use of chemical reductants. These method can be considered as practical strategy due to its fast and massive scale reaction compared to the chemical reactions. However, it has been received less attention yet because the process has lack of site-selectivity controllability of the products.

Despite the challenging steps for CO_2 activations, using CO_2 as a one-carbon building block for the synthesis of hydrocarbon fuel is very attractive strategy in the aspect of both sustainable energy cycle and practical chemical industry. Researchers envision that the virtual artificial photosynthesis can be achieved as shown in **Figure 2.9**.

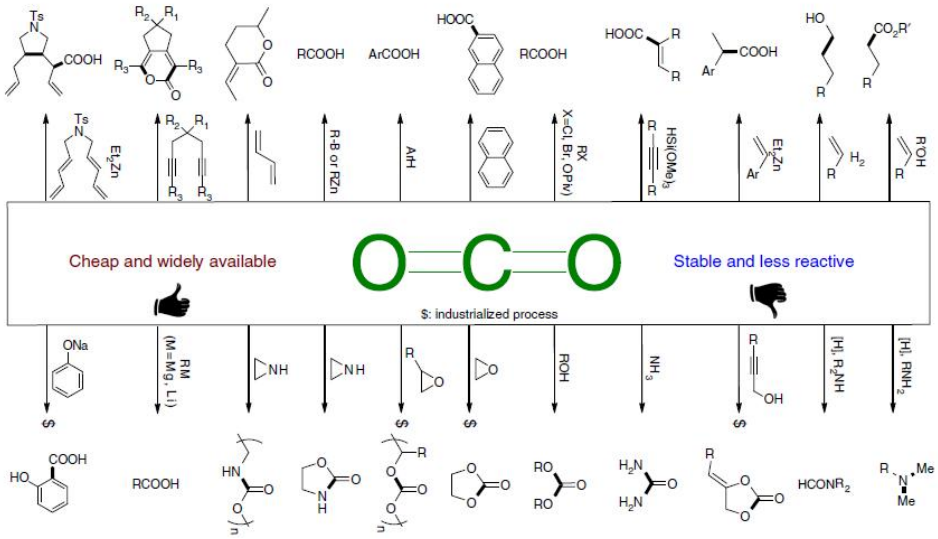

Figure 2.8. Artificial CO_2 insertion reactions for organic synthesis.

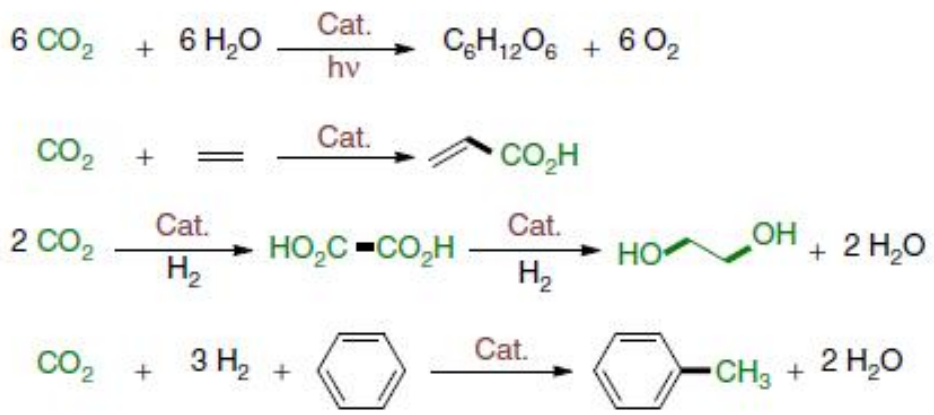

Figure 2.9. Possible CO_2 insertion reactions.

Reference

1. Lee, J.-H., Lee, J.H., Lee, Y.J. & Nam, K.T. Protein/peptide based nanomaterials for energy application. *Current Opinion in Biotechnology* **24**, 599-605 (2013).
2. Kim, J.H., Nam, D.H. & Park, C.B. Nanobiocatalytic assemblies for artificial photosynthesis. *Current Opinion in Biotechnology* **28**, 1-9 (2014).
3. Kim, Y., Shin, S.A., Lee, J., Yang, K.D. & Nam, K.T. Hybrid system of semiconductor and photosynthetic protein. *Nanotechnology* **25** (2014).
4. Furumaki, S., Vacha, F., Hirata, S. & Vacha, M. Bacteriochlorophyll Aggregates Self-Assembled on Functionalized Gold Nanorod Cores as Mimics of Photosynthetic Chlorosomal Antennae: A Single Molecule Study. *ACS Nano* **8**, 2176-2182 (2014).
5. Grill, L. et al. Nano-architectures by covalent assembly of molecular building blocks. *Nat. Nanotechnol.* **2**, 687-691 (2007).
6. Kang, B., Chung, S., Ahn, Y.D., Lee, J. & Seo, J. Porphyrin-Peptoid Conjugates: Face-to-Face Display of Porphyrins on Peptoid Helices. *Org. Lett.* **15**, 1670-1673 (2013).
7. Zhang, T. & Lin, W.B. Metal-organic frameworks for artificial photosynthesis and photocatalysis. *Chem. Soc. Rev.* **43**, 5982-5993 (2014).
8. So, M.C., Wiederrecht, G.P., Mondloch, J.E., Hupp, J.T. & Farha, O.K. Metal-organic framework materials for light-harvesting and energy transfer. *Chem. Commun.* **51**, 3501-3510 (2015).
9. Son, H.J. et al. Light-Harvesting and Ultrafast Energy Migration in

Porphyrin-Based Metal-Organic Frameworks. *Journal of the American Chemical Society* **135**, 862-869 (2013).

10. Lee, C.Y. et al. Light-Harvesting Metal-Organic Frameworks (MOFs): Efficient Strut-to-Strut Energy Transfer in Bodipy and Porphyrin-Based MOFs. *Journal of the American Chemical Society* **133**, 15858-15861 (2011).
11. Frischmann, P.D., Mahata, K. & Wurthner, F. Powering the future of molecular artificial photosynthesis with light-harvesting metallosupramolecular dye assemblies. *Chemical Society reviews* **42**, 1847-1870 (2013).
12. Yang, J., Yoon, M.C., Yoo, H., Kim, P. & Kim, D. Excitation energy transfer in multiporphyrin arrays with cyclic architectures: towards artificial light-harvesting antenna complexes. *Chem. Soc. Rev.* **41**, 4808-4826 (2012).
13. Huber, V., Katterle, M., Lysetska, M. & Wurthner, F. Reversible self-organization of semisynthetic zinc chlorins into well-defined rod antennae. *Angew. Chem. Int. Edit.* **44**, 3147-3151 (2005).
14. Shoji, S. et al. Nanotubes of Biomimetic Supramolecules Constructed by Synthetic Metal Chlorophyll Derivatives. *Nano Lett*. (2016).
15. Liu, J.Y., El-Khouly, M.E., Fukuzumi, S. & Ng, D.K.P. Mimicking Photosynthetic Antenna-Reaction-Center Complexes with a (Boron Dipyrromethene)(3)-Porphyrin-C-60 Pentad. *Chem-Eur. J.* **17**, 1605-1613 (2011).
16. El-Khouly, M.E., Fukuzumi, S. & D'Souza, F. Photosynthetic Antenna–

Reaction Center Mimicry by Using Boron Dipyrromethene Sensitizers. *ChemPhysChem* **15**, 30-47 (2014).

17. Harriman, A. Artificial light-harvesting arrays for solar energy conversion. *Chemical communications* **51**, 11745-11756 (2015).
18. Ning, X. et al. Construction of a Porphyrin-Based Nanohybrid as an Analogue of Chlorophyll Protein Complexes and Its Light-Harvesting Behavior Research. *The Journal of Physical Chemistry C* **120**, 919-926 (2016).
19. Woller, J.G., Hannestad, J.K. & Albinsson, B. Self-assembled nanoscale DNA–porphyrin complex for artificial light harvesting. *Journal of the American Chemical Society* **135**, 2759-2768 (2013).
20. Sim, U. et al. N-doped monolayer graphene catalyst on silicon photocathode for hydrogen production. *Energ. Environ. Sci.* **6**, 3658-3664 (2013).
21. Sim, U. et al. N-doped graphene quantum sheets on silicon nanowire photocathodes for hydrogen production. *Energ. Environ. Sci.* **8**, 1329-1338 (2015).
22. Yang, T.-Y. et al. An iron oxide photoanode with hierarchical nanostructure for efficient water oxidation. *Journal of Materials Chemistry A* **2**, 2297-2305 (2014).
23. Yang, K.D. et al. Graphene Quantum Sheet Catalyzed Silicon Photocathode for Selective CO_2 Conversion to CO. *Adv. Funct. Mater.* **26**, 233-242 (2016).
24. Vos, M.H. et al. Direct observation of vibrational coherence in bacterial

reaction centers using femtosecond absorption spectroscopy. *Proceedings of the National Academy of Sciences* **88**, 8885-8889 (1991).

25. Baker, D.R., Simmerman, R.F., Sumner, J.J., Bruce, B.D. & Lundgren, C.A. Photoelectrochemistry of photosystem I bound in nafion. *Langmuir* **30**, 13650-13655 (2014).

26. Gizzie, E.A. et al. Photosystem I-polyaniline/TiO_2 solid-state solar cells: simple devices for biohybrid solar energy conversion. *Energ. Environ. Sci.* **8**, 3572-3576 (2015).

27. Kato, M., Cardona, T., Rutherford, A.W. & Reisner, E. Covalent Immobilization of Oriented Photosystem II on a Nanostructured Electrode for Solar Water Oxidation. *Journal of the American Chemical Society* **135**, 10610-10613 (2013).

28. Zhou, P., Yu, J. & Jaroniec, M. All-Solid-State Z-Scheme Photocatalytic Systems. *Adv. Mater.* **26**, 4920-4935 (2014).

29. Kothe, T. et al. Combination of A Photosystem 1-Based Photocathode and a Photosystem 2-Based Photoanode to a Z-Scheme Mimic for Biophotovoltaic Applications. *Angewandte Chemie International Edition* **52**, 14233-14236 (2013).

30. Hartmann, V. et al. Redox hydrogels with adjusted redox potential for improved efficiency in Z-scheme inspired biophotovoltaic cells. *Phys. Chem. Chem. Phys.* **16**, 11936-11941 (2014).

31. Tada, H., Mitsui, T., Kiyonaga, T., Akita, T. & Tanaka, K. All-solid-state Z-scheme in CdS-Au-TiO_2 three-component nanojunction system. *Nat. Mater.* **5**, 782-786 (2006).

32. Hou, W. & Cronin, S.B. A Review of Surface Plasmon Resonance-Enhanced Photocatalysis. *Adv. Funct. Mater.* **23**, 1612-1619 (2013).

33. Jones, M.R., Osberg, K.D., Macfarlane, R.J., Langille, M.R. & Mirkin, C.A. Templated Techniques for the Synthesis and Assembly of Plasmonic Nanostructures. *Chem. Rev.* **111**, 3736-3827 (2011).

34. Aresta, M. & Dibenedetto, A. Utilisation of CO_2 as a chemical feedstock: opportunities and challenges. *Dalton Transactions*, 2975-2992 (2007).

35. Qiao, J., Liu, Y., Hong, F. & Zhang, J. A review of catalysts for the electroreduction of carbon dioxide to produce low-carbon fuels. *Chemical Society reviews* **43**, 631-675 (2014).

36. Concepcion, J.J., House, R.L., Papanikolas, J.M. & Meyer, T.J. Chemical approaches to artificial photosynthesis. *Proceedings of the National Academy of Sciences* **109**, 15560-15564 (2012).

37. Costentin, C., Robert, M. & Savéant, J.-M. Catalysis of the electrochemical reduction of carbon dioxide. *Chemical Society reviews* **42**, 2423-2436 (2013).

38. Benson, E.E., Kubiak, C.P., Sathrum, A.J. & Smieja, J.M. Electrocatalytic and homogeneous approaches to conversion of CO_2 to liquid fuels. *Chemical Society reviews* **38**, 89-99 (2009).

39. Hawecker, J., Lehn, J.M. & Ziessel, R. Electrocatalytic Reduction of Carbon-Dioxide Mediated by Re(Bipy)(Co)3cl(Bipy=2,2'-Bipyridine). *J Chem. Soc. Chem. Comm.*, 328-330 (1984).

40. Bernatis, P.R., Miedaner, A., Haltiwanger, R.C. & Dubois, D.L. Exclusion of 6-Coordinate Intermediates in the Electrochemical Reduction of CO_2

Catalyzed by [Pd(Triphosphine)(CH_3CN)](BF_4)(2) Complexes. *Organometallics* **13**, 4835-4843 (1994).

41. Raebiger, J.W. et al. Electrochemical reduction of CO_2 to CO catalyzed by a bimetallic palladium complex. *Organometallics* **25**, 3345-3351 (2006).

42. Tanaka, K. & Ooyama, D. Multi-electron reduction of CO_2 via Ru-CO_2, -C(O)OH, -CO, -CHO, and -CH_2OH species. *Coordin. Chem. Rev.* **226**, 211-218 (2002).

43. Kumar, B., Smieja, J.M. & Kubiak, C.P. Photoreduction of CO_2 on p-type Silicon Using Re(bipy-Bu ')(CO)(3)Cl: Photovoltages Exceeding 600 mV for the Selective Reduction of CO_2 to CO. *J. Phys. Chem. C* **114**, 14220-14223 (2010).

44. Sullivan, B.P., Bolinger, C.M., Conrad, D., Vining, W.J. & Meyer, T.J. One-Electron and 2-Electron Pathways in the Electrocatalytic Reduction of CO_2 by Fac-Re(2,2'-Bipyridine)($Co)_3$Cl. *J. Chem. Soc. Chem. Comm.*, 1414-1415 (1985).

45. Kumar, B., Smieja, J.M., Sasayama, A.F. & Kubiak, C.P. Tunable, light-assisted co-generation of CO and H_2 from CO_2 and H_2O by Re(bipy-tbu)($CO)_3$Cl and p-Si in non-aqueous medium. *Chemical communications* **48**, 272-274 (2012).

46. Smieja, J.M. et al. Manganese as a Substitute for Rhenium in CO_2 Reduction Catalysts: The Importance of Acids. *Inorganic Chemistry* **52**, 2484-2491 (2013).

47. Costentin, C., Drouet, S., Robert, M. & Saveant, J.M. A Local Proton Source Enhances CO_2 Electroreduction to CO by a Molecular Fe Catalyst.

Science **338**, 90-94 (2012).

48. Zhu, W.L. et al. Monodisperse Au Nanoparticles for Selective Electrocatalytic Reduction of CO_2 to CO. *Journal of the American Chemical Society* **135**, 16833-16836 (2013).

49. Zhu, W.L. et al. Active and Selective Conversion of CO_2 to CO on Ultrathin Au Nanowires. *Journal of the American Chemical Society* **136**, 16132-16135 (2014).

50. Lu, Q. et al. A selective and efficient electrocatalyst for carbon dioxide reduction. *Nat. Commun.* **5** (2014).

51. Hoshi, N., Kato, M. & Hori, Y. Electrochemical reduction of CO_2 on single crystal electrodes of silver Ag(111), Ag(100) and Ag(110). *J. Electroanal. Chem.* **440**, 283-286 (1997).

52. Gattrell, M., Gupta, N. & Co, A. A review of the aqueous electrochemical reduction of CO_2 to hydrocarbons at copper. *J. Electroanal. Chem.* **594**, 1-19 (2006).

53. Kuhl, K.P., Cave, E.R., Abram, D.N. & Jaramillo, T.F. New insights into the electrochemical reduction of carbon dioxide on metallic copper surfaces. *Energ. Environ. Sci.* **5**, 7050-7059 (2012).

54. Hori, Y., Takahashi, I., Koga, O. & Hoshi, N. Electrochemical reduction of carbon dioxide at various series of copper single crystal electrodes. *J. Mol. Catal. A Chem.* **199**, 39-47 (2003).

55. Lee, H.E. et al. Concave Rhombic Dodecahedral Au Nanocatalyst with Multiple High-Index Facets for CO_2 Reduction. *ACS Nano* **9**, 8384-8393 (2015).

56. Li, C.W. & Kanan, M.W. CO_2 Reduction at Low Overpotential on Cu Electrodes Resulting from the Reduction of Thick Cu_2O Films. *Journal of the American Chemical Society* **134**, 7231-7234 (2012).

57. Chen, Y.H., Li, C.W. & Kanan, M.W. Aqueous CO_2 Reduction at Very Low Overpotential on Oxide-Derived Au Nanoparticles. *Journal of the American Chemical Society* **134**, 19969-19972 (2012).

58. Bassham, J.A. et al. The Path of Carbon in Photosynthesis .21. The Cyclic Regeneration of Carbon Dioxide Acceptor. *Journal of the American Chemical Society* **76**, 1760-1770 (1954).

59. Lorimer, G.H. The Carboxylation and Oxygenation of Ribulose 1,5-Bisphosphate - the Primary Events in Photosynthesis and Photo-Respiration. *Annu. Rev. Plant Phys.* **32**, 349-383 (1981).

60. Li, S.H., Yuan, W.M. & Ma, S.M. Highly Regio- and Stereoselective Three-Component Nickel-Catalyzed syn-Hydrocarboxylation of Alkynes with Diethyl Zinc and Carbon Dioxide. *Angew. Chem. Int. Edit.* **50**, 2578-2582 (2011).

61. Fujihara, T., Xu, T.H., Semba, K., Terao, J. & Tsuji, Y. Copper-Catalyzed Hydrocarboxylation of Alkynes Using Carbon Dioxide and Hydrosilanes. *Angew. Chem. Int. Edit.* **50**, 523-527 (2011).

62. Wang, X.Q., Nakajima, M. & Martin, R. Ni-Catalyzed Regioselective Hydrocarboxylation of Alkynes with CO_2 by Using Simple Alcohols as Proton Sources. *Journal of the American Chemical Society* **137**, 8924-8927 (2015).

63. Yu, B., Xie, J.N., Zhong, C.L., Li, W. & He, L.N. Copper(I)@Carbon-

Catalyzed Carboxylation of Terminal Alkynes with CO_2 at Atmospheric Pressure. *ACS Catalysis* **5**, 3940-3944 (2015).

64. Huguet, N. et al. Nickel-Catalyzed Direct Carboxylation of Olefins with CO_2: One-Pot Synthesis of alpha,beta-Unsaturated Carboxylic Acid Salts. *Chem-Eur. J.* **20**, 16858-16862 (2014).

65. Ostapowicz, T.G., Schmitz, M., Krystof, M., Klankermayer, J. & Leitner, W. Carbon Dioxide as a C-1 Building Block for the Formation of Carboxylic Acids by Formal Catalytic Hydrocarboxylation. *Angew. Chem. Int. Edit.* **52**, 12119-12123 (2013).

66. Wu, L.P., Liu, Q., Fleischer, I., Jackstell, R. & Beller, M. Ruthenium-catalysed alkoxycarbonylation of alkenes with carbon dioxide. *Nat. Commun.* **5** (2014).

67. Ishida, N., Masuda, Y., Uemoto, S. & Murakami, M. A Light/Ketone/Copper System for Carboxylation of Allylic C-H Bonds of Alkenes with CO_2. *Chem-Eur. J.* **22**, 6524-6527 (2016).

68. Julia-Hernandez, F., Moragas, T., Cornella, J. & Martin, R. Remote carboxylation of halogenated aliphatic hydrocarbons with carbon dioxide. *Nature* **545**, 84-+ (2017).

69 Moore, D. R., Cheng, M., Lobkovsky, E. B. & Coates, G. W. Mechanism of the alternating copolymerization of epoxides and co2 using b-diiminate zinc catalysts: evidence for a bimetallic epoxide enchainment. *J. Am. Chem. Soc*. **125**, 11911−11924 (2003).

70. Coates, G. W. & Moore, D. R. Discrete metal-based catalysts for the copolymerization of CO_2 and epoxides: discovery, reactivity,

optimization,and mechanism. *Angew. Chem. Int. Ed.* **43**, 6618−6639 (2004).

71. Sakakura, T. & Kohno, K. The synthesis of organic carbonates from carbondioxide. *Chem. Commun.* **11**, 1312−1330 (2009).

72. Nakano, K., Kobayashi, K., Ohkawara, T., Imoto, H. & Nozaki, K. Copolymerization of epoxides with carbon dioxide catalyzed by iron–corrole complexes: synthesis of a crystalline copolymer. *J. Am. Chem. Soc.* **135,** 8456–8459 (2013).

73. Nozaki, K., Nakano, K. & Hiyama, T. Optically active polycarbonates: asymmetric alternating copolymerization of cyclohexene oxide and carbon dioxide. *J. Am. Chem. Soc.* **121**, 11008–11009 (1999).

74. Clements, J. H. Reactive applications of cyclic alkylene carbonates. Ind. Eng.Chem. Res. 42, 663−674 (2003). 13. Jin, L. et al. Metal porphyrin/phenyltrimethylammonium tribromide: high efficient catalysts for coupling reaction of CO2 and epoxides. *J. Mol. Catal. A Chem*. **261**, 262−266 (2007).

75. Ema, T., Miyazaki, Y., Koyama, S., Yano, Y. & Sakai, T. A bifunctional catalyst for carbon dioxide fixation: cooperative double activation of epoxides for the synthesis of cyclic carbonates. *Chem. Commun*. **48**, 4489−4491 (2012).

76. Kember, M. R., Knight, P. D., Reung, P. T. R. & Williams, C. K. Highly active dizinc catalyst for the copolymerization of carbon dioxide and cyclohexene oxide at one atmosphere pressure. *Angew. Chem. Int. Ed.* **48**, 931−933 (2009).

77. Whiteoak, C. J. et al. A powerful aluminum catalyst for the synthesis of highly functional organic carbonates. J. Am. Chem. Soc. 135, 1228−1231 (2013). 20. Liang, S. et al. Highly efficient synthesis of cyclic carbonates from CO_2 and epoxides over cellulose/KI. *Chem. Commun*. **47**, 2131−2133 (2011).

78. Cheng, M., Lobkovsky, E. B. & Coates, G. W. Catalytic reactions involving C1 feedstocks: new high-activity Zn(II)-based catalysts for the alternating copolymerization of carbon dioxide and epoxides. *J. Am. Chem. Soc*. **120**, 11018−11019 (1998).

79. Liu, Q., Wu, L.P., Jackstell, R. & Beller, M. Using carbon dioxide as a building block in organic synthesis. *Nat. Commun.* **6** (2015).

Chapter 3. Porphyrin decorated gold nanoparticle antenna complex

3.1 Introduction

In the photosynthetic antenna complexes, the net absorbance and the energy transfer efficiency of the antenna complex are determined by the combination of chlorophylls and several accessory pigments. In detail, the overall property of the integrated complex varies as a function of the mutual arrangement and distance in angstrom between the pigment molecules within the complex. Principles that govern the natural arrangement of chlorophylls in antenna complexes impact the net optical property of the complex and are subjects of great research interest.[1] The ability to mimic the natural arrangement of chlorophylls in vitro can inspire designing of artificial antenna complexes for light-based systems such as photosensitizers, photoelectrodes, and light emitting devices.

Recently, various photosynthetic antenna mimetic complexes have been developed, with particular emphasis on the controlled arrangement of pigment molecules. Herein, the porphyrin chromophore has been used as it is the primary pigment of chlorophylls in the natural antenna. The ability to manipulate their spatial alignment, such as precisely controlling the distance between the molecules and their orientation, is a major bottleneck in the system.[2, 3] In natural antenna complexes, chlorophylls are fixed to the designated position by the surrounding helical peptide scaffolds and are assembled into the protein structure. Similarly,

porphyrins can be immobilized in the desired alignment with the support of artificially manufactured scaffolds. So far, various scaffolding materials have been developed for artificial antenna complexes such as metal frameworks,[4, 5] polymer materials,[6, 7] and biomaterials like peptides[8, 9] or DNA[10, 11].

Based on the use of peptides as natural scaffolds, peptoids were recently developed as peptidomimetic templates. Peptoids are bioinspired heteropolymers that are structurally different from peptides due to the presence of nitrogen-bonded side chains instead of the usual α-carbon bonded side chains.[12] Previously, porphyrin decorated peptoid helices were demonstrated as a mimicry of the pigment-peptide scaffold in photosynthetic antenna.[13] Use of peptoids as functional scaffold molecules enables convenient management of the net sequence and decoration of side chains with functional components. This is achieved by use of post-functionalized monomers as building blocks in the submonomer method, which arranges the net sequence by step-wise monomer addition.[14] Thus, porphyrins are accurately conjugated to the desired position of peptoid helices and porphyrin-peptoid conjugates (PPCs) are formed. The distance and angle between the porphyrins are fixed on the peptoid template, which has a helical twist of 120° (3 monomers per turn) and a pitch length of 6 Å. Considering that the average distance between pigments in the natural antenna is ~10 Å,[15] success in achieving precise alignment of chromophores in a peptoid scaffold in high resolution is remarkable.

In bulk solutions, PPC exhibited both intramolecular and intermolecular porphyrin interactions via excitonic coupling and π-π stacking.[13] Since these interactions have a cumulative effect on the overall optical properties, it is difficult

to decouple and analyze the effects of intra- and inter-molecular interactions individually. Moreover, intermolecular coupling is affected by solvent concentration and dielectric constants. These hinder the ability to exclusively analyze the effect of molecular alignments on optical properties of peptoids. Particularly, concentration-dependent alterations in absorption spectra are commonly observed in bulk PPCs. For example, there is intermolecular π-π stacking in self-assembled molecules, which induces formation of porphyrin J-aggregates.[16] Intramolecular coupling in these systems is determined by exciton-coupled circular dichroism, which, however, provides limited and indirect evidence of excitonic couplings as the signals are affected by intermolecular interactions. Therefore, to comprehend the relationship between porphyrin configuration and the net optical property of the scaffolds without interference from intra- and inter-molecular interactions, better templates should be generated.

Here, we developed a novel porphyrin-peptoid hybridized metal nanoparticle as a platform for the study of porphyrin-based antenna. Inspired from the natural protein, we succeeded to manage molecular configuration of porphyrins in few angstrom range by conjugating them on the peptoid scaffold. Furthermore, to prevent the intermolecular aggregation, we fixed PPCs on the nanoparticle template. Therefore, our hybrid template enabled porphyrins to maintain designated molecular configuration and simultaneously immobilized into the antenna assembly. This resembles the role of protein scaffolds in natural antennae—prevention of concentration-dependent quenching of chlorophylls and maintenance of intrinsic efficiency at dense pigment concentrations.

For the practical investigation of optical property, we introduced

plasmonic metal as a core of the nanoparticle. Under the effect of plasmon, both excitation and emission of fluorescence spectra was significantly altered. Here surprisingly, distinctive change of fluorescence was observed among porphyrin molecules having different configurations. In detail, we showed two factors in designing the porphyrin arrangement indeed affect the fluorescence signal: (1) the conjugating orientation of porphyrin on the nanoparticle surface, and (2) the inter-porphyrin distance on peptoid branch. Particularly, the porphyrin sample having its inter-porphyrin distance of 6 angstrom on a peptoid showed the most distorted fluorescence emission. The amplified inter-porphyrin interaction at very close distance can be understand in the same context of efficient energy transfer between closely located chlorophyll pairs in the photosynthetic antennas.

Moreover, the plasmon-modified fluorescence showed significantly distinctive feature when the plasmon resonance wavelength of gold core was changed. This demonstrates that plasmon effect can be not only used as a sensing tool, but also utilized as a powerful technique for mechanistic study on intermolecular interaction. In this thesis, based on the overall tendency in fluorescence modifications, we proposed possible mechanism for the fluorescence results in the aspect of energy interaction between porphyrin-metal or/and porphyrin-porphyrin. Because our template has versatility at constructing various designated conditions in porphyrin alignment and plamon effect, we believe the strategy can be applied to further profound studies on material design in porphyrin-based antenna.

3.2 Experimental and analysis

3.2.1 Materials

L-Arginine (99%) and ethylene glycol (99.5%) were purchased from Junsei Chemical. Tetraethyl orthosilicate (TEOS, 99%), poly(diallyldimethylammonium chloride) solution (pDADMAC, 20wt% in water), tetrachloroauric (III) trihydrate ($HAuCl_4 \cdot 3H_2O$, 99.9%), sodium silicate solution (27 wt%) and N,N-diisopropylethylamine (DIEA, 99.5%) were purchased from Sigma-Aldrich. Succinic anhydride (99%) and 3-aminopropyltriethoxysilane (99%) were purchased from Acros Organics. Isopropyl alcohol (99.9%), 1-ethyl-3-(3-dimethylaminopropyl)carbodiimide (EDC, 98%) and N-hydroxysuccinimide (NHS, 98%) were purchased from Tokyo Chemical Industry. Cyclohexane (99.5%), ethanol (anhydrous, 99.5%), N,N-dimethylformamide (DMF, 99.5%), ammonia solution (28%) and hydrochloric acid (HCl, 35%) were purchased from Deajung Chemicals. High purity deionized water (18.2 $MWcm^{-1}$) was used in the procedures.

3.2.2 PPC synthesis

Peptoid sequences were synthesized using a microwave-assisted solid-phase submonomer synthesis method[14] with a CEM MARS multimodal microwave reactor equipped with a fiber-optics temperature probe and a magnetic stirrer (CEM Corp., Matthews, NC, USA). Prepared reaction mixture in a cartridge was stirred and irradiated at different reaction conditions under atmospheric pressure while the

temperature probe positioning in the cartridge. An Fmoc-Rink amide MBHA resin (0.59 mmol/g, Novabiochem, San Diego, CA, USA) was used to obtain *C*-terminal amide peptoids. To begin with, resin (0.42 g, 0.25 mmol) was swelled in DMF for 20 minutes and then Fmoc deprotection was conducted by treating 20% (v/v) piperidine in DMF (10 ml) two times for 5 and 20 minutes, respectively. After Fmoc was removed, each monomer for target peptoid was sequentially added by a series of bromoacetylation and displacement of bromide by a primary amine, which was repeated until the desired peptoid sequence was obtained. In our case, (*S*)-*N*-(1-phenylethyl)glycine (*N*spe) was mainly used as a primary amine to achieve a right-handed helical structure which is generated and well-maintained when steric and electronic interactions between the backbone amides and α-chiral aromatic side chain exist.[2] For conjugating porphyrin, mono-Mmt protected 1,4-diaminobutane (*N*Lys(Mmt)) was added at the position of porphyrin incorporation. Bromoacetylation was performed with bromoacetic acid (4.18 ml of 1.2 M bromoacetic acid in DMF stock solution, 5 mmol) and *N,N'*-diisopropylcarbodiimide (0.63 g, 0.78 ml, 5 mmol), stirred and irradiated at 35 °C (microwave, 400 W 15% power, ramp 0.5 minutes) for 2 minutes. For the displacement step, *N*spe (5 ml of 2.0 M in NMP stock solution, 10 mmol) or *N*Lys(Mmt) (5 ml of 1.0 M in NMP stock solution, 5 mmol) was added according to desired peptoid sequence, and stirred and irradiated at 80 °C (microwave, 400 W 75% power, ramp 2 minutes) for 1.5 minutes. The resin was completely washed with DMF and DCM between each step

To resin-bound peptoid (0.16 mmol) was added a solution of Fmoc-Gly-OH (0.19 g, 0.64 mmol) and HBTU (0.30 g, 0.8 mmol) dissolved in DMF (2 ml)

each, followed by adding DIEA (0.28 ml, 1.6 mmol) dropwise. The reaction mixture was stirred and kept for 2 hours at room temperature, and then the resin was thoroughly washed using DCM, DMF and MeOH. The coupling reaction was repeated for 2 hours and overnight to obtain higher yield.

Mmt deprotection was firstly performed on resin-bound peptoid with 0.75% TFA solution (DCM : TFA : TIS = 94.25 : 0.75 : 5). The TFA solution (6 ml) was treated for 2 minutes at room temperature and the resin was washed with DCM after draining orange colored solution. These steps were repeated more than 5 times until the drained solution became colorless. Porphyrin conjugation was achieved by NHS ester coupling reaction with TPP-NHS ester which was prepared by reported method.[3] After washing the resin-bound peptoid with the solution of DCM (4 ml) and DIEA (0.15 ml) for 1 minute to remove residual TFA, TPP-NHS ester (150 mg, 0.20 mmol) in DCM (7 ml) was added to the resin followed by the addition of DIEA (0.07 ml, 0.40 mmol). The reaction mixture was sealed and stirred for overnight under N_2 atmosphere. The resin was thoroughly washed and then treated with 20% (v/v) piperidine in DMF (10 ml) twice for 5 and 20 minutes to remove *N*-terminal Fmoc. After Fmoc deprotection, peptoids were cleaved from resin using 95 % TFA solution (DCM : TFA = 5 : 95), stirred for 10 minutes. Obtained crude solution was filtered by solid-phase extraction (SPE) cartridge with 20μ hydrophobic polyethylene frits (Applied separations, Allentown, PA, USA) and was lyophilized. Peptoids with >98% purity were obtained after chromatography purification, and were analyzed by analytical high performance liquid chromatography (HPLC) and electrospray ionization mass spectrometer (ESI-MS). The HPLC and ESI-MS results are shown in **Figure 3.1** and **Table 3.1** respectively.

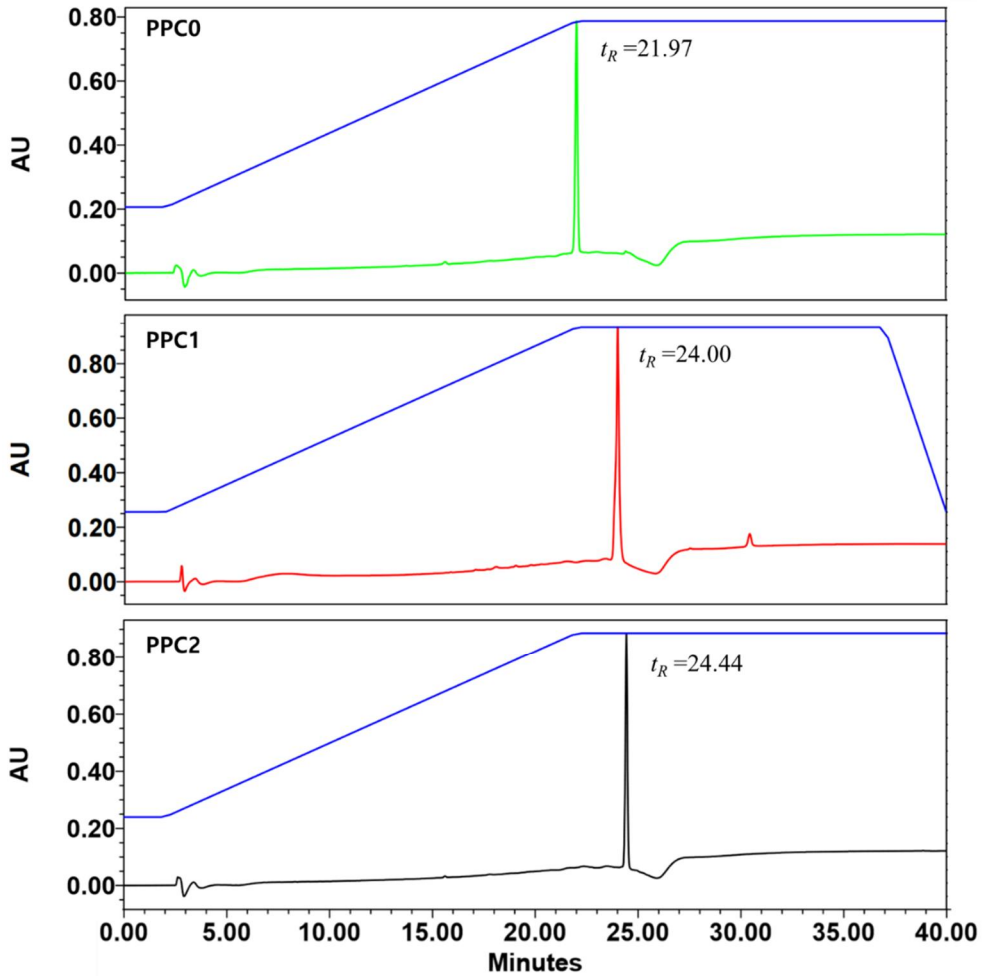

Figure 3.1. HPLC chromatogram of PPCs monitored at 220 nm.

Table 3.1. ESI-MS data of PPCs

Compounds	Mass calculated	Mass observed[a]
PPC0	2131.04	2132.12 (H^+), 2154.10 (Na^+)
PPC1	2738.28	2739.28 (H^+), 2761.26 (Na^+)
PPC2[b]	3221.53	1611.83 ($2H^+$), 1074.89 ($3H^+$)

[a] Observed in ESI-MS. [b] Singly charged species were not observed due to the mass range of instrument (up to *m/z* 3000). Observed masses are not fragments, doubly ($2H^+$) and triply ($3H^+$) charged peaks.

3.2.3 Synthesis of silica nanoparticles

Silica nanoparticles were synthesized as previously reported with minor modifications.[17] First, very uniform silica seeds of 24 nm were synthesized. Briefly, 9.1 mg of L-arginine was put in 6.9 ml water and 0.45 ml cyclohexane was added. The mixture was heated to 60 °C under mild stirring, 0.55 ml TEOS was added and the reaction mixture was stirred continuously for 20 h maintaining the temperature at 60 °C. To regrow the silica seeds to 40 nm size, 2 ml of the prepared seed solution was mixed with 14.4 ml water, 2.2 ml cyclohexane, and 2 ml TEOS. The mixture was stirred mildly for 30 h at 60 °C. Finally, the silica nanoparticles were regrown to 130 nm by mixing 0.7 ml of as-prepared solution with 3.5 ml water, 2.8 ml ammonia solution (28%), and 11.7 ml ethanol. To this solution, 1 ml TEOS was added with a syringe pump at a rate of 0.6 ml/h. Finally, the particles were washed thrice with ethanol and dried in a 50 °C oven overnight and stored at room temperature.

3.2.4 Synthesis of AuNPs

Octahedral AuNPs were synthesized as previously reported with minor modifications.[18] For a pot, 0.6 ml pDADMAC, 0.3 ml HCl 12.5 % (v/v), and 30 µl of 0.5 M $HAuCl_4 \cdot 3H_2O$ were mixed with 30 ml ethylene glycol in a 100 ml glass vial and stirred vigorously for 20 min. The vial was sealed and put in an oil bath and heated up to 192 °C or 194 °C for Au(590) or Au(650) synthesis, respectively, without stirring. The mixture was allowed to react for 35 min and cooled at room temperature for 2 h. To wash the synthesized gold, 60 ml of ethanol was added to

the solution, and the particles settled after centrifugation at 3900 rpm for 30 min. The particles were further washed thrice with ethanol and finally, with water. Based on the amount of $HAuCl_4 \cdot 3H_2O$ precursor in a pot (15 μmol) and final size of octahedral AuNPs, calculated amount of final AuNPs in a pot was approximately ~10^{11} particles.

3.2.5 Silica coating on AuNPs

Silica coating was performed in two sequential steps, by using sodium silicate[18] and TEOS,[19] respectively, as precursors. First, 66.5 μl of sodium silicate solution (27 % wt) was mixed with 25 ml water, and as-synthesized AuNPs were dispersed in the silicate solution. The mixture was heated to 90 °C in a water bath and allowed to react for 1.5 h under vigorous stirring. For 2 nm thick silica layer, the $Au@SiO_2$ solution was washed in ethanol in this stage. After completion of the reaction, the solution was cooled to room temperature and washed 3 times with water and finally with ethanol. For further coating with TEOS, silicate-coated AuNPs were dispersed in a mixture containing 14 ml ethanol, 5 ml water, 6 ml isopropyl alcohol, and 0.24 ml ammonia solution (28%). Then, 1 μl TEOS diluted to 10 % (v/v) in ethanol was dissolved in the solution and allowed to react for 20 h in a shaker. $Au@SiO_2$ particles showed 11 nm thick silica layer after the process. To further increase the silica thickness, 1 μl TEOS diluted to 10 % (v/v) in ethanol was additionally dissolved in the solution after 2 h from the first injection of TEOS and allowed to react for 20 h in a shaker. $Au@SiO_2$s were washed thrice with ethanol and directly used in the dye-linking process.

3.2.6 Carboxylation on silica surface

The surface of the silica particles was functionalized with carboxylic acid groups, as described previously.[20] Briefly, carboxylic acid silane was synthesized by dissolving 450 mg of succinic anhydride into the mixture of 0.5 ml DMF, 1ml ethanol, and 1.05 ml APTES. The solution was incubated in a shaker and used after 20 h. Usually, 10^{11} nanoparticles were used in one pot which corresponds to 0.57 mg of dried silica nanoparticles or the amount of a pot in AuNPs synthesis. The particles were dissolved in a mixture of 8 ml ethanol and 2 ml water, to which 1.5 ml carboxylic acid silane solution was added. The solution was allowed to react for 2 h under mild stirring at room temperature, and further in a 50 °C water bath for 1 h. The functionalized particles were washed twice with ethanol and finally with DMF.

3.2.7 EDC/NHS coupling

The carboxylated nanoparticles (~10^{11} particles) were dispersed in 30 µl DMF. EDC and NHS solutions were prepared by dissolving 2 mg EDC and 1.5 mg NHS in 90 µl and 7.5 µl DMF, respectively. The EDC solution was mixed with the particles and NHS solution was added after 5 min. The mixture was shaken vigorously for 2 h at room temperature and washed thrice with DMF and dispersed in 20 µl DMF. For TPP linking, 0.15 µl DIEA and 0.15 µl of 5 mM TPP stock in DMF was applied in the particle solution. For PPC linking, 0.75 µl DIEA and 0.75

μl of 5 mM PPC stock in DMF was put in the particle solution, and finally all the mixtures were vigorously shaken overnight. The final dye-linked particles were washed thrice in DMF before the characterizations.

3.2.8 Analytical methods

The TEM micrographs were observed using a JEM 2100F (JEOL, Tokyo, Japan) microscope, operating at 200 kV. Samples were prepared by dropping the particle solutions onto carbon supported film grids and dried in air. For the FESEM micrographs, a Zeiss SUPRA 55VP (Zeiss, Oberkochen, Germany) was used operating at 2 kV. The samples were prepared by dropping the particle solutions onto washed silicon wafers and dried in air.

The UV/Visible absorption spectra of samples were measured using a NanoDropTM2000c and a spectroscopic cuvette. The samples were dissolved in their final solution, generally DMF, and placed in a 1 ml quartz cuvette for analysis. The fluorescence was measured using a PTI QuantaMasterTM spectrofluorometer, QM4 (Photon Technology International, Birmingham, NJ) at room temperature. The samples were dissolved in DMF and placed in a quartz cuvette. Typically, excitation spectra was taken with a 715 nm emission, a scan range of 370-670 nm and a step size of 1 nm. Also, emission spectra was taken with a 418 nm excitation, a scan range of 600-800 nm and a step size of 1 nm.

3.3 Results and discussion

3.3.1 Silica nanoparticle linked PPCs

We used tetraphenylporphyrin (TPP), a metal-free heterocyclic porphyrin (inset in **Figure 3.2**), as the target porphyrin molecule. Absorption and fluorescence emissions were measured and the spectra were plotted (**Figure 3.3**). In the absorption spectra, a large Soret band at 418 nm and four Q-bands (Q1, Q2, Q3, and Q4) at 513 nm, 550 nm, 590 nm, and 645 nm were observed.[21] In the fluorescence spectra, two emission peaks at 650 nm and 715 nm were detected and marked as E650 and E715, respectively. To clearly indicate which energy level transition corresponds to the absorptions and emissions, each absorption and emission process was illustrated in the energy level diagram of TPP (**Figure 3.4**). As depicted in figure 1c, the Soret and Q-bands respectively originate from the S0 → S2 and S0 → S1 electronic transitions, and the fluorescence emissions arise from S1 → S0 energy relaxation.[21]

Three PPCs decorated with TPP were synthesized by the previously reported submonomer method.[14] At the N-terminal of peptoids, glycine was linked to utilize the amino group in the conjugation processes. **Figure 3.2** shows a schematic representation of each PPC and their chemical structures. To investigate the effect of neighboring porphyrins, one TPP-conjugated peptoid (PPC0) and two TPP-conjugated peptoids (PPC1, PPC2) were constructed. PPC1 and PPC2 were designed to have their inter-porphyrin distance as one pitch (6 Å) and two pitches (12 Å) of the peptoid helix, respectively. Thus, the intramolecular alignment of

TPPs in the two PPCs ensured a parallel face-to-face orientation and permitted distinction in their distance. The products were analyzed by high performance liquid chromatography and electrospray ionization mass spectrometer as discussed in experimental part.

According to our previous observation, TPP and PPCs exhibit differences in absorption in bulk solution.[13] Compared to TPP, the absorption of PPCs showed a broader Soret band and a bathochromic shift. Another important observation was that the occurrence of the bathochromic shift depended on the nature and concentration of the PPCs. For example, PPC1 showed a noticeable color change from bright purple to green when the concentration increased from 0.2 mM to 1.0 mM. This indicated that the molecules assembled into J-aggregates in the bulk solvent. Therefore, prior to investigating the effect of SPR, we immobilized TPP and PPCs on solid templates to prevent intermolecular aggregation and retain the original optical property of the porphyrin. Among solid templates, silica was chosen because it is optically inert and easy to synthesize.

Silica nanoparticles were synthesized by the modified Stöber method[17] and functionalized with carboxylic acid groups. Then, TPP and PPCs were conjugated to the silica nanoparticles via EDC/NHS coupling that created amide bonds between the carboxyl group of silica and the amine groups of TPP and PPCs. The overall procedure is schematically represented in **Figure 3.5**. Finally, TPP- and PPC-linked silica nanoparticles were rinsed in fresh dimethylformamide to remove unlinked porphyrins. The size and shape of the silica nanoparticles were investigated by FESEM as shown in **Figure 3.6**. The final particles were uniformly spherical in shape with a diameter of 130 nm. In addition, the approximate number

of linked porphyrins on the silica nanoparticles was calculated by subtracting the number of unlinked porphyrins from that of the original reactants. By controlling the final activation time of EDC/NHS coupling, all TPP- and PPCs-linked silica nanoparticles were synthesized to have same amount of porphyrins on a silica nanoparticle. Approximately, 1400 porphyrin molecules were linked on a particle, which equals 1400 molecules of TPP or PPC0, and 700 molecules of PPC1 or PPC2. Considering the surface area of 130 nm silica sphere, the porphyrin density corresponds to an intermolecular distance of ~15 nm for TPP or PPC0, and ~21 nm for PPC1 or PPC2. In case of PPCs, since their full length is approximately 2 nm, the calculated intermolecular distance is presumed to be long enough to prevent aggregation.

The absorption spectra of the synthesized samples were compared with that of free TPP as shown in **Figure 3.7 (a)**. As expected, the peaks in the absorption spectra from TPP-silica and PPC-silica nanoparticles had identical position and intensities as that of free TPP. The result shows that the silica template successfully prevented intermolecular aggregation which is observed in free porphyrins. We found that slight increments in the spectral baseline resulted from reflection of the incident radiation from silica. The fluorescence emission of TPP- and PPC-silica nanoparticles also matched with that of free TPP (**Figure 3.7 (b)**). Therefore, we concluded that TPP and PPCs on silica nanoparticle can be a good platform to study the effect of intramolecular alignment of porphyrin.

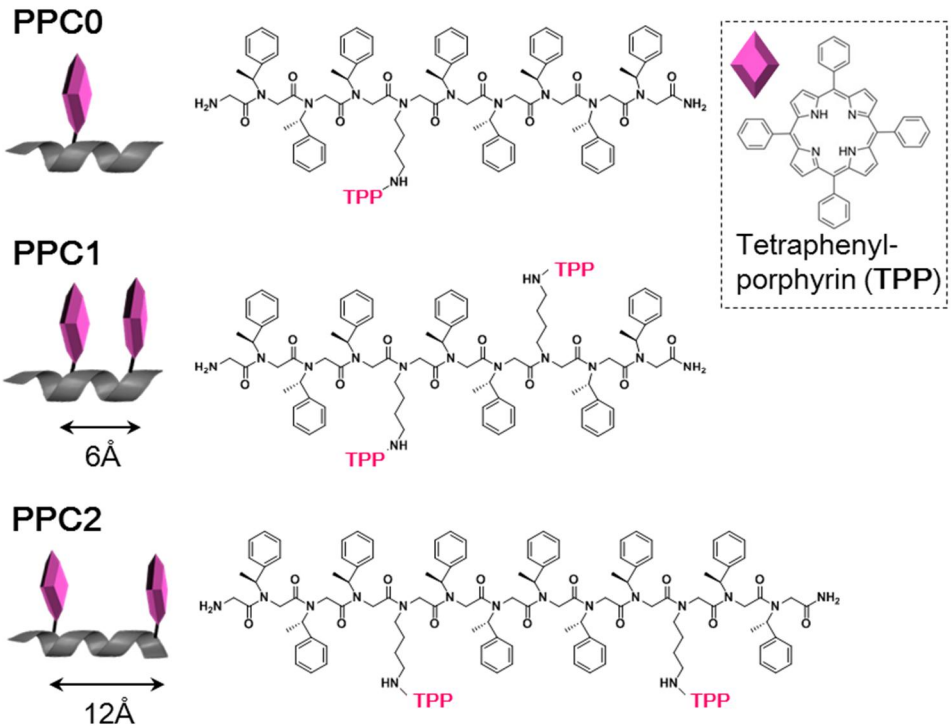

Figure 3.2. Schematic representations and chemical structures of the porphyrin samples—TPPs and PPCs—used in the study.

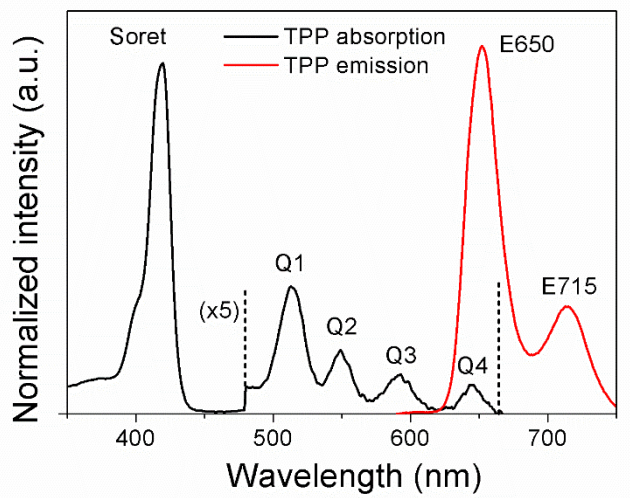

Figure 3.3. Absorption (black) and fluorescence emission (red) spectra of TPP. One Soret and four Q-bands in the absorption spectra, and two emission peaks in the fluorescence spectra, respectively, are marked.

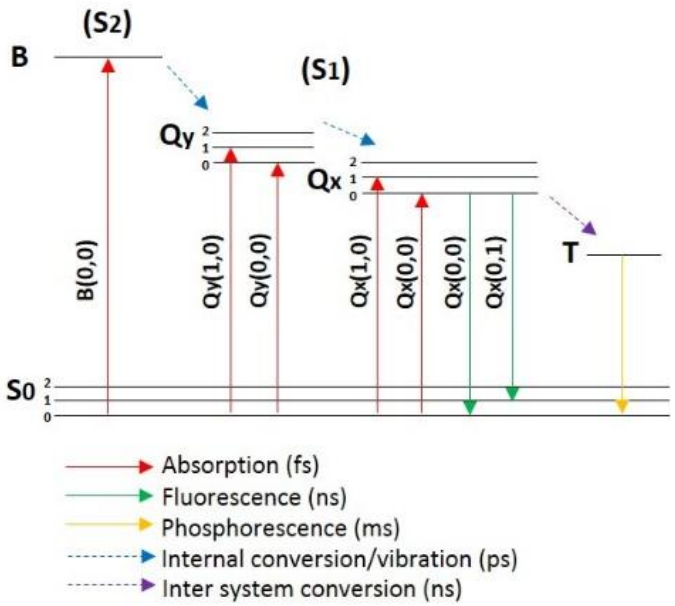

Figure 3.4. Schematic energy diagram of TPP. Red arrows depict the electronic transitions during absorption and green arrows depict the energy relaxation during fluorescence.

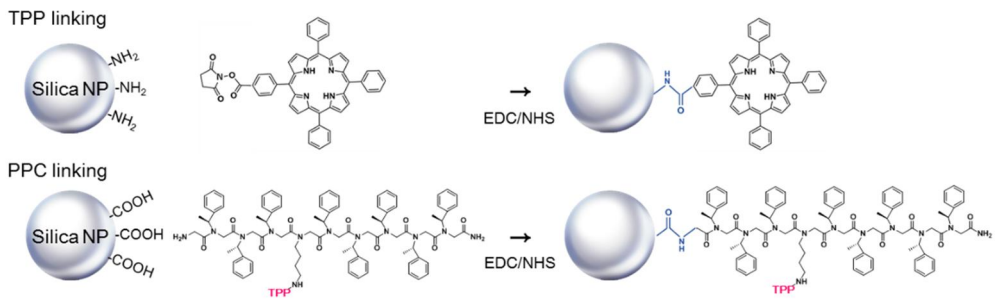

Figure 3.5. Schematic showing the procedure for synthesizing TPP- and PPC-linked silica nanoparticles.

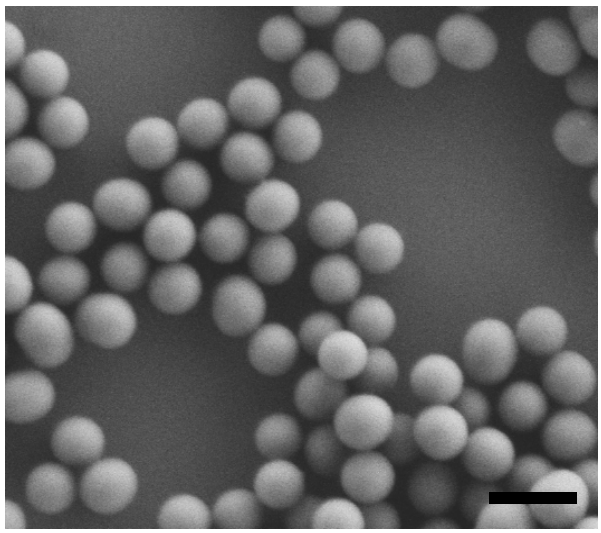

Figure 3.6. SEM image of silica nanoparticles. Scale bar = 200 nm.

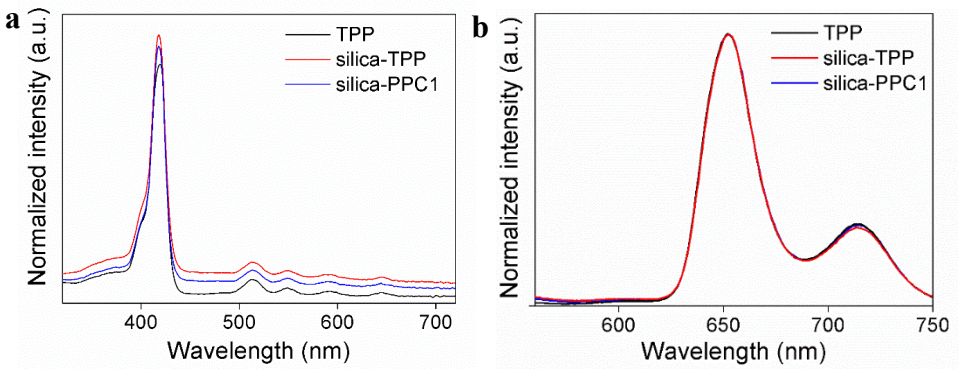

Figure 3.7 (a) Absorption spectra and (b) Fluorescence emission spectra of TPP and PPC1-linked silica nanoparticles (λex = 418 nm, Soret band).

3.3.2 Silica coated gold nanoparticle linked PPCs

Based on the successful development of porphyrin-linked silica, we next introduced AuNPs into the nanoparticle template. After the synthesis of Au@SiO_2, next process of linking porphyrins to silica surface followed analogous procedure to that of porphyrin-linked silica nanoparticles. The detailed experimental protocol is summarized schematically in **Figure 3.8**. Core AuNPs were synthesized by a previously reported method with modifications[22] and observed under FESEM (**Figure 3.9 (a)**) and TEM (**Figure 3.9 (b)**). The core particles were octahedral-shaped with a height of 100 to 110 nm. Absorption of the sample was also measured at regular intervals during synthesis to monitor the procedure. **Figure 3.10** shows measured absorption spectra of AuNPs which have their SPR peak at 650 nm. The as-synthesized AuNPs showed a large absorption peak that corresponded to its SPR wavelength. After application of the silica coating, the absorption peak broadened and the baseline increased, particularly at longer wavelengths. Finally, in TPP-linked Au@SiO_2, a new absorption peak at 418 nm emerged in the spectrum, which corresponds to the Soret absorption of TPP.

We firstly analyzed the effect of metal-dye distance on plasmon enhanced fluorescence by controlling silica thickness. Since direct linking of the dye to the plasmon metal can induce energy quenching, the dye and metal should be maintained at moderate distances.[23, 24] Previous studies have demonstrated that the optimal metal-dye distance required to obtain maximum plasmon-induced emission ranges between 8 and 20 nm.[25-27] Here, we coated silica layer on AuNPs (SPR position = 650 nm) with three different thicknesses of 2 nm, 11 nm and 20 nm to screen optimal dye-metal distance in our template. **Figure 3.11 (a)** is TEM image

of each Au@SiO_2 which clearly shows homogeneous silica layer coated on the core AuNPs. We finally linked TPP to the silica surface and measured fluorescence excitation at an emission wavelength of 715 nm (**Figure 3.11 (b)**). Compared to the spectrum of free TPP excitation, the excitation peaks corresponding to the wavelengths of one Soret and four Q-bands were clearly observed for TPP-linked Au@SiO_2, and the peak intensities increased due to plasmon effect from the AuNPs. The relative enhancement to free TPP gradually increased as the wavelength of Q-band gets closer to Q4. This indicates that plasmon-enhanced fluorescence in our template is maximized near the SPR wavelength of AuNPs (650 nm) as previous studies on dye-metal system also showed same trend in fluorescence enhancements.[25, 28] We also observed differences in increment tendency between three Au@SiO_2 templates. Au@SiO_2 with a 11 nm thick layer of silica exhibited the most enhanced fluorescence at all Q-band positions. In case of the thicker silica layer of 20 nm, the increment significantly reduced. Thus, we fixed the silica thickness to 11 nm for the following studies on plasmon enhanced fluorescence.

To investigate the effect of SPR wavelength, we synthesized two AuNPs with SPR at 590 nm and 650 nm, and designated as Au(590) and Au(650). Finally, each core AuNPs were coated with a 11 nm thick silica layer and designated as Au(590)@SiO_2 and Au(650)@SiO_2. The TEM images of Au(590)@SiO_2 (**Figure 3.12 (a)**) and Au(650)@SiO_2 (**Figure 3.12 (b)**) show size difference between two core AuNPs, which exhibit their average height of ~95 nm and ~110 nm, respectively. The SPR of Au(590)@SiO_2 corresponded to Q3 absorption, which is expected to modify the excitation pathway at Q3. On the other hand, SPR of

Au(650)@SiO_2 encompassed both Q4 absorption and E650 emissions, which placed the excitation and emission under the influence of SPR simultaneously. The absorption spectra of TPP-linked Au(590)@SiO_2 and Au(650)@SiO_2 are shown in **Figure 3.12 (c)**, where the absorption and emission wavelengths of TPP are highlighted on the spectra. Based on the above observations, the trends in SPR-induced fluorescence modifications as a function of SPR positions were subsequently analyzed.

The fluorescence excitations of TPP- and PPC-Au(590)@SiO_2, and TPP- and PPC-Au(650)@SiO_2 were investigated (**Figure 3.13**). The spectra were scanned from 370 nm to 670 nm at an emission wavelength of 715 nm and the excitation baseline of bare Au@SiO_2s were subtracted from the raw spectra. For direct comparison, numerical enhancement factors (EF) for each TPP- and PPC-Au@SiO_2 were calculated and plotted against that of free TPP (**Figure 3.14**). In every sample, Q-band excitations were significantly enhanced and the EF values gradually increased with increase in the excitation wavelength. We also observed differences in increment tendency between porphyrins on Au(590)@SiO_2 and Au(650)@SiO_2. In detail, all samples exhibited comparable EFs around 1.9 at Q1. At Q2, TPP-Au(590)@SiO_2 showed the largest EF of 9.0, and the rest showed comparable value around 5.0. Notable results were observed at Q3 and Q4 which respectively corresponds to the SPR wavelength of Au(590)@SiO_2 and Au(650)@SiO_2. In case of Q3, porphyrins on Au(590)@SiO_2 exhibited significantly large EFs compared to that on Au(650)@SiO_2 (EF of TPP- and PPC-Au(590)@SiO_2 : 18 and 13; EF of TPP- and PPC-Au(650)@SiO_2 : 13 and 11). In contrast, Au(650)@SiO_2 exhibited larger EF at Q4 (EF of TPP- and PPC-

Au(590)@SiO_2 : 19 and 17; EF of TPP- and PPC-Au(650)@SiO_2 : 24 and 21). This result clearly indicated that enhanced fluorescence excitations were induced by the plasmon effect. Indeed, according to previous studies, the plasmon-enahnced excitation is maximized when absorption wavelengths of fluorophores coincide with the SPR position.[25, 28] Such enhancements are generally explained by an increase in the excitation rate via plasmon-enhanced local electric field.[29-32]

Next, we analyzed the effect of porphyrin configuration on fluorescence excitation by using TPPs and PPCs. When SPRs of the core AuNPs were identical, larger fluorescence excitation enhancement was observed in TPP-Au@SiO_2 (red line in **Figure 3.13**) than in PPC-Au@SiO_2. Meanwhile, differences in excitation among PPCs were not detected. The EF values of TPP-Au@SiO_2 were greater by 21% than the EF values of PPC-Au@SiO_2 at each Q-band (**Figure 3.14**). Considering that absorption was identical for all samples on the nanoparticle template, the modest increase in excitation observed with TPP-Au@SiO_2 could not be easily explained. Although the exact reason is not clear at this stage, we believe that differences in the orientation of porphyrin conjugation on the nanoparticle surface may cause the variation in efficiency of excitation enhancement. While porphyrins in TPP-Au@SiO_2 stand directly and vertically on the nanoparticle surface, porphyrins in PPC-Au@SiO_2, which are decorated on the peptoid branches, can be more unconstrained in their orientation ranging from tilted to horizontal. Previous studies have demonstrated that relative dipole orientations between fluorophore molecules and plasmonic metal can affect both excitation and emission modifications.[33, 34] Thus, differences in the relative orientation of porphyrin and nanoparticle surface between TPP- and PPC-Au@SiO_2 can induce distinct dipole

interactions and result in differential fluorescence enhancement. Measuring the fluorescence spectra after regulating the precise angle of porphyrin-Au@SiO_2 can additionally support the proposed explanation. We are currently designing experiments for addressing this aspect by regulating the sequence of the peptoid scaffold.

Next, we analyzed the fluorescence emission property of all samples. The aim of the analysis was to understand how the optical signals of conjugated porphyrins are affected by their configuration and plasmon effect. The spectra were scanned from 600 nm to 800 nm at the excitation of 418 nm, which exhibits the strongest absorption. **Figure 3.15** depict the spectra from TPP- and PPC-Au(590)@SiO_2, and TPP- and PPC-Au(650)@SiO_2, respectively. From the original spectra, the emission of each bare Au@SiO_2 were subtracted and the intensities were normalized. As shown in absorption spectra of TPP-Au@SiO_2 (**Figure 3.10**), the pure absorbance from attached porphyrin is difficult to be quantified due to the broad absorbance from AuNPs. Therefore, we normalized the emission spectra by the Soret excitation intensity as an alternative to absorbance-based normalization. The normalized shapes of emission spectra from each samples showed excellent reproducibility regardless of the orginal emission intensity. To quantitatively compare the degree of spectral changes between each sample, we defined the E650 to E715 intensity ratio as RE650. The RE650 from all samples are summarized in **Table 3.2**, where the relative values based on the free TPP (RE650 = 3.2) are also indicated. In the most cases, the emission spectra were modified to reduce RE650. In case of Au(590)@SiO_2, the RE650s of all linked PPCs were decreased by 5% compared to that of free TPP. More significant modification was observed in case

of Au(650)@SiO_2, where linked TPP showed a 19% decrease in RE650, and linked PPC0, PPC1 and PPC2 showed 27%, 33%, and 28% decrease in RE650 respectively. The change of fluorescence emission was undetected in the previous cases of bulk porphyrins and silica-linked porphyrins. Thus, the spectral change can be explained by plasmon-enhanced fluorescence emission.

In plasmon/dye-conjugated systems, both radiative and non-radiative decay can be modified in the plasmon-coupled photonic state, and are maximized when the emission wavelength coincides with SPR.[29-32] Increase in radiative decay contributes to enhancement of fluorescence, while increase in non-radiative decay results in quenching of fluorescence. In this result, E650 was relatively quenched compared to that of E715, and the phenomena was remarkable especially when the core metal has its SPR at 650 nm (Au(650)@SiO_2). Thus, plasmon-enhanced fluorescence quenching at 650 nm can be an appropriate mechanism to describe the reduction of RE650 in fluorescence spectra. Moreover, in addtion to the dependency of SPR wavelength, the modification of emission spactra is dependent on the porphyrin configurations. The spectra showed clear difference bewteen TPP and PPCs, and also among PPCs. In detail, among the PPCs on Au(650)@SiO_2, PPC1 (inter-porphyrin distance of 6 Å) showed a 1.2 fold reduction in RE650 than PPC0 (one TPP on a peptoid); RE650 of PPC2 (inter-porphyrin distance of 12 Å) was comparable to that of PPC0. This highlights that strong inter-porphyrin interactions within PPC1 are generated by the SPR effect. In the previous studies on multiple fluorophores/plasmon metal conjugated systems, plasmon-enhanced excitonic energy transfer between fluorophores was observed when the SPR wavelength peak is positioned between the donor emission and the acceptor

absorption wavelengths.[35, 36] As a result, the fluorescence of the net systems were altered in the direction of reduced emission in donor and enhanced emission at acceptor. Moreover, since the rate of the energy transfer is determined by intermolecular distance,[37, 38] the optimal alignment of the multiple fluorophores is the key contributing factor to effective energy interaction. Thus, we suppose that our platform amplified inter-porphyrin interactions under the effect of SPR and even enable to directly observe as spectral variations, especially when inter-porphyrin alignment and SPR wavelength are optimized. In our case, the SPR wavelength of Au(650)@SiO_2 encompasses both Q4 absorption and E650, thus, may provide good condition to facilitate plasmon-enhanced energy interactions. In summary, the spectral modifications of fluorescence on our platform can be attributed from the selective plasmon-enhanced fluorescence quenching at E650 and inter-porphyrin energy interaction. Consequently, distinct fluorescence signals depending on the SPR wavelength and the porphyrin conjugation were detected. To further understand the energy dynamics of the system, investigations of its kinetic properties using time-resolved spectroscopy are underway. In detail, study on the fluorescence lifetime are in progress to verify the origin of plasmon-enhanced fluorescence and presence of plasmon-induced intermolecular energy transfer.

Our result can be also viewed in the context of studies on energy transfer between chlorophyll molecules in photosynthetic antenna. Pioneering work in photosynthetic antenna have pointed out that the distance in angstroms between chlorophyll molecules determines the overall efficiency of energy transfer.[1] For example, recent structural analysis of plant photosystem I (PSI) - light harvesting complex I (LHCI) supercomplex has revealed that adjacent chlorophyll *a* pairs

located at the gap between PSI and LHCI enable the supercomplex to exhibit ~100% EET efficiency.[39, 40] Here, we demonstrated that emission spectra can be changed by solely manipulating inter-porphyrin distances at angstrom ranges. This underlines the importance of correct spatial configuration of porphyrins and their involvement in energy transfer. Therefore, we envision that our platform can serve as a systematic model for understanding material design in antenna complexes.

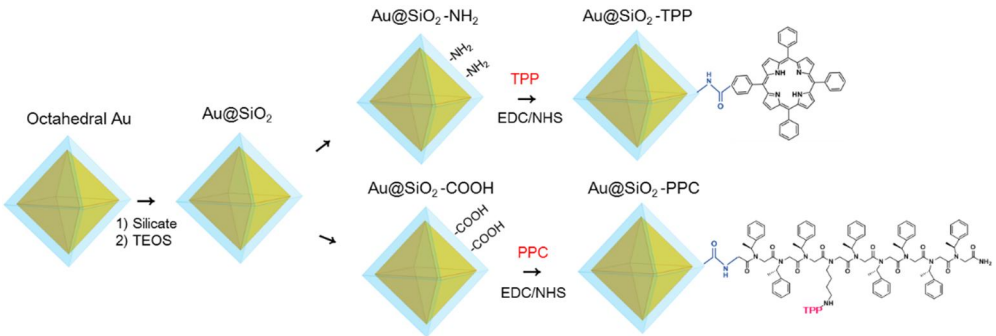

Figure 3.8. Schematic showing the procedure for synthesizing TPP- and PPC-linked Au@SiO_2.

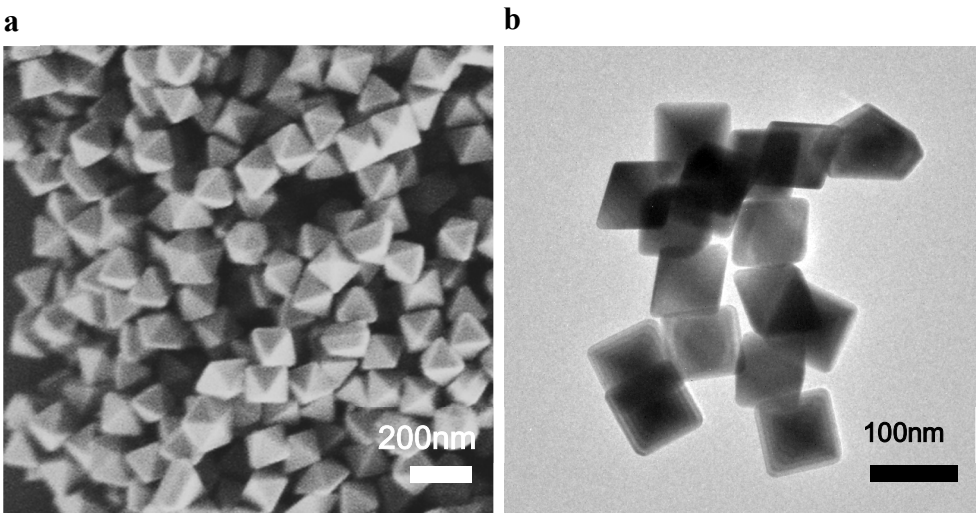

Figure 3.9. (a) FESEM and (b) TEM image of sytnehsized octahedral AuNPs.

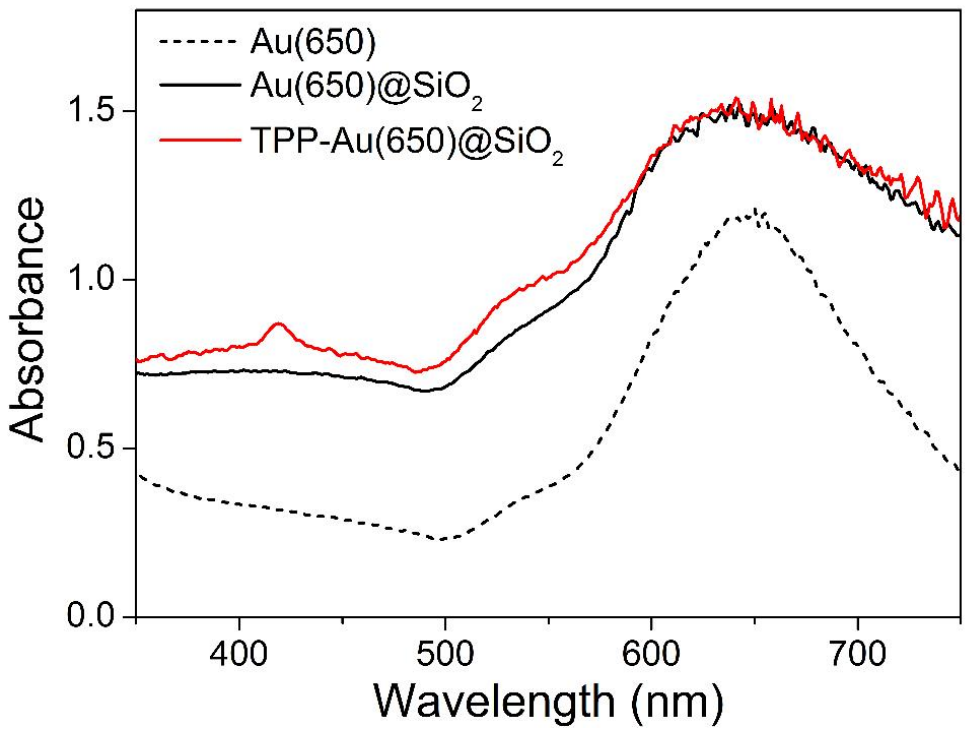

Figure 3.10. Absorption spectra of AuNPs, Au@SiO_2, and TPP-Au@SiO_2.

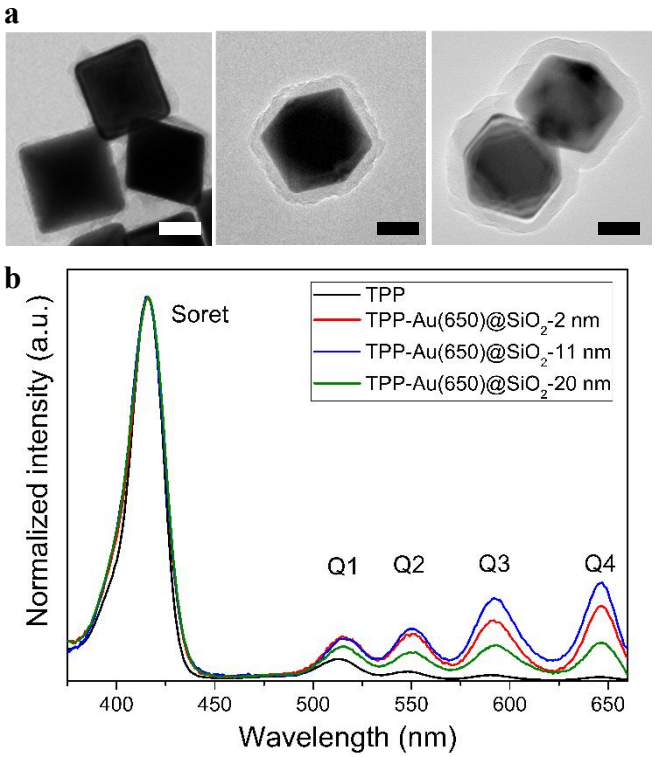

Figure 3.11. (a) TEM images of Au@SiO_2 with silica coating thickness of2 nm (left), 11 nm (middle), and 20 nm (right). Scale bar is 50 nm. (b) Fluorescence excitation spectra (λem = 715 nm) of TPP-Au@SiO_2 with different silica coating thicknesses.

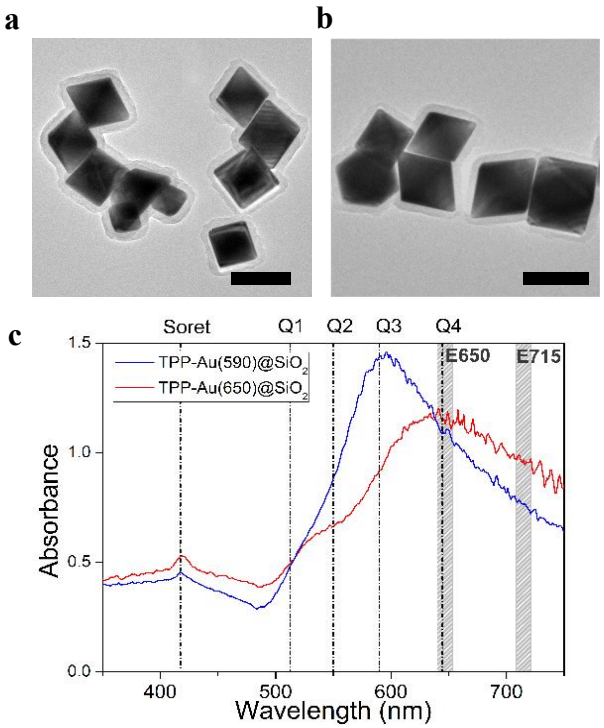

Figure 3.12. TEM image of (a) Au(590)@SiO_2 and (b) Au(590)@SiO_2 (scale bar = 100 nm). (c) Absorption spectra of TPP-Au(590)@SiO_2 and TPP-Au(650)@SiO2. The absorption and fluorescence emission wavelengths of free TPP are marked in the background.

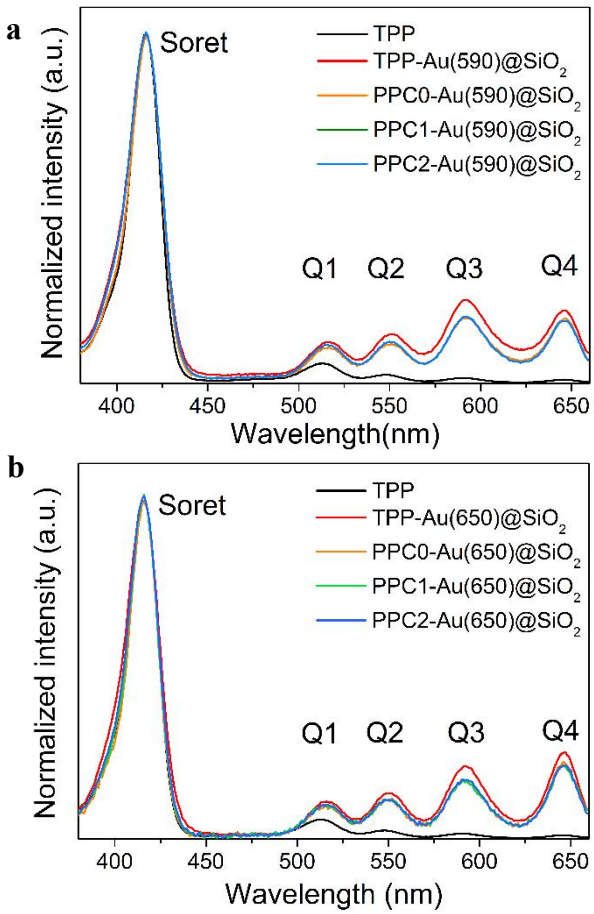

Figure 3.13. Fluorescence excitation spectra (λem = 715 nm) of (a) TPP- and PPCs-Au(590)@SiO_2, and (b) TPP- and PPCs-Au(650)@SiO_2.

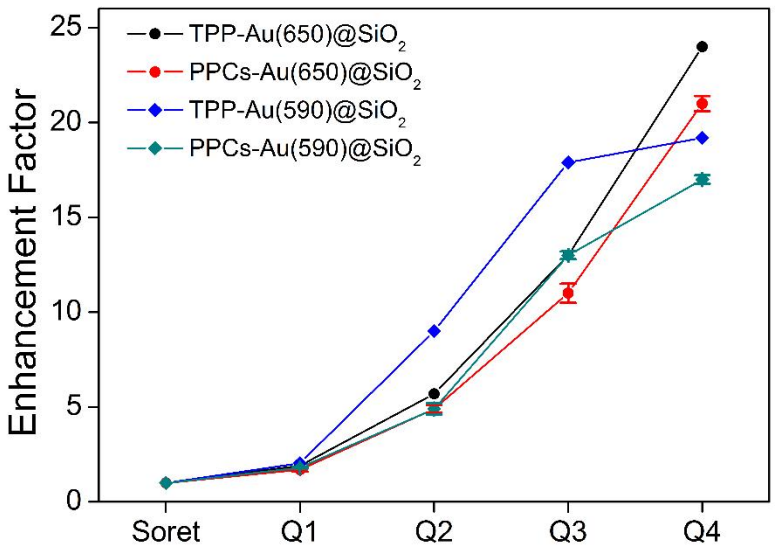

Figure 3.14. Graph showing variation in numerical enhancement factor of fluorescence excitation (versus free TPP) as a function of absorption wavelength.

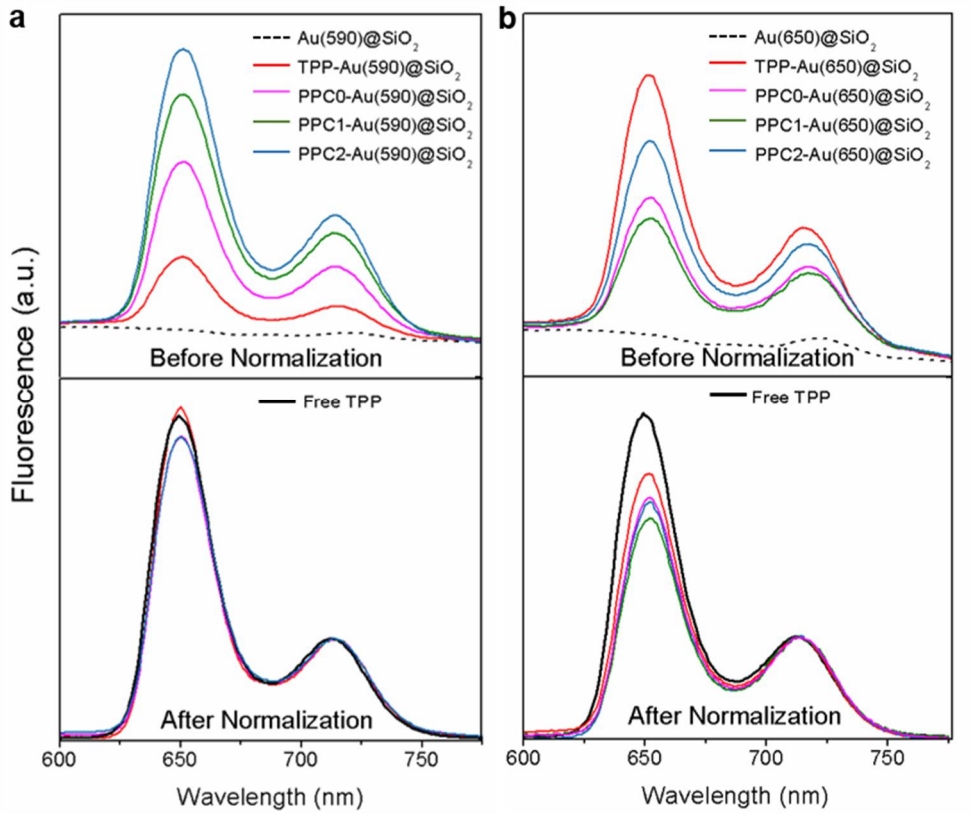

Figure 3.15. Fluorescence emission spectra (λex = 418 nm, Soret band) of (a) TPP- and PPC-Au(590)@SiO_2 and (b) TPP- and PPC-Au(650)@SiO_2.

Table 3.2. RE650 (E650:E715 intensity ratio) value of each porphyrin-linked Au@SiO_2. Releative RE650 based on free TPP (RE650 = 3.2) is expressed in parenthesis.

Porphyrin	Core AuNPs	
	Au(590)	Au(650)
TPP	3.27 (1.02)	2.59 (0.81)
PPC0	3.05 (0.94)	2.35 (0.73)
PPC1	3.04 (0.95)	2.15 (0.67)
PPC2	3.05 (0.94)	2.31 (0.72)

3.4 Conclusion

In conclusion, we fabricated a platform that consists of porphyrin-peptoids hybridized to Au@SiO_2 nanoparticles to analyze the effects of molecular configuration on optical properties of porphyrin-based antenna complexes. The porphyrin molecules were fixed on the nanoparticle template by peptoid branches, which enabled study of the effects of molecular arrangements on optical properties of the platform without any influence of the aggregation among porphyrins. The role of nanoparticles as a structural support for porphyrins was first verified by using silica nanoparticles. Then, we incorporated AuNPs in the nanoparticles to apply SPR effect on porphyrins and measure the modified signals. Indeed, both fluorescence excitations and emissions were significantly changed according to the SPR peak of core AuNPs. In the excitation spectra, the intensity was enhanced up to 24 fold when the SPR peak overlapped with the absorption peak. We also found that the emission spectra were modified in the direction of decreasing RE650, especially on Au(650)@SiO_2. The modification was expected to arise from plasmon-enhanced fluorescence quenching at E650. Moreover, we found that inter-porphyrin distance within PPCs can affect the degree of emission alterations. In case of PPC1, which has an inter-porphyrin distance of 6 Å, the RE650 was decreased by 33%, which was the most reduced value obtained. Considering that the intermolecular distance of photosynthetic chlorophylls is 10 Å, the distinctive spectral feature of PPC1 underscores the impact of pigment configuration on optical properties of the system. By using this platform, additional conditions can be screened by modulating the sequence of peptoid-porphyrin scaffolds or/and changing the AuNPs to incorporate specific SPR wavelengths. Similar to the

proteins in the antenna complex that possess the dual function of a supporting template and functional material, the peptoid decorated Au@SiO_2 also functions as a support for the porphyrin molecules and a generator of SPR. In conclusion, the newly developed platform can be a practical model for understanding the mechanisms of material design in natural antenna systems.

Reference

1. Croce, R. & van Amerongen, H. Natural strategies for photosynthetic light harvesting. *Nat. Chem. Biol.* **10**, 492-501 (2014).
2. Prathapan, S., Johnson, T.E. & Lindsey, J.S. Building-Block Synthesis of Porphyrin Light-Harvesting Arrays. *Journal of the American Chemical Society* **115**, 7519-7520 (1993).
3. Kim, Y., Lee, J.H., Ha, H., Im, S.W. & Nam, K.T. Material science lesson from the biological photosystem. *Nano Convergence* **3**, 19 (2016).
4. Otte, F.L. et al. Ordered Monolayers of Free-Standing Porphyrins on Gold. *Journal of the American Chemical Society* **136**, 11248-11251 (2014).
5. Grill, L. et al. Nano-architectures by covalent assembly of molecular building blocks. *Nat. Nanotechno.l* **2**, 687-691 (2007).
6. Roberts, D.A., Schmidt, T.W., Crossley, M.J. & Perrier, S. Tunable Self-Assembly of Triazole-Linked Porphyrin-Polymer Conjugates. *Chem-Eur. J.* **19**, 12759-12770 (2013).
7. Screen, T.E.O., Thorne, J.R.G., Denning, R.G., Bucknell, D.G. & Anderson, H.L. Amplified optical nonlinearity in a self-assembled double-strand conjugated porphyrin polymer ladder. *Journal of the American Chemical Society* **124**, 9712-9713 (2002).
8. Wang, Q.B. et al. Morphology and chirality controlled self-assembled nanostructures of porphyrin-pentapeptide conjugate: effect of the peptide secondary conformation. *J. Mater. Chem.* **21**, 8057-8065 (2011).
9. Dunetz, J.R. et al. Self-assembling porphyrin-modified peptides. *Org. Lett.*

7, 2559-2561 (2005).

10. Nguyen, T., Brewer, A. & Stulz, E. Duplex Stabilization and Energy Transfer in Zipper Porphyrin-DNA. *Angew Chem Int Edit* **48**, 1974-1977 (2009).
11. Fendt, L.-A., Bouamaied, I., Thöni, S., Amiot, N. & Stulz, E. DNA as Supramolecular Scaffold for Porphyrin Arrays on the Nanometer Scale. *Journal of the American Chemical Society* **129**, 15319-15329 (2007).
12. Simon, R.J. et al. Peptoids - a Modular Approach to Drug Discovery. *P Natl Acad. Sci. USA* **89**, 9367-9371 (1992).
13. Kang, B., Chung, S., Ahn, Y.D., Lee, J. & Seo, J. Porphyrin-Peptoid Conjugates: Face-to-Face Display of Porphyrins on Peptoid Helices. *Org. Lett.* **15**, 1670-1673 (2013).
14. Zuckermann, R.N., Kerr, J.M., Kent, S.B.H. & Moos, W.H. Efficient method for the preparation of peptoids [oligo(N-substituted glycines)] by submonomer solid-phase synthesis. *Journal of the American Chemical Society* **114**, 10646-10647 (1992).
15. Amunts, A., Drory, O. & Nelson, N. The structure of a plant photosystem I supercomplex at 3.4 angstrom resolution. *Nature* **447**, 58-63 (2007).
16. Wurthner, F., Kaiser, T.E. & Saha-Moller, C.R. J-Aggregates: From Serendipitous Discovery to Supramolecular Engineering of Functional Dye Materials. *Angew. Chem. Int. Edit.* **50**, 3376-3410 (2011).
17. Hartlen, K.D., Athanasopoulos, A.P.T. & Kitaev, V. Facile preparation of highly monodisperse small silica spheres (15 to > 200 nm) suitable for colloidal templating and formation of ordered arrays. *Langmuir* **24**, 1714-

1720 (2008).

18. Li, J.F. et al. Surface analysis using shell-isolated nanoparticle-enhanced Raman spectroscopy. *Nat. Protoc.* **8**, 52-65 (2013).

19. DuChene, J.S., Almeida, R.P. & Wei, W.D. Facile synthesis of anisotropic Au@SiO2 core-shell nanostructures. *Dalton Transactions* **41**, 7879-7882 (2012).

20. Liu, S.H. & Han, M.Y. Synthesis, functionalization, and bioconjugation of monodisperse, silica-coated gold nanoparticles: Robust bioprobes. *Adv Funct Mater* **15**, 961-967 (2005).

21. Gouterman, M. Spectra of Porphyrins. *J. Mol. Spectrosc.* **6**, 138-& (1961).

22. Li, C.C., Shuford, K.L., Chen, M.H., Lee, E.J. & Cho, S.O. A facile polyol route to uniform gold octahedra with tailorable size and their optical properties. *ACS Nano* **2**, 1760-1769 (2008).

23. Dulkeith, E. et al. Fluorescence quenching of dye molecules near gold nanoparticles: Radiative and nonradiative effects. *Phys Rev Lett* **89** (2002).

24. Schneider, G. et al. Distance-dependent fluorescence quenching on gold nanoparticles ensheathed with layer-by-layer assembled polyelectrolytes. *Nano Lett.* **6**, 530-536 (2006).

25. Abadeer, N.S., Brennan, M.R., Wilson, W.L. & Murphy, C.J. Distance and Plasmon Wavelength Dependent Fluorescence of Molecules Bound to Silica-Coated Gold Nanorods. *ACS Nano* **8**, 8392-8406 (2014).

26. Zhang, X.K. et al. Ag@zinc-tetraphenylporphyrin core-shell nanostructures with unusual thickness-tunable fluorescence. *Chem. Commun.* **49**, 3513-3515 (2013).

27. Feng, A.L. et al. Distance-Dependent Plasmon-Enhanced Fluorescence of Upconversion Nanoparticles using Polyelectrolyte Multilayers as Tunable Spacers. *Sci Rep-Uk* **5** (2015).

28. Khatua, S. et al. Resonant Plasmonic Enhancement of Single-Molecule Fluorescence by Individual Gold Nanorods. *ACS Nano* **8**, 4440-4449 (2014).

29. Ming, T., Chen, H.J., Jiang, R.B., Li, Q. & Wang, J.F. Plasmon-Controlled Fluorescence: Beyond the Intensity Enhancement. *J. Phys. Chem. Lett.* **3**, 191-202 (2012).

30. Geddes, C.D. & Lakowicz, J.R. Metal-enhanced fluorescence. *J. Fluoresc.* **12**, 121-129 (2002).

31. Kern, A.M. et al. Enhanced single-molecule spectroscopy in highly confined optical fields: from [small lambda]/2-Fabry-Perot resonators to plasmonic nano-antennas. *Chem. Soc. Rev.* **43**, 1263-1286 (2014).

32. Lakowicz, J.R. et al. Plasmon-controlled fluorescence: a new paradigm in fluorescence spectroscopy. *Analyst* **133**, 1308-1346 (2008).

33. Anger, P., Bharadwaj, P. & Novotny, L. Enhancement and quenching of single-molecule fluorescence. *Phys. Rev. Lett.* **96** (2006).

34. Kuhn, S., Hakanson, U., Rogobete, L. & Sandoghdar, V. Enhancement of single-molecule fluorescence using a gold nanoparticle as an optical nanoantenna. *Phys. Rev. Lett.* **97** (2006).

35. Zhao, L., Ming, T., Shao, L., Chen, H.J. & Wang, J.F. Plasmon-Controlled Forster Resonance Energy Transfer. *J. Phys. Chem. C* **116**, 8287-8296 (2012).

36. Lunz, M. et al. Surface Plasmon Enhanced Energy Transfer between Donor and Acceptor CdTe Nanocrystal Quantum Dot Monolayers. *Nano Lett.* **11**, 3341-3345 (2011).

37. Dexter, D.L. A Theory of Sensitized Luminescence in Solids. *J. Chem. Phys.* **21**, 836-850 (1953).

38. Forster, T. *Zwischenmolekulare Energiewanderung Und Fluoreszenz. *Ann. Phys-Berlin* **2**, 55-75 (1948).

39. Qin, X.C., Suga, M., Kuang, T.Y. & Shen, J.R. Structural basis for energy transfer pathways in the plant PSI-LHCI supercomplex. *Science* **348**, 989-995 (2015).

40. Suga, M., Qin, X., Kuang, T. & Shen, J.-R. Structure and energy transfer pathways of the plant photosystem I-LHCI supercomplex. *Current Opinion in Structural Biology* **39**, 46-53 (2016).

Chapter 4. Hybrid Z-scheme of photosystem I and $BiVO_4$ for hydrogen evolution

4.1 Introduction

In this chapter, Z-scheme of light reaction was chosen as a model system for the development of hybrid Z-scheme for hydrogen production. In the developed system, hydrogen was successfully produced from water under visible light without any chemical nor electrical reducing power, as nature effectively produces NADPH from water under sunlight.

In natural photosynthesis, the two-step photo-induced charge separation in photosystem II (PSII) and photosystem I (PSI) and an electron chain between the two photosystems follows a Z-scheme. First, a hole is generated from the charge separation step in the PSII that oxidizes two water molecules into an oxygen and four protons, and the excited electron moves to the PSI through the electron transport chain. The electron is finally excited in the PSI and gains sufficient potential energy (-0.58 V vs. NHE, pH 7) to reduce $NADP^+$.[1, 2] The step-wise charge transfer reaction provides the efficient light-to-chemical energy conversion from only water and visible light (Scheme 1a). Generally, approximately 28.2% of the total sunlight is converted into chemical energy as ATP and NADPH in the light reaction of natural photosynthesis.[3] The simplified structural model and energy diagram of natural Z-scheme is presented in **Figure 4.1** (up).

This natural Z-scheme has inspired an artificial Z-scheme, which has been

used in photocatalytic fuel production. In recent years, hydrogen fuel production from non-sacrificial water splitting has been studied by combining half-reactions that produce H_2 and O_2. In 1979, Bard introduced photosynthesis as a model system for water splitting using dual semiconductors.[4] This novel approach enabled H_2 production from water using only visible light. Numerous studies on material development and system design have since been conducted to exploit solar light to the greatest extent possible. Generally, metal oxides[5-7] metal (oxy)nitrides[8, 9] and metal sulfides[10] have been utilized as charge separating photocatalysts, and proper co-catalysts have been loaded to catalyze H_2 and O_2 production.[11] For H_2 evolving part, Pt,[8] Ru,[5, 12] and Ni-based[10] co-catalysts have been studied to enhance the photocatalytic activity. To obtain an optimal band position, some photocatalysts were further engineered with dopants[13] or treated to form solid solutions.[14, 15]

Another interesting approach to modeling natural photosynthesis is a direct utilization of photosystems for a H_2-evolving photocatalyst. The PSI is a naturally existing photocatalyst that possesses solar light-active chlorophyll dyes that have an optimal structure for efficient energy transfer. The P700 reaction center at the center of the PSI has a charge separation efficiency near unity and a low excitation energy of 1.77 eV (l = 700 nm).[1, 2] Therefore, the PSI itself is very attractive photocatalyst that can be used in natural environments. Recently, PSI hybrid systems have been fabricated by conjugating artificial or biological co-catalysts. Generally, the PSI has been platinized to deposit platinum nanoclusters on the electron emitting stromal side of a protein by the photo-reductive deposition reaction, $[PtCl_6]^{2-} + 4e^- + h\nu \rightarrow Pt + 6Cl^-$.[16-18] Similarly, a co-catalyst has been conjugated using a chemical linker. Recently, Pt or Au nanoparticles[19, 20] and

hydrogenases[21-25] have been covalently linked to the PSI to dramatically enhance its H_2 evolution activity. However, to position a chemical linker at the desired position, the PSI was reconstituted mostly by engineering cysteine (Cys) residues for use in dithiol molecular wire. The most recent studies have reported the self-assembly of molecular catalysts, such as a Ni catalyst[26] and cobaloxime[27]. However, all of these systems only mimic the one-step photo-reduction in the PSI, which requires that a chemical donor, such as ascorbic acid, be mixed into the reaction solution. In this study, we implemented a full Z-scheme for the H_2 evolution from water using platinized PSI (PtPSI). This is the first report of the use of a protein-photocatalyst system for H_2 production from water without the use of an additional reducing additive, which we call a "hybrid Z-scheme". The synthesized semiconductor particle both participated in the oxidation of the photocatalyst and served as an electron supply for the PSI.

Two types of structural design are generally used in a Z-scheme, depending on the mediating role between the two reaction centers. First, when the electron mediator is a redox couple in the form of ion pairs, the two reaction centers are physically separated. However, the redox pair can induce an undesirable back reaction and dissipate the electrons and holes that participate in the intended pathway. Moreover, it is often difficult to operate a redox couple mediated system over a wide pH range.[28] In the second design, a conducting material can be employed as a mediator to transfer electrons directly between the reaction centers. The two reaction centers are thus physically linked via a conductor to form an "all-solid-state". The integration of two reaction centers with a conductor between the centers creates an ohmic contact and reduces the distance for electron transfer.

Thus, the back reaction is prevented, and the working conditions are expanded to a wide pH range and even to the gas-phase.[28] Recently, a reduced graphene oxide was used as a solid electron mediator for all-solid-state water splitting using $BiVO_4$ and $Ru/SrTiO_3$:Rh photocatalysts,[12] and innovative developments in H_2-evolution systems have been realized by designing various all-solid-state Z-schemes using conducting mediators.[13, 29-31] Our hybrid Z-scheme was also constructed in an all-solid state by attaching metal particles onto a semiconductor to form a chemical linker between the metal and the PSI. The metal-deposited semiconductor served both as a stable support and a direct electron supplier for the PSI. In a natural thylakoid membrane, photosynthetic proteins are stably inserted into the lipid membrane, resulting in a fluid structure where the proteins are arranged in a fixed position and orientation. Immobilizing a PSI on the metal should be analogous to inserting a PSI in the thylakoid membrane. In this study, we compared a linked system and an unlinked but mixed system and analyzed the positive effects of the all-linked system.[12]

In the designed system, $BiVO_4$ was selected as the semiconductor component. $BiVO_4$ has both a suitable valence band for water oxidation (2.75 V vs. NHE) and a low band gap for visible light absorption (2.43 eV).[32] Gold (Au) or silver (Ag) nanoparticles were deposited on the surface. The work functions of these nanoparticles (-5.1 eV for Au and -4.7 eV for Ag)[33] are both located between the conduction band of $BiVO_4$ and the redox potential of the PSI reaction center (P700, 0.47 V vs. NHE, pH 8)[34], such that these nanoparticles can serve as a conducting mediator between two components. **Figure 4.1** (down) presents the structural model and the energy diagram of the hybrid Z-scheme with an Au

mediator. In terms of its light absorption properties, the PSI harvests solar light through chlorophylls that efficiently absorb red (≃700 nm) and blue (≃450 nm) light, and $BiVO_4$ absorbs light with wavelengths below 510 nm. Therefore, the absorption range in the hybrid Z-scheme encompasses the entire visible light range. Metal particles were carboxyl-functionalized for covalently conjugation with the PtPSI via EDC/Sulfo-NHS coupling. The metal-deposited $BiVO_4$ (mt-$BiVO_4$) and the PtPSI constituted a hybrid Z-scheme in an all-solid-state form, which successfully evolved H_2 from water under visible light.

Natural Z-scheme

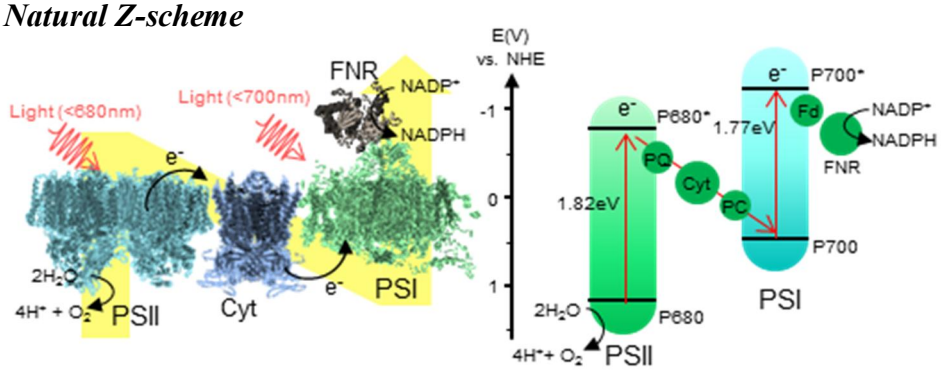

Hybrid Z-scheme of PSI and semiconductor ($BiVO_4$)

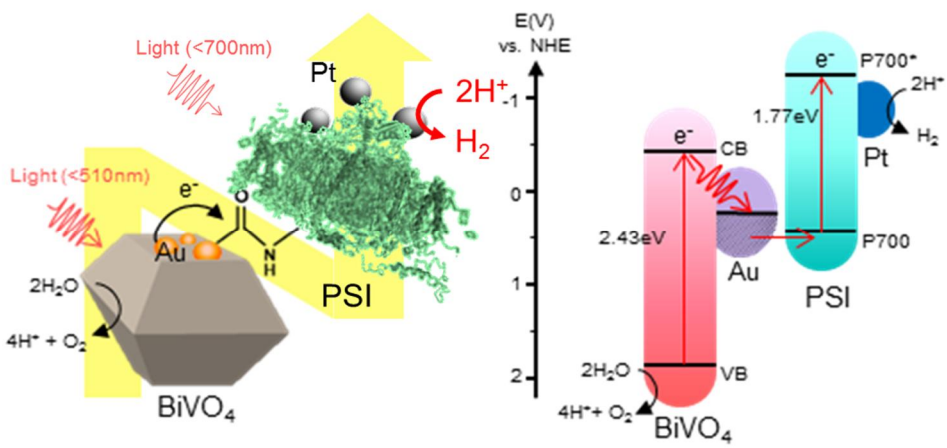

Figure 4.1. Natural Z-scheme (up) and Hybrid Z-scheme developed in this study (down).

4.2 Experimental and analysis

4.2.1 Materials

Sodium ascorbate (Asc, 98%), 2,6-dichloroindophenolate hydrate (Dc, 90%), sodium hexachloroplatinate(IV) hexahydrate ($Na_2[PtCl_6]$, 98%), gold(III) chloride trihydrate ($HAuCl_4 \cdot 3H_2O$, 99.9%), silver nitrate ($AgNO_3$, 99.0%) and 3-mercaptopropionic acid (MPA, 99%) were purchased from Sigma-Aldrich, and 1-ethyl-3-(3-dimethylaminopropyl)carbodiimide (EDC, 98%) and N-hydroxysulfosuccinimide (sulfo-NHS, 98%) were purchased from Tokyo Chemical Industry. High purity deionized water (18.2 MW cm^{-1}) was used in all of the procedures.

4.2.2 Isolation of PSI

The PSI protein was isolated by the established method with minor modifications.[35] Spinach (*Spinacia oleracea* L.) was purchased from a local market. Two hundred grams of green spinach leaves were ground using a blender with 600 ml of washing buffer (0.3 M sucrose, 30 mM Tris-HCl, 15 mM NaCl, pH 7.8) for 30 s. The obtained homogenate was filtered through 2 layers of Miracloth (with a pore size of 22-25 mm, CalBiochem) and centrifuged at 2,000 g for 7 min. The light green supernatant was discarded, and the pallet was resuspended in a hypotonic buffer (5 mM EDTA, 5 mM Tris-HCl, pH 7.8). The solution was sonicated for 2 min and centrifuged at 10,000 g for 15 min. The pallet was adjusted

to 2.5 mgChl ml^{-1} using a basic buffer (0.3 M sucrose, 30 mM Tris-HCl, pH 7.8) and 1.7% triton X-100 (w/v) was added. After gentle stirring for 30 min in the dark at 4 °C, the solution was centrifuged at 35,000 g for 30 min, and the supernatant was collected. The solution was adjusted to 2.0 mgChl ml^{-1} using a basic buffer, and dodecyl-b-D-maltoside (DDM) was added to produce a final concentration of 2.0% (w/v). After gentle stirring for 20 min in the dark at 4 °C, 9 ml of the solution was loaded onto a 24 ml 0.1-1.0 M sucrose gradient (containing the basic buffer and 0.05% DDM) with a 5 ml cushion of 2 M sucrose. After ultracentrifugation at 26,800 rpm for 17 h in a SW-32 rotor (Beckman), the lowest dark green band was collected with a syringe and frozen at -80 °C using 20% glycerol (v/v).

4.2.3 Characterization of PSI

The protein concentration was adjusted via the chlorophyll concentration. The chlorophyll concentration was determined after extraction in 80% acetone using a method that was developed by Arnon.[36] The proteins were analyzed using SDS-PAGE and a Coomassie blue staining step. The SDS-PAGE was carried out using 15% acrylamide resolving gels. Briefly, 10 μl of the samples and pre-stained protein size markers were loaded onto each well, and electrophoresis was performed at 100 V for 100 min. After the electrophoresis step, the gel was washed in distilled water for 10 min and rinsed with a fixation solution (containing 30% methanol and 10% acetic acid) for 30 min. After fixation, EzWayTM Protein-Quick Blue solution (Koma Biotech) was added and stained for 2 h.

4.2.4 Platinization of PSI

The extracted PSI was dialyzed in a 20 mM sodium phosphate buffer with a pH of 7.2 (reaction buffer) for 24 h before platinization. The PtPSI was prepared by photo-deposition using 30 mM Asc and 0.2 mM Dc as a sacrificial electron donor. The reaction proceeded in the reaction buffer with 0.05 mgChl ml^{-1} PSI, 0.4 mM $Na_2[PtCl_6]$ and an Asc/Dc couple (for a total volume of 10 ml). A continuous white light emitting diode (LED) bulb light illuminated the sample under vigorous stirring for 20 h. The PtPSI was washed with the reaction buffer before linking with the oxidation component to remove the remaining $Na_2[PtCl_6]$ and Asc/Dc.

4.2.5 Synthesis of $BiVO_4$

The hydrothermal method was used as previously reported.[37] Typically, 36.0 mmol of NH_4VO_3 (99%) and 36.0 mmol of $Bi(NO_3)_3 \cdot 5H_2O$ (98%) were dissolved in 220 and 80 ml of 2.0 M nitric acid solutions, respectively. The two solutions were mixed, and a yellow homogeneous solution was formed under stirring. The pH value of the solution was then adjusted to 2.0 using an ammonia solution under vigorous stirring until an orange precipitate was obtained. After further stirring for 0.5 h, the precipitate was aged for 2 h, and 70 ml of the subsided precipitate was transferred to a Teflon-lined stainless steel autoclave (100 ml) and hydrothermally heated to 473 K, which was held for 24 h. The resulting yellow powder was filtered following natural cooling to room temperature and dried in air at 60 °C.

4.2.6 Photo-deposition of metal on $BiVO_4$

The metals (Au and Ag) were photo-deposited onto the as-synthesized $BiVO_4$. $HAuCl_4$ and $AgNO_3$ were used as precursors for the Au and Ag deposition. Generally, 0.2 g of the as-synthesized $BiVO_4$ and 10 wt% of the metal precursor (by calculation) were stirred together in 100 ml of deionized water under irradiation by a 300-W Xe lamp (420-nm cut) for 3 h. The metal-deposited $BiVO_4$ (mt-$BiVO_4$) was washed with deionized water 3 times to remove the unreacted metal precursor before further chemical treatment and SEM analysis.

4.2.7 EDC/Sulfo-NHS coupling

Finally, covalent linking between PtPSI and mt-$BiVO_4$ was carried out via EDC/sulfo-NHS coupling. First, 0.1 g of mt-BiVO4 was immersed in ethanolic 10 mM MPA to carboxylate the metal particles. After gently stirring the solution for 24 h, the MPA treated mt-$BiVO_4$ was rinsed with deionized water and finally diluted in 5 ml of 10 mM MES buffer (pH 5.5). Then, 30 mg of EDC and 30 mg of sulfo-NHS were added, stirred for 2 h and washed with the reaction buffer. Finally, l ml of 0.5 mgChl ml^{-1} of the prepared PtPSI was added to the total solution volume and gently stirred for 24 h. The all-linked samples were washed twice with the reaction buffer to remove unlinked proteins. For reference, we added 1 ml of 0.5 mgChl ml^{-1} of the PtPSI to 0.1 g of the carboxylated mt-$BiVO_4$ and stirred the resulting mixture for 24 h.

4.2.8 Analytical methods

The irradiance of the light source was measured using a spectrum analyzer (International Light Technologies, ILT950). The UV/Visible absorption spectra were measured using a NanoDropTM 2000c and a spectroscopic cuvette. The samples were dispersed in the reaction buffer, which was then place in a 1-ml cuvette for analysis. The UV/Visible reflectance spectra were obtained using a UV-Vis-NIR spectrometer (Agilent Technologies, Cary 5000).

The FESEM micrographs were obtained using a Zeiss, SUPRA 55VP operating at 2 kV. The FESEM samples were prepared by dropping the sample containing solutions onto silicon wafers and drying in air.

The phase composition of the synthesized powder was determined using X-ray powder diffraction (XRD, Bruker, AXS D8 Advance) with CuKα radiation. The XRD patterns were recorded in a 2θ range of 10°-60°. The step size and the counting time were 0.02° and 0.25 s, respectively. The XRD patterns were analyzed using an EVA software package (Bruker AXS) to identify the phases present.

The PL spectra were taken using a PTI QuantaMasterTM spectrofluorometer, QM4 (Photon Technology International, Birmingham, NJ) with an excitation wavelength of 340 nm, a scan range of 450-660 nm and a step size of 1 nm. Each sample was placed in a cuvette and stirred vigorously to disperse the particles. Typically, 1 mg of sample was put into 3 ml of the reaction buffer. When

the mt-$BiVO_4$ was mixed or linked with PtPSI, the additional washing step for the removal of the unlinked protein was skipped.

The quantitative detection of hydrogen was performed by gas chromatography (GC, PerkinElmer, NARL8502 Model 4003). Typically, 0.05 g of the PtPSI-mt-$BiVO_4$ in 20 ml of the reaction buffer was placed in a tightly capped vial and stirred vigorously during the photo-reaction. One milliliter of the final gas was ejected into the gas chromatograph by a syringe at the designated time. The GC measured the molar proportion of the hydrogen gas relative to the total ejected gas, and the exact amount of gas was calculated by multiplying by the empty space in the vial reactor.

4.3 Results and discussion

4.3.1 Synthesis of Pt-PSI

PSI was extracted from spinach and characterized by SDS-PAGE. The isolated thylakoid membrane fragments were distributed into three layers via a sucrose density gradient (**Figure 4.2 (a)**). The thick upper layer consisted of a light harvesting complex II (LHCII) and other protein fragments, and the middle and lower layers consisted of monomeric and aggregated PSI, respectively. Each protein layer was injected using a syringe and analyzed by SDS-PAGE (**Figure 4.2 (b)**). The PSI was identified by a significant band that was assigned to PsaA and PsaB polypeptides and other minor polypeptide bands that are not marked in the figure.[35] Two bands also appeared that corresponded to the light harvesting complex I (LHCI). In a plant thylakoid, the LHCI surrounds a PSI core to collect light and transfer the photo-energy to the PSI core. Previous studies on bacterial photosynthetic proteins have demonstrated that a light harvesting antenna-reaction center core complex exhibits higher photo-activity than a bare reaction center core *in vitro*.[38] Thus, we expected the LHCI to serve as an extra light collector in our LHCI-PSI complex and used as this form for the remaining procedures. The polypeptides from the PSI bands virtually disappeared in the LHCII-rich band, which showed that the PSI was well-isolated from the thylakoid membrane.

The H_2 evolution efficiency of the platinized PSI was measured by gas chromatography before the PtPSI was linked to the $BiVO_4$-metal complex. During the 20 h of the photo-reduction process, ≃1 mmol H_2 $mgChl^{-1}$ of H_2 was generated.

Detectable H_2 (< ≃0.01 mmol H_2 $mgChl^{-1}$) was produced after 6 h, which corresponded to the platinization stage of the PSI. After the initial platinization stage, the H_2 production rate increased dramatically. The maximum activity was reasonable compared to previous reports for platinized PSI systems, as shown in **Table 4.1**. Typically, PSI extracted from thermophilic bacteria exhibits higher photo-activity and stability. However, we used spinach as a source material to simplify the extraction method and mass produce the final protein.

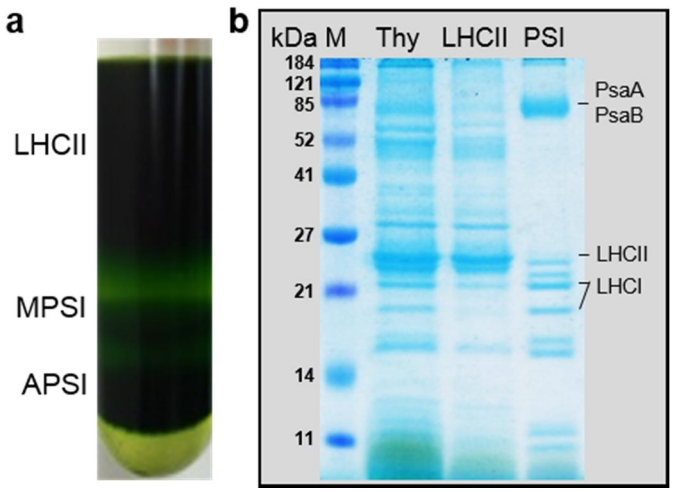

Figure 4.2 (a) Sucrose density gradient resulting in three separate layers: LHCII-rich thylakoid, monomer PSI (MPSI) and aggregated PSI (APSI); (b) SDS-PAGE of thylakoid before ultracentrifugation (Thy), LHCII-rich thylakoid fragment (LHCII, upper layer in (a)), and PSI (PSI, middle and bottom layer in (a)). Identified main bands are marked with the name of component.

Table 4.1. H_2 evolution activity in PtPSI. The extracted PSIs are all wild type and are not rebuilt.

Year	Source of PSI	Electron donor, mediator	Maximum activity ($mmol\ H_2\ h^{-1}\ mgChl^{-1}$)	Light source
This study	Spinach	Asc, Dc	0.08	White LED
(2001)[17]	Spinach	Asc, PC	2	LED (660 nm)
(2004)[18]	Spinach	Asc, Corss-linked PC	0.09 (0.03 without PC)	150-W halogen lamp (< 600 nm)
(2010)[16]	Thermophilic bacteria	Asc, Cyt c6	5.5	150-W halogen lamp (< 590 nm)

4.3.2 Synthesis of metal deposited $BiVO_4$

To selectively extract electrons, single crystal monoclinic $BiVO_4$ was synthesized by a hydrothermal method. The synthesized particles were then characterized by XRD (**Figure 4.3**) and FESEM (**Figure 4.4**). The XRD pattern was well-matched with that of monoclinic $BiVO_4$, which corresponds to the standard card #14-0688. The decahedral shape and fine crystallinity of $BiVO_4$ was observed in the FESEM images. The two square exposed facets corresponded to the {010} facet, which was the electron-accumulated facet, and the isosceles trapezoidal facets at the other sides corresponded to the {110} facet, which was the hole-accumulated facet.[39] Thus, the Au and Ag particles were selectively deposited on the {010} facet of $BiVO_4$ by accepting electrons on the surface.

The photo-deposition of Au and Ag was carried out using $HAuCl_4$ and $AgNO_3$ metal precursors in water, respectively, which functioned as hole scavengers. A large number of small-sized metal particles can be used to extend the contact surface between the materials and reduce the electron migration distance. In the experimental process, the initial precursor concentration was optimized to 10 wt%, because a further increase in the precursor did not significantly improve the deposited area. The number of deposited particles saturated in ≃3 h, and further reaction only enlarged the particle size.

The mt-$BiVO_4$ particles that were synthesized by the optimized procedure were observed using FESEM (**Figure 4.5**). The diameters of both the Au and Ag particles were distributed between 100 and 200 nm, which was approximately 7-fold larger than the size of the monomeric PSI. We integrated the area of the

exposed {010} facet and the metal-deposited partial area using the FESEM images. The resulting average ratio of the area of the metal-deposited surface to that of the {010} facet was approximately 11% for Au-$BiVO_4$ and 30% for Ag-$BiVO_4$. Assuming that the area of {010} facet of a $BiVO_4$ particle was 10 mm^2 and that PSI was densely bound to the flat metal surface as monolayer, 6,400 (for the Au-deposited particles) and 17,000 (for the Ag-deposited particles) monomeric PSI should have been conjugated to a single $BiVO_4$ particle. Conversion to the macroscopic scale showed that 0.016 mgChl (for the Au-deposited particles) and 0.043 mgChl (for the Ag-deposited particles) of PSI were the equivalent binding amounts for 1 g of $BiVO_4$.

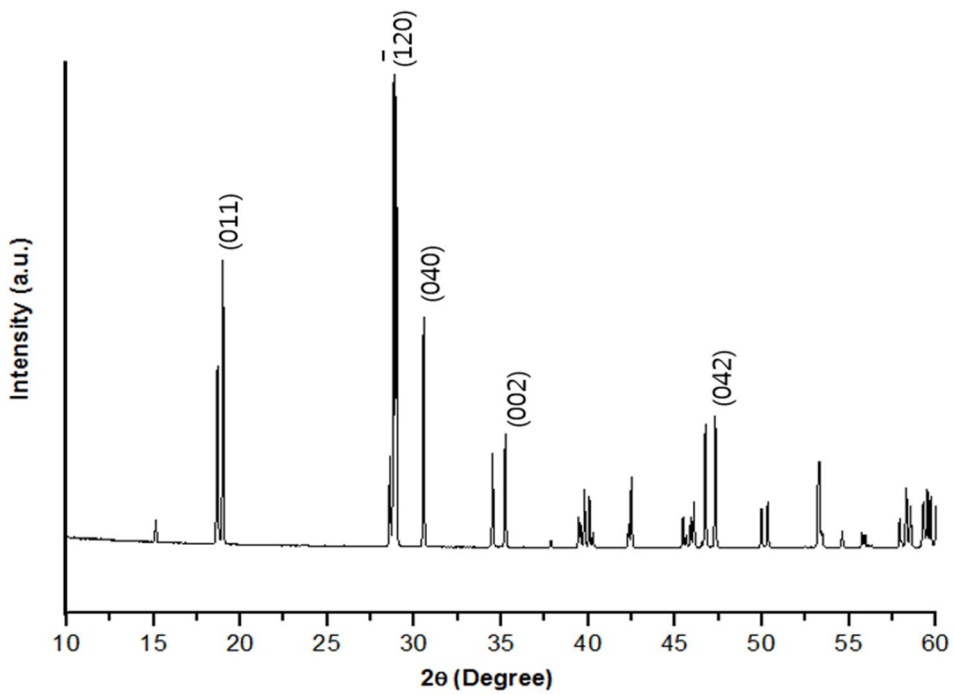

Figure 4.3. XRD pattern of monoclinic $BiVO_4$ (JCPD #14-0688).

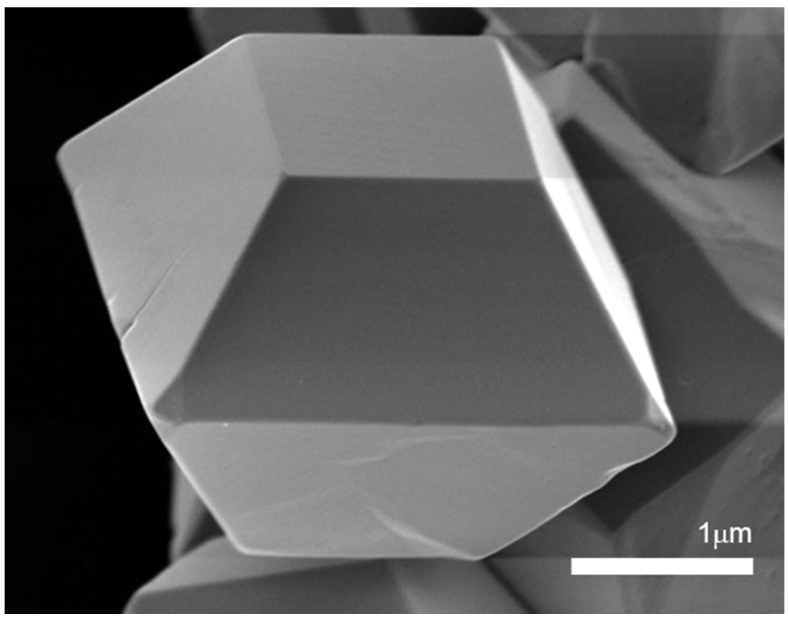

Figure 4.4. FESEM image of $BiVO_4$. Scale bar: 4 μm.

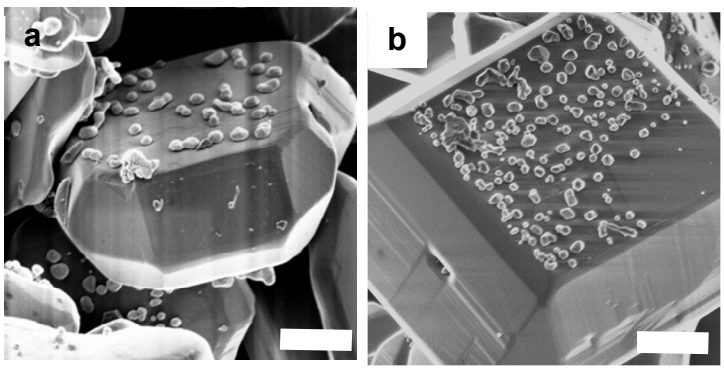

Figure 4.5. FESEM image of (a) Au-$BiVO_4$ and (b) Ag-$BiVO_4$. Scale bar: 1 μm.

4.3.3 Optical property analysis

The optical properties of the two photocatalysts were investigated by UV/Visible absorption. The absorption spectra were recorded for isolated PSI (which is shown as a green solid line in **Figure 4.6**), which exhibited two primary peaks at 436 nm and 678 nm. The minor peak at 471 nm that was observed in the spectra corresponded to the light harvesting complex I (LHCI) that surrounded the PSI core.[35] The diffuse reflectance of $BiVO_4$ was measured, and the spectra is presented as a blue dotted line in figure 3. Our $BiVO_4$ absorbed light effectively below 510 nm.

In this study, we used a white LED bulb, which is a commonly used indoor light, as a light source to provide the full spectrum of visible light with an intensity near the light saturation point of the PSI (190 mE m^{-2} s^{-1} with a 660-nm LED).[17] Our light source had an intensity of 186 mE m^{-2} s^{-1} between 650 nm and 700 nm and of 91 mE m^{-2} s^{-1} below 510 nm. The mild intensity of the light source prevented a temperature rise in the reactor and unnecessary energy dissipation. Figure 3 shows the irradiance intensity spectra for different wavelengths, which are fitted with a black line.

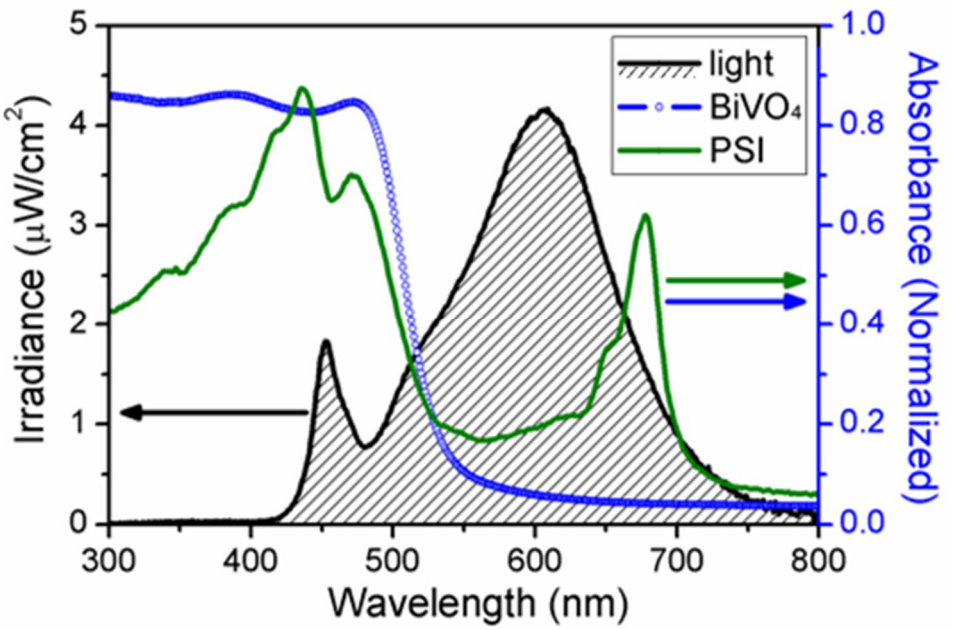

Figure 4.6. Absorption spectra of PSI (green line) and $BiVO_4$ (line with blue circle) and irradiance spectra of LED light used in this study (black line).

4.3.4 Synthesis of hybrid Z-scheme

The as-prepared PtPSI and mt-$BiVO_4$ was integrated into the hybrid system. To carboxylate the metal surface, the synthesized mt-$BiVO_4$ was treated with an MPA ethanolic solution. An amide bond was then formed between the carboxyl group on the metal and the amine group on the PSI by EDC/Sulfo-NHS coupling. Generally, the primary amine in the lysine (Lys) residue has the highest activity; thus, most of the amide bond was expected to be formed on the Lys of the protein surface. The Lys was densely located on both the lumen and stromal side of the PSI, which are shown as magenta spheres in **Figure 4.7**. In platinization, the reduction of Pt occurred primarily at the stromal side of the electron emitting site, such that the Pt nanoclusters were expected to cover the electron emitting site of the PSI (which is shown as orange spheres in **Figure 4.7**). Therefore, some of the exposed active residues in stromal side may have been blocked. However, the active residues on the lumen side were exposed without obstruction and could freely form an amide bond. The amide bond at the lumen side provided a favorable pathway for the acceptance of electrons from mt-$BiVO_4$.

As mt-$BiVO_4$ is a micro-particle, it sinks into a solution within a few minutes (see Au-B and Ag-B in **Figure 4.8**). However, after coupling to the PtPSI, some of the particles were still dispersed in solution after 1-h holding time (see Au-B-PtPSI and Ag-B-PtPSI in **Figure 4.8**). The upper greenish section contained both unlinked PtPSI and all-linked particles. The absorption spectra of the upper dispersed particles were removed for the absorption measurements. In **Figure 4.8 (a)**, the broad absorption spectra over the entire wavelength range corresponded to the $BiVO_4$ particles that were dispersed in solution, and the observable peaks at the

wavelengths of red and blue light corresponded to the PtPSI. To calculate the amount of the linked PtPSI, the micro-particles were removed by gentle centrifugation, and the concentration of the remaining PtPSI particles was measured from the absorbance spectra. Thus, 0.08 ± 0.03 mgChl and 0.16 ± 0.05 mgChl of the PtPSI decreased in the solution after coupling with 1 g of Au-$BiVO_4$ and Ag-$BiVO_4$, respectively. The differing amounts that were bound on Au and Ag resulted primarily from the different deposited areas of the metal particles.

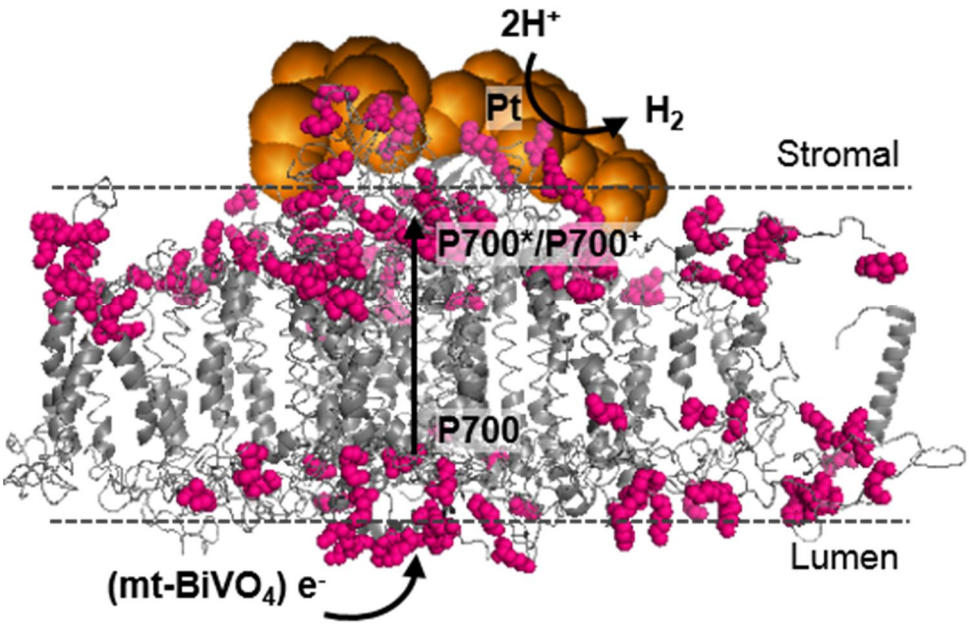

Figure 4.7. Molecular structure of PtPSI showing emphasized Lys, which are the primary targets in EDC/sulfo-NHS coupling. Pt nanoclusters and Lys are shown as orange and magenta spheres. The electron pathway from lumen side to stromal side is shown with arrows (PDB entry 2WSC).

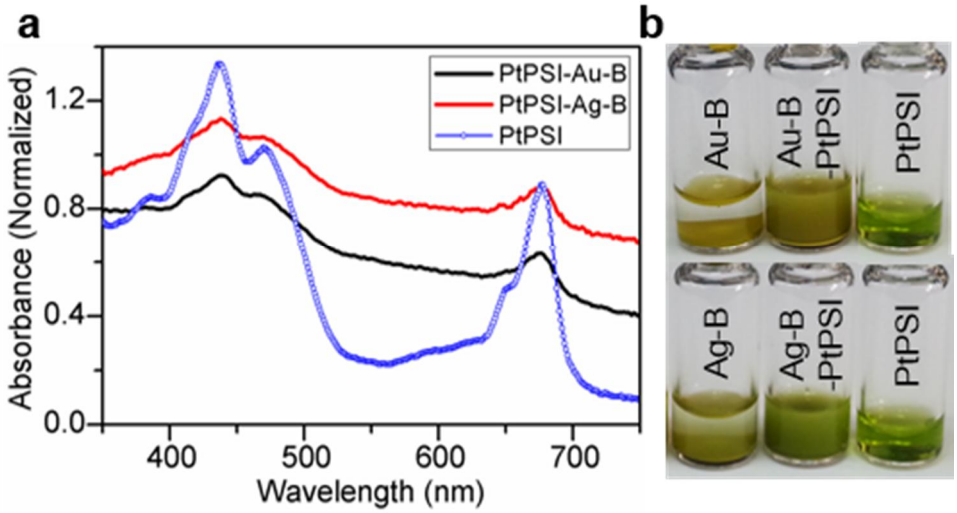

Figure 4.8. (a) Absorption spectra of PtPSI (line with blue circle), dispersed PtPSI linked with Au-$BiVO_4$ (red) and Ag-$BiVO_4$ (black); (b) image of synthesized samples after 1-h holding time at room temperature. B denotes $BiVO_4$.

4.3.5 Electron transfer study in the hybrid system by PL analysis

We evaluated the electron motion in the hybrid system by PL analysis (**Figure 4.9**). The PL spectra were observed for 4 different samples, $BiVO_4$, mt-$BiVO_4$, mt-$BiVO_4$ with PtPSI, which was simply mixed together (Mixed) and covalently all-linked by EDC coupling (Linked). In monoclinic $BiVO_4$, UV excitation generates holes in the O_{2p} band, and the electrons in the V_{3d} band and the excitation energy can be relaxed by recombination at Bi_{6s}.[40] Our $BiVO_4$ exhibited a PL peak at approximately 540 nm in agreement with previous reports.[41] We first observed the PL quenching effect by metal deposition. The metal particle covering the electron emitting facet can accept electrons from the V_{3d} conduction band of $BiVO_4$ and decreases recombination. The PL intensity at 540 nm for Au-$BiVO_4$ and Ag-$BiVO_4$ was 93% and 62% of that of pure $BiVO_4$. This result suggests that Ag offers an advantage over Au in electron extraction. Structurally, the deposited area of Ag is approximately 3-fold that of Au, which can result in more effective quenching. Besides, plasmonic metal can increase or decrease PL in various ways including local electric field enhancement, radiative/non-radiative decay enhancement, and energy quenching inducement. The PL quenching observed in this study may be the result of these coupled effects. In our system, transfer of excited electron to metal and plasmon driven PL enhancement occurred simultaneously.

To observe additional electron transfer to the protein, the mt-$BiVO_4$ was combined with the PtPSI. The use of the protein resulted in electron transfer from the metal toP700 and induced extra quenching. In the analysis, 0.5 mgChl of the PtPSI was mixed with and linked to 1 mg of the mt-$BiVO_4$. In both the Au-$BiVO_4$

and Ag-$BiVO_4$, the PL of the covalently linked system was quenched more than that of the simply mixed system. This result supported the hypothesis that chemical bonding between metal and protein facilitated efficient electron transfer from the $BiVO_4$ conduction band to the PSI. The amount of the PtPSI was then reduced to 0.05 mgChl, which was comparable to the theoretical equivalent binding amount of the PSI on Ag-$BiVO_4$. Herein, the linked system exhibited noticeable quenching, whereas there was nearly negligible quenching in the mixed system. Thus, the quenching effect resulted primarily from only the linked PtPSI. Interestingly, the PL quenching in the linked system with 0.05 mgChl PtPSI was comparable to that in the mixed system with 0.5 mgChl of the PtPSI.

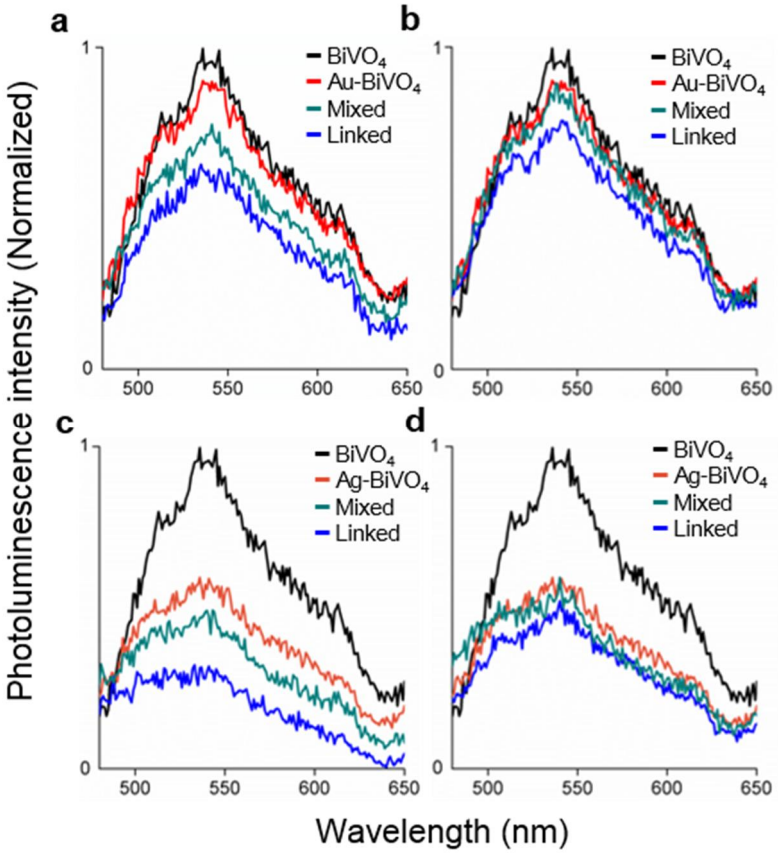

Figure 4.9. (a) PL spectra of Au-$BiVO_4$ with 10 equivalent PtPSI; (b) PL spectra of Au-$BiVO_4$ with one equivalent PtPSI; (c) PL spectra of Ag-$BiVO_4$ with 10 equivalent PtPSI; (d) PL spectra of Au-$BiVO_4$ with one equivalent PtPSI.

4.3.6 H_2 evolution measurement by GC analysis

The H_2 evolution rate was measured by GC. The hybrid Z-scheme using Au and Ag mediators exhibited an H_2 evolution activity of 34 nmol h^{-1} and 15 nmol h^{-1}, respectively (**Figure 4.10**). To our knowledge, this result is the first observation of H_2 evolution from a protein-photocatalyst system in which only water was used as an electron source. The calculated external quantum efficiency of the system was approximately 10^{-5}. Such a low quantum efficiency resulted primarily from the inefficient hybrid ratio of the reduction component of the PtPSI to the oxidation component, $BiVO_4$. The oxygen evolution activity of monoclinic $BiVO_4$ with a $NaIO_3$ sacrificial agent has been previously reported to be approximately 100 mmol h^{-1} g^{-1}.[37] Considering that 4 electrons from the oxidation step immediately move to PSI via the metal mediator in the Z-scheme, 400 mmol h^{-1} of electrons can be supplied to the PSI from 1 g of $BiVO_4$. However, considering that the maximum amount of the PtPSI was conjugated on $BiVO_4$, the activity of the photo-reduction from the equivalently bound protein lagged far behind (at approximately 1/160,000 (for Au-deposited particles) and 1/58,000 (for Ag-deposited particles)) the photo-oxidation in the semiconductor component of the hybrid system. The imbalance between the oxidation and reduction rates was the primary limitation of the hybrid system in terms of the efficiency. To overcome the imbalance in the combination ratio, nano-scale semiconductor particles should be used to increase the surface area for protein binding. The photoreaction proceeded for 72 h, and H_2 was collected every 24 h. **Figure 4.11** shows the measured amount of H_2 from our Z-scheme using Au and Ag mediators. The initial H_2 evolution activity lasted steadily for 72 h and even slightly increased in some cases. In this regard, we expect that

the unlinked, but attached PSIs in the vicinity of activated metal formed new amide bonds during the photo-reaction, followed by providing additional linked Z-scheme.

When the PtPSI and mt-$BiVO_4$ components were mixed without covalent conjugation to serve as a reference, the H_2 evolution activity was lowered to approximately 1 nmol h^{-1}. In order to clarify the pathway of H_2 evolution, several mt-$BiVO_4$ samples also have been investigated by GC analysis. As a result, all the contrast samples including Au-$BiVO_4$, Ag-$BiVO_4$, Pt-$BiVO_4$ and pure $BiVO_4$ showed no H_2 evolution activity when the deposited metal was either activated with EDC/Sulfo-NHS or inactivated.

When the H_2 evolution activity was recalculated considering the bound PtPSI, 0.42 ± 0.20 mmol h^{-1} $mgChl^{-1}$ and 0.091 ± 0.044 mmol h^{-1} $mgChl^{-1}$ of H_2 were produced in the Au- and Ag-mediated systems. The activity was much higher (for the Au-deposited particles) or analogous (for the Ag-deposited particles) to the activity that was measured during the platinization step using an Asc/Dc electron donor couple. In platinization, the PSI receives an electron from the Asc/Dc reductant couple that is dissolved in solution, whereas the PSI in our hybrid Z-scheme received an electron from the directly linked metal. Similarly, in nature, the bound mediator PC transfers an electron directly to the lumen side of the PSI. [32] Thus, we hypothesized that our all-linked system effectively realized an electron transfer chain and exhibited enhanced or comparable activity for the PSI relative to the half-reaction system with a chemical electron donor. In addition, we expect that the linker could be designed to significantly enhance the activity even further.

The Au mediator more than doubled the H_2 evolution activity over that of

the Ag mediator. Considering the improved quenching of PL in the Ag-mediated Z-scheme over the Au-mediated Z-scheme, it was interesting that the Au mediator showed significantly higher H_2 evolution activity. We hypothesize that the Au provided a moderate metal-to-$BiVO_4$ potential barrier that prevented electron back transfer, whereas the small potential barrier in Ag-$BiVO_4$ could easily have induced the back transfer of electrons. **Figure 4.12** illustrates the energy band position of the semiconductor and metal part. We also expect that a suitable surface plasmon resonance of Au could contribute to enhanced photo-activity.[42] Ag also exhibits a considerable plasmon effect; however, the resonance wavelength of Ag is located at the edge of our light source spectrum.[43] Recently, light absorption enhancement has been demonstrated by the plasmon effect of Ag nanoparticles in an all-solid-state Z-scheme.[44-46] We expect that the Au nanoparticles in the hybrid Z-scheme could also provide extra absorption and enhance the electron supply to the PSI. In addition, other roles of Au nanoparticle as a hot electron source or a hole scavenger should be considered in order to comprehensively understand the electron mediating pathway through Au nanoparticle.[47]

In this study, we have successfully demonstrated the first hybrid Z-scheme for H_2 evolution. The final scheme of the Z-scheme mediated by Au metal are shown in **Figure 4.13**. Our hybrid Z-scheme was designed to split water and evolve H_2 as a final product at PtPSI. Thus, we expected that O_2 would evolve on the semiconductor side as a water oxidation product, but we also considered the possibility of the evolution of reactive oxygen species, such as hydroxyl and superoxide anion radicals. These radicals are commonly reported to be detected in metal(oxide)-doped semiconductors in competition with O_2 and H_2.[48, 49] In the

current study, we did not perform quantitative measurements of all of the oxygen species from the Z-scheme, and we are currently investigating the use of isotope labeled H_2O^{18} as a reactant to categorize and quantify the direct products. Despite the insufficient analysis of the oxygen reaction products, we were still able to verify the successful operation of the hybrid Z-scheme by measuring the target product, H_2. First, the use of the hybrid Z-scheme was successful in realizing the protein-photocatalyst system for the evolution of water-sacrificed, visible light-driven H_2. Moreover, we demonstrated the effects of a directly linked structure and plasmonic nanoparticle mediators on the activity of the system. Thus, the issues that were explored in this study can open new avenues in the development of other protein hybrid systems for various applications.

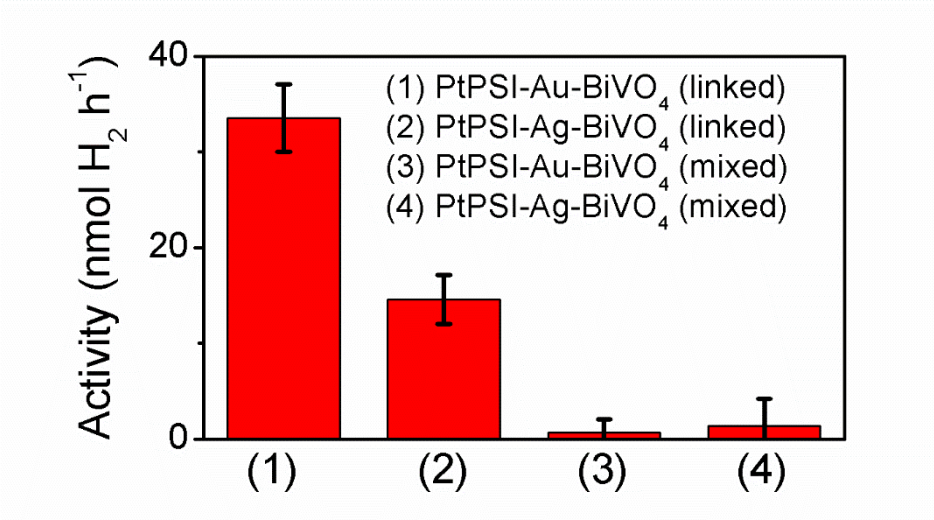

Figure 4.10. Hydrogen evolution activity measured by GC (for 1 g of sample). The average hydrogen evolution activity for 48 h.

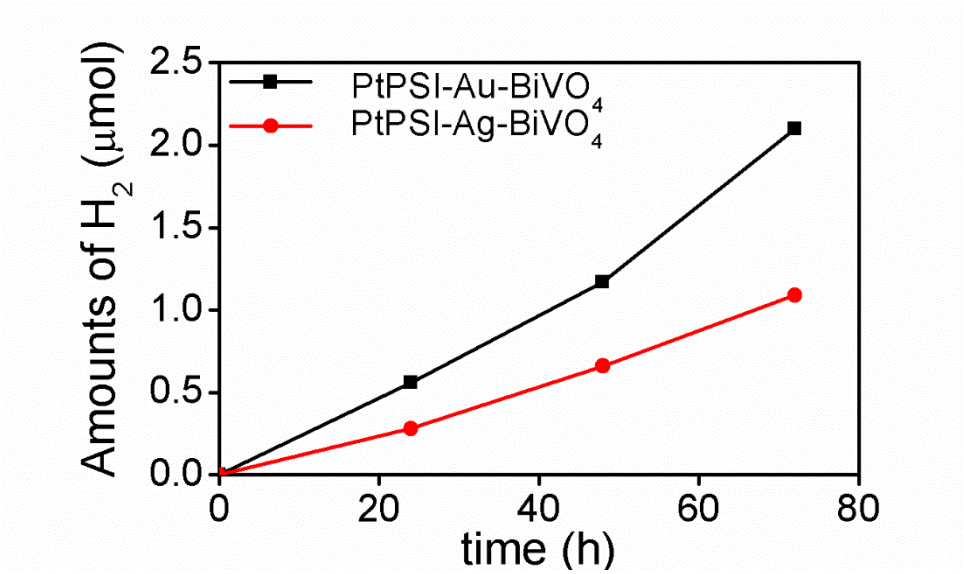

Figure 4.11. The hydrogen evolution activity as a function of operation time. The produced hydrogen was measured every 24 h from the same sample.

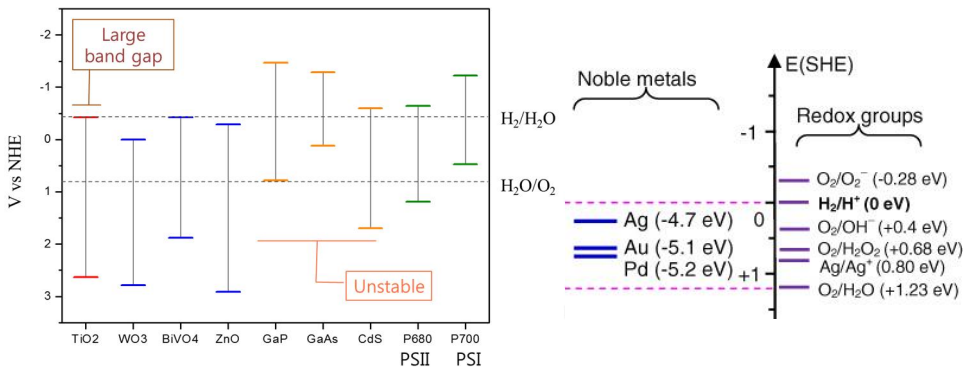

Figure 4.12. Energy band diagrams of various semiconductors (left) and metals (right).

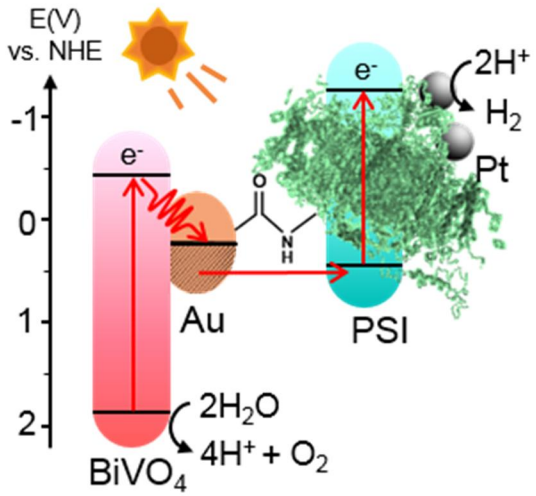

Figure 4.13. The all-solid-state hybrid Z-scheme composed of $BiVO_4$, Au and PSI.

4.4 Conclusion

We developed a hybrid Z-scheme for H_2 evolution by integrating $BiVO_4$ and a PtPSI in an all-solid-state. Under visible light, our system showed the ability to evolve hydrogen from water without the use of additional sacrificial agents or redox mediators for the first time. The water-sacrificed H_2 evolution was a successful demonstration of the utility of a PSI as a photocatalytic material. In designing this structure, we constructed an all-linked hybrid system using Au and Ag nanoparticle conductors. The positive effect of direct linking between a protein and a metal mediator was revealed by effective PL quenching and enhanced H_2 evolution activity. We demonstrated the enhanced activity of PSI over that of a solvent-based sacrificial reaction and found that the plasmon effect of the metal could further amplify the electron supply.

Various proteins, including enzymes, photosynthetic proteins and immunoproteins, have the intrinsic capability to be used as desirable and functional materials. However, one of the remaining challenges in the practical application of proteins is the hybridization of proteins with artificially constructed systems. In our hybrid system, both a hybridized semiconductor and a photosystem participated in the key photo-electrochemical reaction. This hybrid system provides a new means of using a photosynthetic protein as a practical material in the design of a photocatalytic energy producing system. Thus, we fully and simultaneously exploited the functionality of these synthetic and biological materials, going beyond using these materials simply as a support for another material.

Our hybrid system can serve as a novel and interesting model for

constructing protein-hybrid systems. This study can also help to understand the communication mechanism in biohybrid systems and develop manufacturing technologies for optimized systems at the molecular scale.

Reference

1. Brettel, K. & Leibl, W. Electron transfer in photosystem I. *Biochimica et Biophysica Acta (BBA) - Bioenergetics* **1507**, 100-114 (2001).
2. Brettel, K. Electron transfer and arrangement of the redox cofactors in photosystem I. *Biochimica et Biophysica Acta (BBA) - Bioenergetics* **1318**, 322-373 (1997).
3. Hall, D.O., Rao, K. & Biology, I.o. Photosynthesis. (Cambridge University Press, 1999).
4. Bard, A.J. Photoelectrochemistry and heterogeneous photo-catalysis at semiconductors. *Journal of Photochemistry* **10,** 59-75 (1979).
5. Sasaki, Y., Kato, H. & Kudo, A. $[Co(bpy)_3]^{3+/2+}$ and $[Co(phen)_3]^{3+/2+}$ Electron Mediators for Overall Water Splitting under Sunlight Irradiation Using Z-Scheme Photocatalyst System. *Journal of the American Chemical Society* **135**, 5441-5449 (2013).
6. Kato, H., Sasaki, Y., Shirakura, N. & Kudo, A. Synthesis of highly active rhodium-doped $SrTiO_3$ powders in Z-scheme systems for visible-light-driven photocatalytic overall water splitting. *Journal of Materials Chemistry A* **1,** 12327-12333 (2013).
7. Qi, J. et al. Multi-shelled CeO_2 hollow microspheres as superior photocatalysts for water oxidation. *Nanoscale* **6**, 4072-4077 (2014).
8. Maeda, K., Higashi, M., Lu, D., Abe, R. & Domen, K. Efficient Nonsacrificial Water Splitting through Two-Step Photoexcitation by Visible Light using a Modified Oxynitride as a Hydrogen Evolution

Photocatalyst. *Journal of the American Chemical Society* **132**, 5858-5868 (2010).

9. Maeda, K., Saito, N., Lu, D., Inoue, Y. & Domen, K. Photocatalytic Properties of RuO_2-Loaded β-Ge_3N_4 for Overall Water Splitting. *The Journal of Physical Chemistry C* **111**, 4749-4755 (2007).

10. Ran, J., Zhang, J., Yu, J. & Qiao, S.Z. Enhanced Visible-Light Photocatalytic H2 Production by ZnxCd1−xS Modified with Earth-Abundant Nickel-Based Cocatalysts. *ChemSusChem* **7**, 3426-3434 (2014).

11. Ran, J., Zhang, J., Yu, J., Jaroniec, M. & Qiao, S.Z. Earth-abundant cocatalysts for semiconductor-based photocatalytic water splitting. *Chemical Society reviews* **43**, 7787-7812 (2014).

12. Iwase, A., Ng, Y.H., Ishiguro, Y., Kudo, A. & Amal, R. Reduced Graphene Oxide as a Solid-State Electron Mediator in Z-Scheme Photocatalytic Water Splitting under Visible Light. *Journal of the American Chemical Society* **133**, 11054-11057 (2011).

13. Yun, H.J. et al. A Combination of Two Visible-Light Responsive Photocatalysts for Achieving the Z-Scheme in the Solid State. *ACS Nano* **5**, 4084-4090 (2011).

14. Maeda, K. et al. Photocatalyst releasing hydrogen from water. *Nature* **440,** 295-295 (2006).

15. Lee, Y. et al. Zinc Germanium Oxynitride as a Photocatalyst for Overall Water Splitting under Visible Light. *The Journal of Physical Chemistry C* **111**, 1042-1048 (2006).

16. Iwuchukwu, I.J. et al. Self-organized photosynthetic nanoparticle for cell-

free hydrogen production. *Nat. Nanotechnol.* **5**, 73-79 (2010).

17. Millsaps, J.F., Bruce, B.D., Lee, J.W. & Greenbaum, E. Nanoscale Photosynthesis: Photocatalytic Production of Hydrogen by Platinized Photosystem I Reaction Centers. *Photochemistry and Photobiology* **73**, 630-635 (2001).

18. Evans, B.R., O'Neill, H.M., Hutchens, S.A., Bruce, B.D. & Greenbaum, E. Enhanced Photocatalytic Hydrogen Evolution by Covalent Attachment of Plastocyanin to Photosystem I. *Nano Lett.* **4**, 1815-1819 (2004).

19. Grimme, R.A., Lubner, C.E., Bryant, D.A. & Golbeck, J.H. Photosystem I/Molecular Wire/Metal Nanoparticle Bioconjugates for the Photocatalytic Production of H_2. *Journal of the American Chemical Society* **130**, 6308-6309 (2008).

20. Grimme, R.A., Lubner, C.E. & Golbeck, J.H. Maximizing H_2 production in Photosystem I/dithiol molecular wire/platinum nanoparticle bioconjugates. *Dalton Trans.*, 10106-10113 (2009).

21. Ihara, M. et al. Light-driven Hydrogen Production by a Hybrid Complex of a [NiFe]-Hydrogenase and the Cyanobacterial Photosystem I. *Photochemistry and Photobiology* **82**, 676-682 (2006).

22. Ihara, M., Nakamoto, H., Kamachi, T., Okura, I. & Maedal, M. Photoinduced Hydrogen Production by Direct Electron Transfer from Photosystem I Cross-Linked with Cytochrome c3 to [NiFe]-Hydrogenase. *Photochemistry and photobiology* **82**, 1677-1685 (2006).

23. Krassen, H. et al. Photosynthetic Hydrogen Production by a Hybrid Complex of Photosystem I and [NiFe]-Hydrogenase. *ACS Nano* **3**, 4055-

4061 (2009).

24. Lubner, C.E. et al. Wiring an [FeFe]-Hydrogenase with Photosystem I for Light-Induced Hydrogen Production. *Biochemistry* **49**, 10264-10266 (2010).

25. Lubner, C.E. et al. Solar hydrogen-producing bionanodevice outperforms natural photosynthesis. *Proceedings of the National Academy of Sciences* **108**, 20988-20991 (2011).

26. Silver, S.C. et al. Protein Delivery of a Ni Catalyst to Photosystem I for Light-Driven Hydrogen Production. *Journal of the American Chemical Society* **135**, 13246-13249 (2013).

27. Utschig, L.M., Silver, S.C., Mulfort, K.L. & Tiede, D.M. Nature-Driven Photochemistry for Catalytic Solar Hydrogen Production: A Photosystem I–Transition Metal Catalyst Hybrid. *Journal of the American Chemical Society* **133**, 16334-16337 (2011).

28. Zhou, P., Yu, J. & Jaroniec, M. All-Solid-State Z-Scheme Photocatalytic Systems. *Adv. Mater.* **26**, 4920-4935 (2014).

29. Yu, Z.B. et al. Self-assembled CdS/Au/ZnO heterostructure induced by surface polar charges for efficient photocatalytic hydrogen evolution. *Journal of Materials Chemistry A* **1**, 2773-2776 (2013).

30. Tada, H., Mitsui, T., Kiyonaga, T., Akita, T. & Tanaka, K. All-solid-state Z-scheme in CdS-Au-TiO_2 three-component nanojunction system. *Nat. Mater.* **5**, 782-786 (2006).

31. Wang, X. et al. ZnO–CdS@Cd Heterostructure for Effective Photocatalytic Hydrogen Generation. *Advanced Energy Materials* **2**, 42-46 (2012).

32. Guan, M.-L., Ma, D.-K., Hu, S.-W., Chen, Y.-J. & Huang, S.-M. From Hollow Olive-Shaped $BiVO_4$ to n–p Core–Shell $BiVO_4$@Bi_2O_3 Microspheres: Controlled Synthesis and Enhanced Visible-Light-Responsive Photocatalytic Properties. *Inorganic Chemistry* **50**, 800-805 (2010).

33. Zhang, T., Wang, C., Liu, S., Wang, J.-L. & Lin, W. A Biomimetic Copper Water Oxidation Catalyst with Low Overpotential. *Journal of the American Chemical Society* **136**, 273-281 (2013).

34. Nakamura, A., Suzawa, T., Kato, Y. & Watanabe, T. Significant species-dependence of P700 redox potential as verified by spectroelectrochemistry: Comparison of spinach and Theromosynechococcus elongatus. *FEBS Letters* **579**, 2273-2276 (2005).

35. Qin, X. et al. Rapid purification of photosystem I chlorophyll-binding proteins by differential centrifugation and vertical rotor. *Photosynthesis Research* **90**, 195-204 (2006).

36. Arnon, D.I. COPPER ENZYMES IN ISOLATED CHLOROPLASTS. POLYPHENOLOXIDASE IN BETA VULGARIS. *Plant Physiology* **24**, 1-15 (1949).

37. Wang, D. et al. Photocatalytic Water Oxidation on BiVO4 with the Electrocatalyst as an Oxidation Cocatalyst: Essential Relations between Electrocatalyst and Photocatalyst. *The Journal of Physical Chemistry C* **116**, 5082-5089 (2012).

38. Suemori, Y. et al. Self-assembled monolayer of light-harvesting core complexes of photosynthetic bacteria on an amino-terminated ITO

electrode. *Photosynthesis Research* **90**, 17-21 (2006).

39. Li, R.G. et al. Spatial separation of photogenerated electrons and holes among {010} and {110} crystal facets of $BiVO_4$. *Nat. Commun.* **4** (2013).

40. Kudo, A., Omori, K. & Kato, H. A Novel Aqueous Process for Preparation of Crystal Form-Controlled and Highly Crystalline $BiVO_4$ Powder from Layered Vanadates at Room Temperature and Its Photocatalytic and Photophysical Properties. *Journal of the American Chemical Society* **121**, 11459-11467 (1999).

41. Li, C. et al. Selective Deposition of Ag_3PO_4 on Monoclinic $BiVO_4$(040) for Highly Efficient Photocatalysis. *Small* **9**, 3951-3956 (2013).

42. Rodríguez-Fernández, J., Pérez-Juste, J., García de Abajo, F.J. & Liz-Marzán, L.M. Seeded Growth of Submicron Au Colloids with Quadrupole Plasmon Resonance Modes. *Langmuir* **22**, 7007-7010 (2006).

43. Liang, H. et al. Controlled Synthesis of Uniform Silver Nanospheres†. *The Journal of Physical Chemistry C* **114**, 7427-7431 (2010).

44. Wang, X., Li, S., Ma, Y., Yu, H. & Yu, J. $H_2WO_4 \cdot H_2O$/Ag/AgCl Composite Nanoplates: A Plasmonic Z-Scheme Visible-Light Photocatalyst. *The Journal of Physical Chemistry C* **115**, 14648-14655 (2011).

45. Hou, J. et al. Hierarchically Plasmonic Z-Scheme Photocatalyst of Ag/AgCl Nanocrystals Decorated Mesoporous Single-Crystalline Metastable $Bi_{20}TiO_{32}$ Nanosheets. *The Journal of Physical Chemistry C* **117**, 5132-5141 (2013).

46. Ye, L. et al. Two Different Roles of Metallic Ag on Ag/AgX/BiOX (X = Cl, Br) Visible Light Photocatalysts: Surface Plasmon Resonance and Z-

Scheme Bridge. *ACS Catalysis* **2**, 1677-1683 (2012).

47. Ma, X. et al. New Insight into the Role of Gold Nanoparticles in Au@CdS Core–Shell Nanostructures for Hydrogen Evolution. *Small* **10**, 4664-4670 (2014).

48. Ge, L. Novel Pd/$BiVO_4$ composite photocatalysts for efficient degradation of methyl orange under visible light irradiation. *Materials Chemistry and Physics* **107**, 465-470 (2008).

49. Kohtani, S. et al. Loading effects of silver oxides upon generation of reactive oxygen species in semiconductor photocatalysis. *Phys. Chem. Chem. Phys.* **10**, 2986-2992 (2008).

Chapter 5. Electrochemical carboxylation of unsaturated hydrocarbons using CO_2

5.1 Introduction

Carbon dioxide (CO_2) fixation in natural photosynthesis (e.g. RuBisCO) occurs by carboxylation of unsaturated carbon bond in enediolate intermediates.[1,2] Recently, a similar mechanism of CO_2 insertion at the unsaturated carbon bond has been adopted in the synthesis of carboxylic acids employing alkynes,[3-6] α-olefins[7,8] and internal alkenes as substrates.[9-12] These methods enabled CO_2 to be harnessed as a renewable one-carbon building block; however, the valorization of CO_2 is still challenging because the gas is thermodynamically and kinetically stable.[13] Consequently, numerous advances in chemical carboxylation using CO_2 have relied on highly reactive organometallic nucleophiles to facilitate the reaction.[13,14] Recent reports have demonstrated that the elaborate design of organometallic nucleophiles is the primary requisite for modulation of site-selectivity and extension of substrates in carboxylation.[14-16] In addition, because the reduction step is necessary to utilize the completely oxidized carbon atom of CO_2, chemical reductants are typically used.[14,16] Recently, Martin and coworkers developed an elegant protocol for site-selectivity tunable carboxylation via nickel hydride or nickelalactone formation using manganese as a reductant for the extensive scope of unsaturated hydrocarbons, such as styrenes, alkenes and alkynes.[17] As an alternative approach, heterogeneously catalyzed carboxylation using electrochemistry has gained increasing attention. These carboxylation reactions are mainly driven by reductive

electrical potential on a cathode electrode.[18-20] Among the unsaturated hydrocarbon feedstocks, this study focused on the electrochemical carboxylation of styrene as a representative model.

In the carboxylation of styrene using CO_2, hydrocarboxylation of the α- or β-position and dicarboxylation at both positions are feasible. Vianello and coworkers first pioneered the electrochemical dicarboxylation of styrene to 2-phenylsuccinic acid (**1**).[21] Since then, several succeeding works on the electrochemical carboxylation of styrene have reported dicarboxylation as a primary reaction both in the presence[22,23] and absence[24-26] of homogeneous catalysts. These studies proposed the electrochemical formation of β-carboxylate radical anions as a key intermediate, followed by additional CO_2 insertion to the benzylic position.[24,26] However, it has been hypothesized that the electrochemical carboxylation of styrene is mostly carried out by the dicarboxylaion pathway.

In contrast, chemical carboxylation of styrene has been actively studied, ranging from dicarboxylation to hydrocarboxylation either with Markovnikov or anti-Markovnikov regioselectivity. Notably, pioneering works have progressed to modulate site-selectivity by developing novel chemical protocols,[27,28] metal catalysts,[29-31] and catalyst ligands.[29,30,32,33] Most of the works using metal catalysts reported α-hydrocarboxylation as a major reaction due to the preference for forming stable η^3 benzylic metal species.[29-31,34] This process facilitates Markovnikov hydrocarboxylation where the proton of the metal hydride first binds to the β-position and then CO_2 later binds to the benzylic position. In the case of β-hydrocarboxylation, CO_2 insertion at the β-position occurs prior to protonation which is the reverse order to that for α-hydrocarboxylation as noted recently by the

Jamison group[28] and the König group.[32] Both works achieved high selectivity for the β-position by activating CO_2 in the initial process of hydrocarboxylation using photocatalysts. Additionally, König demonstrated that different intermediates resulting from employed ligands determine site selectivity between α- and β-hydrocarboxylation.[32]

Inspired by these predictive selectivities in chemical carboxylation, we envisioned that electrochemical carboxylation would be extended to site-selective hydrocarboxylation by controlling the protonation process. Because β-carboxylate is the key intermediate during electrical reduction, we thought that intentional protonation might suppress successive CO_2 insertion to form **1** (**Figure 5.1**, top) and result in β-hydrocarboxylation to form hydrocinnamic acid (**2**) (**Figure 5.1**, bottom). We employed water as a clean and abundant proton source and precisely explored the effect on the yield and selectivity of products. Surprisingly, this new β-hydrocarboxylation reaction appeared to exhibit selectivity of 96% towards **2** which has never been reported. A mechanistic investigation of electrochemical β-hydrocarboxylation was also conducted in this study. For the ongoing work, we also extended the substrate to aliphatic α-olefins using the electrochemical platform.

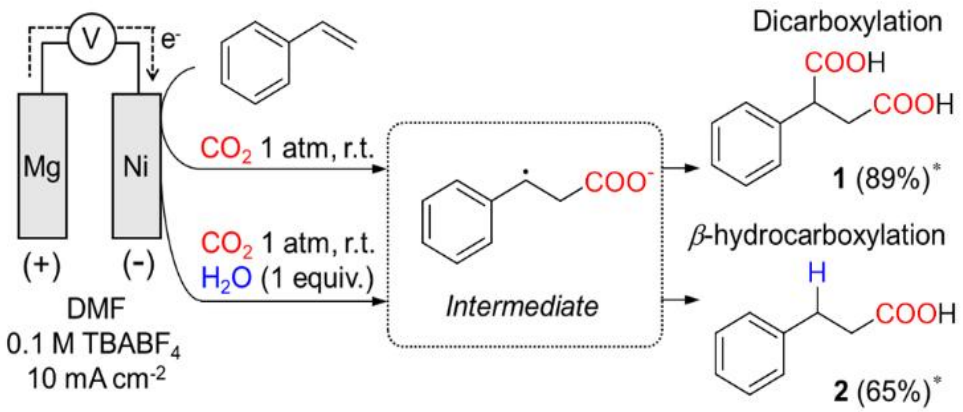

Figure 5.1. Electrochemical carboxylation of styrene with CO_2. *Faradaic efficiency.

5.2 Experimental and analysis

5.2.1 Materials

Hydrocinnamic acid, 2-phenylsuccinic acid, styrene, all styrene derivatives, tetrabutylammonium tetrafluoroborate ($TBABF_4$) and tetramethylsilane (TMS) were purchased from TCI chemicals (Tokyo, Japan). Chloroform-*d* ($CDCl_3$) and dimethyl sulfoxide-*d*6 (DMSO-*d*6) were purchased from Acros Organics (Geel, Belgium). Iodomethane and magnesium sulfate ($MgSO_4$) were purchased from Sigma-Aldrich (Milwaukee, WI, USA). Acetic acid, acetonitrile, *tert*-butanol, *N*,*N*-dimethylformamide (DMF), diethyl ether, hydrochloric acid (HCl), methanol, phenol, potassium carbonate (K_2CO_3) and sodium hydroxide (NaOH) were purchased from Daejung chemicals (Gyenonggido, Korea). DMF was dried with 4 Å molecular sieve, and all other chemicals were used as received. Purified deionized water (18.2 $M\Omega cm^{-1}$) was used in the procedures. Nickel foil (Ni, 0.1 mm thick), titanium foil (Ti, 0.127 mm thick), platinum foil (Pt, 0.025 mm thick) and magnesium foil (Mg, 0.25 mm thick) were purchased from Alfa Aesar (MA, USA).

5.2.2 Electrochemical analysis

An undivided three-electrode cell equipped with a gas line was used in all voltammetric measurements and electrolysis. Ni, Ti, and Pt with surface dimensions of 1 cm × 2.5 cm and Mg with surface dimensions of 1 cm × 3 cm were used as the working electrode and counter electrode, respectively. Prior to use, the

metal foils were polished with sandpaper, cleaned with diluted HCl (aq.) and rinsed with distilled water. The reference electrode was Ag/Ag^+ (0.01 M)/$TBABF_4$ (0.1 M) in acetonitrile. For the electrolyte, $TBABF_4$ (0.1 M) was put in dried DMF and saturated with CO_2 by purging the gas for 1 h. Then, 4 mL of the solution was put into the reactor cell at a volume of 50 mL. The reactants were injected into the electrolyte, and the headspace of the cell was ventilated with CO_2 gas for 0.5 h and closed tightly under CO_2 at atmospheric pressure. All reactions were performed at room temperature under vigorous stirring of the electrolyte. After electrolysis, 1 mL of headspace gas was transferred by syringe for gas chromatography (GC) analysis. The solutions in the reactor cell were acidified with HCl (2 M, aq.) for 3 h and extracted with diethyl ether (3 × 20 mL). The organic layer was washed with distilled water, dried over $MgSO_4$ and evaporated. The isolated products were dissolved in deuterated solvents for nuclear magnetic resonance (NMR) analysis or diethyl ether for gas chromatography-mass spectrometry (GC-MS) analysis.

5.2.3 Analytical methods

NMR spectra were recorded on a JEOL 400 MHz NMR spectrometer (JeolJMN-LA400) or Bruker 600 MHz NMR spectrometer (Bruker Avance 600) at room temperature. Chemical shifts were reported in parts per million (ppm) downfield of TMS (δ = 0.00 ppm). Products were dissolved into 0.7 mL of DMSO-*d*6 or $CDCl_3$. A potentiostat (CHI 760E, CH Instruments) was used for voltammetric measurements and bulk electrolysis. All potentials were controlled against the reference electrode and recorded after IR compensation. The

quantitative measurement of the gas phase from the headspace of the electrochemical cell was performed by GC (PerkinElmer, NARL8502 Model 4003). Liquid- and solid-phase products dissolved in the organic solvents were detected by GC-MS (Agilent 5977) using an automatic liquid sampler.

5.3 Results and discussion

5.3.1 Electrochemical carboxylation of styrene

We first performed the electrochemical carboxylation of styrene using CO_2 without any proton source. Three electrode systems with a Ni cathode, Mg anode and Ag/Ag^+ (0.01 M)/ tetrabutylammonium tetrafluoroborate ($TBABF_4$, 0.1 M) reference electrode were used in *N,N*-dimethylformamide (DMF) and $TBABF_4$ (0.1 M) electrolyte. To investigate voltammetric behavior of styrene, linear sweep voltammetry scans were recorded at a 20 mV s^{-1} scan rate with IR compensation (**Figure 5.2**). As shown in the enlarged scans shown in **Figure 5.3**, observed onset potential of CO_2 (saturated in the electrolyte) and styrene (0.1 M, in Ar-saturated electrolyte) are -2.6 V and -2.7 V (vs Ag/Ag^+), respectively. Then, various concentration of styrene up to 0.2 M were added to the CO_2-saturated electrolyte. As a result, current density gradually enhanced with the addition of styrene, while all the onset potentials appeared at the range between the onset potential of CO_2 and styrene. This observation indicates simultaneous electrical reduction of both CO_2 and styrene above the onset potential as was surmised in previous reports.[24,26] However, the increase of current density reached saturation in the case of styrene concentration above 0.1 M, which may originate from saturated active sites on the surface in the presence of abundant styrene. Therefore, the concentration of styrene was fixed to 0.1 M in the following analysis.

The effect of protons on styrene carboxylation was investigated by adding various concentrations of water. First, linear sweep voltammetry scans were recorded by enhancing the water concentrations up to 0.4 M at a 20 mV s^{-1} scan

rate with IR compensation as shown in **Figure. 5.4**. The onset potential was observed at identical potential until the water concentration increased to 0.05 M and shifted to positive direction at higher water concentrations above 0.1 M. Also, as shown in the enlarged cyclic voltammetry scan with 0.1 M H_2O (**Figure 5.5**), new reduction current of ~0.2 mA cm^{-2} was observed from the applied potential of -1.7 V (vs Ag/Ag^{+}). These results indicate the occurrence of a new reduction reaction in the presence of water which turned out to be a hydrogen evolution reaction (HER), as will be discussed later. Moreover, enhanced charging current was observed in the case of adding 0.1 M H_2O, but the current level was still smaller than 0.4 mA cm^{-2} before the onset potential. This shows possible double layer effect of proton source in the electrolyte while the effectiveness may not significant considering the small current level. To determine the rate-determining step (RDS), Tafel slopes were measured for the cases of 0, 0.05 and 0.1 M water, where a negligible shift of the onset potentials was observed (**Figure 5.6**). The currents were obtained from the partial current density of carboxylation reaction calculated by faradaic efficiency of carboxylic acid products. The measured slope value was between 113 and 120 mV dec^{-1}, which suggests that one electron is involved in the RDS.[35] As a result, we thought that the formation of $CO_2^{\bullet-}$ or $[Styrene]^{\bullet-}$ could correspond to the RDS.

For the electrochemical electrolysis, 20 C of charge was passed under constant negative potential. The current density of 10 mA cm^{-2} was stably maintained during electrolysis for ~2000 s, as shown in **Figure 5.7**. The carboxylate products were acidified with HCl (2 M), extracted with ether and isolated after solvent distillation. The final carboxylic acids were characterized

using proton nuclear magnetic resonance spectroscopy (^{1}H NMR, 400 MHz, DMSO-*d*6). The ^{1}H NMR spectra clearly showed the change in peak intensity of **1** and **2** by adding water (**Figure 5.8**). The observed ^{1}H NMR spectra of electrolyte also showed the peak of residual styrene, DMSO-*d*6, DMF and water, but no other peaks of by products such as polymerized or reduced styrenes are detected. Along with the carboxylic acids in the electrolyte, the gas products from the headspace of the reactor, such as hydrogen, carbon monoxide and methane, were analyzed by gas chromatography (GC).

Based on the ^{1}H NMR and GC results, the yields of each product from the styrene carboxylation were obtained based on faradaic efficiency (FE) in the presence of different amounts of water (**Figure 5.9** and **Table 5.1**). Among acid products, the selectivity of **2** to **1** dramatically increased from 3% to 96% as the water concentration increased from 0 M (**Table 5.1**, entry 1) to 1 M (**Table 5.1**, entry 11). This result clearly shows a change in the carboxylation pathway from dicarboxylation to *β*-hydrocarboxylation. However, in terms of product yield, the maximum FE of **2** was obtained at 0.1 M water which is 1 equivalent relative to styrene (65%, **Table 5.1**, entry 5) and gradually decreased to 47% when water was added up to 1 M (**Table 5.1**, entry 11). This decline in *β*-hydrocarboxylation can be explained by the increasing gas production. In particular, FE of hydrogen significantly increased from 3.2% to 15% as the water concentration increased from 0.1 M to 0.2 M (**Table 5.1**, entries 5 and 7) and even increased up to 44% at 1 M water (**Table 5.1**, entry 11). Among the CO_2 reduction reactions, the production of CH_4 gradually increased, exhibiting a maximum FE of 6.7% in 0.3 M water (**Table 5.1**, entry 8). The result indicates that excess water above 0.1 M (1

equivalent relative to styrene) in the electrolyte is used mostly in the HER and partially in CH_4 production. This increase in gas production also corresponds to the positive shift of the onset potential in voltammetry scans at water concentrations above 0.1 M. Consequently, it is clearly evident that the amount of water present in the reaction system is crucial in controlling both the selectivity and reactivity in the carboxylation of styrene.

In addition, the effect of water acidity on the product selectivity was investigated by using diluted HCl. In detail, the equivalent amount of 2 M HCl in terms of protons was used instead of 0.05 M and 0.1 M neutral water, which was expected to enhance the free proton concentrations to pH 2.74 and 2.44, respectively (**Table. 5.1**, entries 4 and 6). The selectivity of **2** was slightly enhanced in both cases using HCl, which were comparable to the cases that used a twofold amount of neutral water.

The effect of electrode catalyst was investigated by using Ti and Pt as cathode. For the electrochemical analysis, linear sweep voltammetry scans were recorded with 0, 0.05 M, 0.1 M and 0.4 M water at a 20 mV s^{-1} scan rate in CO_2-saturated DMF and $TBABF_4$ (0.1 M) electrolyte under an atmosphere of CO_2 (**Figure 5.10 (a)** and **(b)**). In both cases, the onset potentials shifted positively by adding water. Especially, on a Pt electrode, current from HER at -1.7 V (vs Ag/Ag^+) was largely appeared compared to Ti and Ni electrodes. The acids and gas products from the styrene carboxylation using Ti and Pt electrode were also detected under the same electrolysis condition which was used in the case of Ni electrode in Fig.3. The calculated FE values of products using Ti and Pt electrode are shown in **Figure 5.10 (c)** and **(d)**. In both cases, the change tendency of products under 0 M to 0.4

M water was analogous to the case of Ni electrode, where the yield of **1** decreased while that of **2** and HER increased by adding water. However, compared to a Ni electrode, both cases showed smaller yield of **2** in the presence of water, due to the rapid enhancement of HER and slower shift of selectivity towards **2** to **1**. As also observed in the voltammetry scan, Pt electrode showed the highest activity for HER where the FE of hydrogen reached to 38% and 61% at 0.1 M and 0.4 M water while the maximum yield of **2** was only 29% at 0.4 M water. On a Ti electrode, the HER were observed by FE of 18% and 40% at 0.1 M and 0.4 M water and maximum yield of **2** was 44% at 0.1 M water. Consequently, Ni electrode turned out to be the best catalyst for β-hydrocarboxylation of styrene among these metals.

Various protic solvents with increasing pK_a value were also used instead of water to explore the effect of proton sources on the selectivity towards **2** (**Table 5.2**). Based on the result that high concentration and acidity of water enhanced selectivity towards **2**, we employed various alcohols and carboxylic acids to investigate the effect of acidity of protic solvents on product selectivity. However, regardless of the pK_a value, all the protic solvents resulted in reduced selectivity towards **2** compared to the case using same amount of water. Moreover, the trend of carboxylation selectivity showed no clear correlation to the proton donating ability of protic solvents. Whereas, in the presence of strong proton donor such as acetic acid and phenol (**Table 5.2**, entry 1 and 2), yield of HER increased significantly compared to the case using water. Because this reaction occurs on heterogeneously catalyzed condition, we think that intrinsic proton donating ability of protic solvent does not determine the overall selectivity during the reaction. Instead, binding affinity to electrode may influence the reaction pathway, as we

proved the effect of metal electrodes on the carboxylation selectivity. Consequently, among the protic solvents examined here, it was confirmed that water was the most favorable proton source for the β-hydrocarboxylation of styrene under these synthetic conditions.

The influence of current density was also investigated by applying various overpotentials (η) during the electrolysis (**Table 5.3**). To evaluate β-hydrocarboxylation activity, the turnover frequency (TOF) was calculated. When the current density was below 5 mA cm^{-2}, the HER was mainly observed because of the insufficient overpotentials for carboxylation to be favored dominantly over the HER. When overpotential was increased to 220 mV, a dramatic enhancement of the acid products was observed, yielding 91% along with a high TOF of 10 s^{-1} (**Table 5.3**, entry 3). The TOF further reached 38 s^{-1} at a 660 mV overpotential (**Table 5.3**, entry 5) along with the negligible change in the selectivity between **1** and **2**.

After optimizing the reaction condition for the β-hydrocarboxylation of styrene, the substrate generality of this electrochemical protocol was investigated. The condition that exhibited maximum yield of **2** using 1 equivalent water was utilized for the reactions. First, cathodic linear sweep voltammetry was measured at 50 mV s^{-1} to evaluate reduction activities as shown in **Figure 5.11**. Compared to styrene, electron-donating substituents such as methoxy group on styrene induced positively shifted onset potential while electron-neutral and electron-withdrawing styrenes possessed comparable or positively shifted onset potentials. Basis on the electrochemical analysis, we conducted electrochemical carboxylation of styrene derivatives with 0.1 M water (**Figure 5.12**). The β-hydrocarboxylation reaction

tolerated electron-donating (**2a**) and electron-neutral (**2b**) styrenes in good yields, and halogen-substituted styrene (**2c-e**) with moderate yields. Notably, in case of **2e** and **2f**, 4-vinylbenzoic acid (**3**) was synthesized as a result of substitution of chlorine or trifluoromethyl group with CO_2, as was also reported in previous study on electrochemical carboxylation.[26] This may be due to the preferable reduction activity of the substituents to the vinyl group. Basis on the investigations, we think that the strong electron withdrawing group attached with benzene ring is easily substituted by CO_2 instead of CO_2 insertion on the vinyl group, while electron-donating and electron-neutral group provides moderate to good yields towards *β*-hydrocarboxylation.

To verify whether the proton used in *β*-hydrocarboxylation comes from water, a deuterium labeling experiment was conducted by fully replacing water with deuterium oxide (D_2O). In the ^1H NMR spectra, D-labeled **2** was observed with 80% deuterium incorporation at the benzylic carbon site as shown in **Figure 5.13**. Moreover, carboxylic acid products were methylated and observed in gas chromatography-mass spectrometry (GC-MS). In the mass spectrum, the ion peak (M^+) of D-labeled methyl-3-phenylpropanoate showed a mass shift of 1 from m/z 164 to 165, which corresponds to labeling with one deuterium atom (**Figure 5.14**). Also, four molecular fragments of D-labeled methyl-3-phenylpropanoate (m/z 78, 92, 105 and 134) showed a mass shift of 1. The only carbon position that these four fragments commonly contain is the benzylic carbon which indicates that deuterium labeling has been carried out at this site. Therefore, basis on the result from both ^1H NMR and GC-MS, we clearly verified that the protonation occurs at a benzylic position by using a proton of water.

After verifying the proton participation in this *β*-hydrocarboxylation, electrokinetic study was investigated by using D_2O as a proton source. In particular, the influence of the protonation step on the overall electrochemical carboxylation of styrene was explored in terms of kinetics. First we recorded cyclic voltammetry scans of the electrochemical carboxylation of styrene (0.1 M) with 0.025 M and 0.1 M D_2O or H_2O. At these proton source concentrations, the selectivity of carboxylation over gas production was above 94%, which could avoid the contribution of other unwanted proton-involved reactions such as the HER. As shown in **Figure 5.15**, no difference was observed in the voltammetric curves between the cases using H_2O and D_2O. This result indicates that a protonation step has no effect on electrokinetics of the carboxylation and proton is not involved in the RDS of this electrochemical carboxylation. In addition, we calculated the yield of acid products from the carboxylation and found out that total FE of acids (**1** + **2**) were only slightly changed from 88% to 85% (entry 2, **Table 5.4**) and 91% to 86% (entry 4, **Table 5.4**). This correlates with the result of cyclic voltammetry scan which shows the overall carboxylation is kinetically independent to H/D exchange. However, at the same time, the selectivity of *β*-hydrocarboxylation towards dicarboxylation significantly decreased when D_2O was used. As a result, the FE of **2** were reduced in the D-labeled cases, from 33% to 20% (entry 2, **Table 5.4**) and 65% to 44% (entry 4, **Table 5.4**), respectively. This result implies that these two carboxylation pathways are in competition with each other and that the capability of protonation largely contributes to tuning the selectivity between pathways.

Based on our collective results, we proposed a reaction pathway for electrochemical *β*-hydrocarboxylation of styrene in the presence of small amount

of water as illustrated in **Figure 5.16**. First, styrene and CO_2 form a β-carboxylate radical intermediate by accepting one electron. This electrical reduction step is the RDS as confirmed by the Tafel analysis and electrokinetic study. From the result that the reduction current has gradually increased by adding reactants, it can be presumed that styrene and CO_2 simultaneously undergo reduction reaction at the applied potential. In terms of onset potential, CO_2 reduction reaction showed more positive onset potential (-2.6 V vs Ag/Ag^+) compared to the styrene reduction reaction (-2.7 V vs Ag/Ag^+) by 100 mV. However, under the reaction condition used here which applies at least 220 mV overpotential, it is still ambiguous to decide the dominant pathway between these two reactions. Because the reduction potential of benzylic radicals are positioned at more positive range than the onset potential (between -1.82 to -0.71 V vs SCE, in acetonitrile),[39] the β-carboxylate radical intermediate could be reduced to β-carboxylate anion. This would avoid unwanted reaction among styrene radicals and result in the absence of polymerized or reduced styrenes during the reaction. Next, protonation takes place at a benzylic position by using a proton, as proved by deuterium labeling analysis, and this protonation leads the reaction to produce **2** via the β-hydrocarboxylation pathway. The dicarboxylation pathway can be explained by the additional incorporation of CO_2 into the benzylic position of the β-carboxylate anion intermediate. Consequently, the competition between the protonation and CO_2 incorporation on the benzylic position determines the final selectivity of this electrochemical carboxylation.

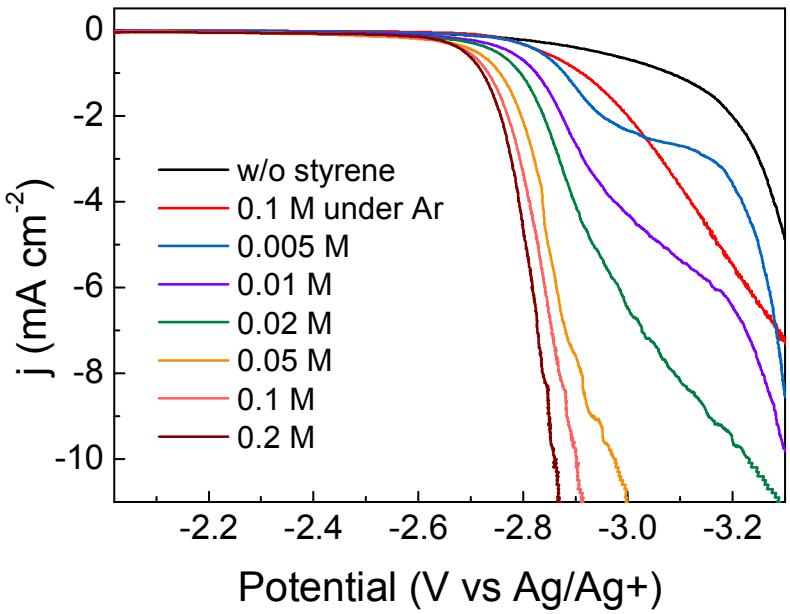

Figure 5.2. Cathodic linear sweep voltammetry data of different concentrations of styrene (0 to 0.2 M) at 20 mV s^{-1}. The measurements were conducted on a Ni electrode in CO_2-saturated DMF and $TBABF_4$ (0.1 M) electrolyte at room temperature and 1 atm CO_2.

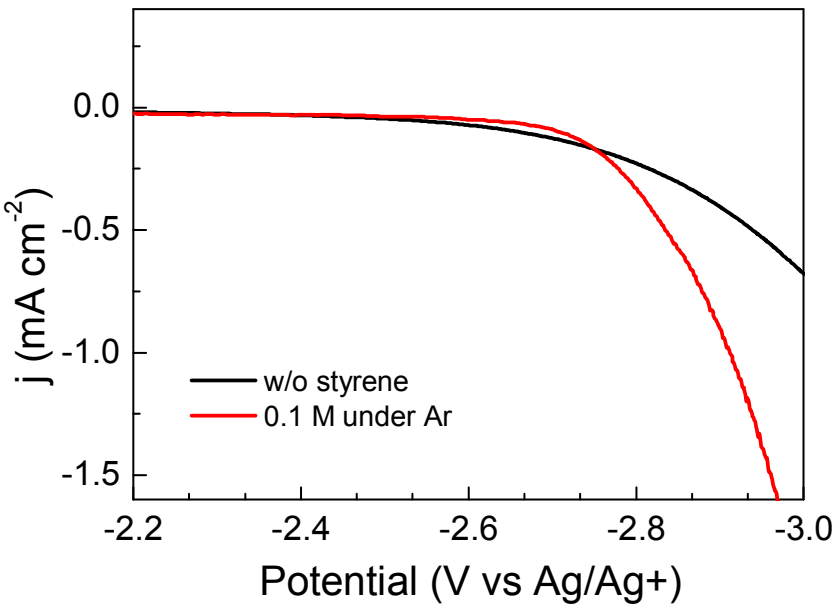

Figure 5.3. Cathodic linear sweep voltammetry data of CO_2-saturated electrolyte under 1 atm CO_2 and 0.1 M styrene in Ar-saturated electrolyte under 1 atm Ar at 20 mV s^{-1}. The measurements were conducted on a Ni electrode in DMF and $TBABF_4$ (0.1 M) electrolyte at room temperature.

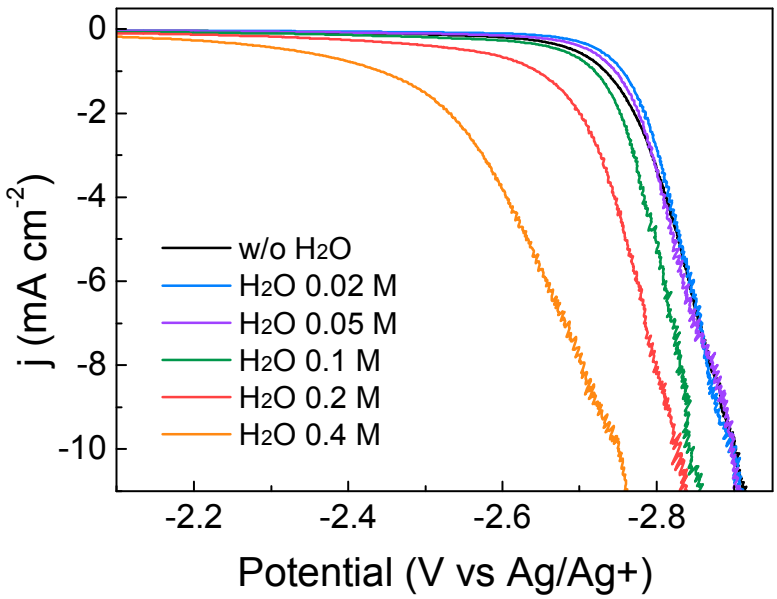

Figure 5.4. Cathodic linear sweep voltammetry data of 0.1 M styrene with various concentrations of H_2O (0 to 0.4 M) at 20 mV s^{-1}. The measurements were conducted on a Ni electrode in CO_2-saturated DMF and $TBABF_4$ (0.1 M) electrolyte at room temperature and 1 atm CO_2.

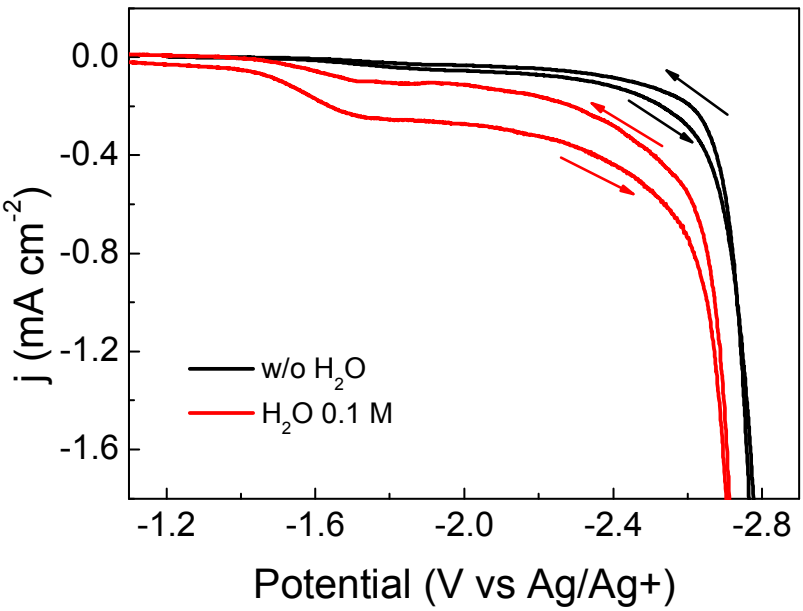

Figure 5.5. Cyclic voltammetry data of 0.1 M styrene without and with 0.1 M H_2O in CO_2-saturated electrolyte under 1 atm CO_2 at 20 mV s^{-1}. The measurements were conducted on a Ni electrode in DMF and $TBABF_4$ (0.1 M) electrolyte at room temperature.

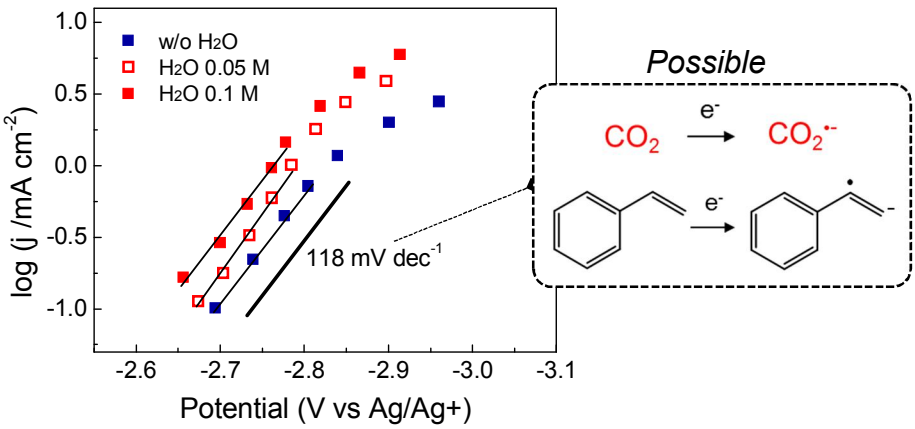

Figure 5.6. Tafel plots from voltammetric measurements of 0.1 M styrene in the presence of 0, 0.05 and 0.1 M H_2O. Current densities are calculated from the partial current densities of carboxylation of styrene.

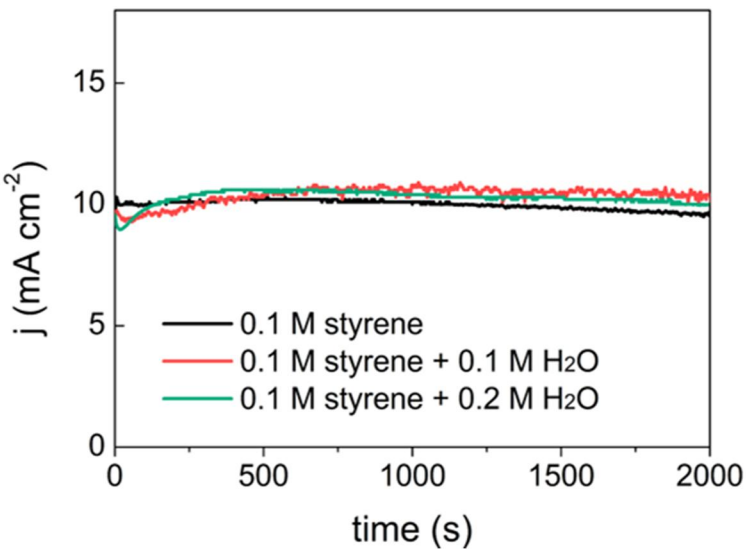

Figure 5.7. Bulk electrolysis of styrene (0.1 M) with different amounts of water. The electrolysis was conducted on the Ni electrode in CO_2-saturated DMF and $TBABF_4$ (0.1 M) electrolyte at room temperature and under 1 atm CO_2. The current density was 10 mA cm^{-2}, and the total charge of 20 C was passed for approximately 2000 s.

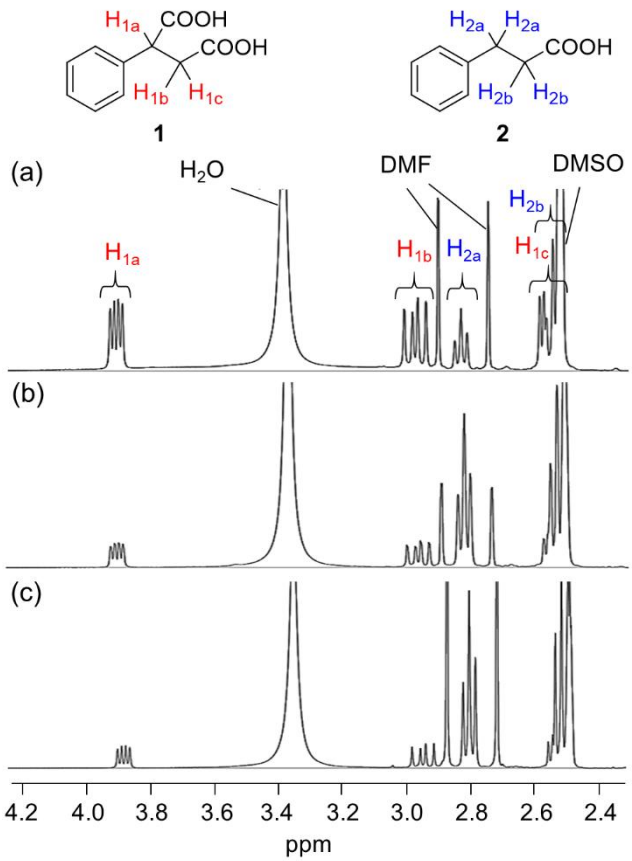

Figure 5.8. ^{1}H NMR spectra of acid products **1** and **2** from the electrolyte after electrochemical carboxylation (400 MHz, DMSO-*d*6). Peaks depicted as H_{1a}, H_{1b} and H_{1c} refer to protons of **1** and H_{2a} and H_{2b} refer to protons of **2**. Residual solvent peaks from water, DMF and DMSO-*d*6 were also detected. The electrochemical carboxylation of styrene (0.1 M) was conducted on Ni electrode in CO_2 saturated DMF and $TBABF_4$ (0.1 M) electrolyte with j = 10 mA cm^{-2}, charge passed = 20 C, room temperature and 1 atm CO_2 in the presence of (a) 0.025 M (b) 0.05 M and (c) 0.1 M H_2O.

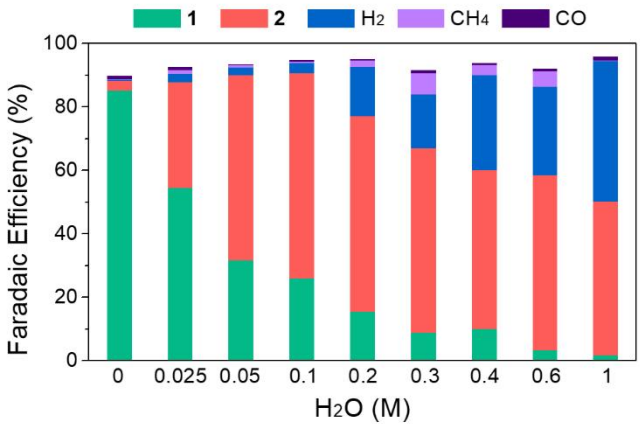

Figure 5.9. Faradaic efficiency (%) of products from electrochemical carboxylation of styrene. Electrolysis was conducted with 0.1 M electrolyte were acidified with HCl (2 M) and extracted with ether for ^{1}H NMR detection (**1** and **2**). The gas products (H_2, CO and CH_4) in the reactor headspace were detected by gas chromatography.

Table 5.1. Product yields from the electrochemical carboxylation of styrene*.

entry	Proton additive (equiv.)	FE of acids (%)†		**1 : 2**	FE of gas products (%)‡		
		1	**2**		H_2	CO	CH_4
1	-	89	3.2	97 : 3	0.5	0.8	0.2
2	H_2O (0.25)	55	33	62 : 38	2.6	0.8	1.3
3	H_2O (0.5)	28	59	35 : 65	2.4	0.1	0.6
4	2 M HCl (0.5)	27	61	31 : 69	2.7	0.3	0.4
5	H_2O (1)	26	65	29 : 71	3.2	0.4	0.4
6	2 M HCl (1)	20	68	23 : 77	4.5	0.3	0.6
7	H_2O (2)	15	61	20 : 80	15	0.3	2.0
8	H_2O (3)	9.5	61	14 : 86	17	0.7	6.7
9	H_2O (4)	11	52	17 : 83	30	0.5	3.2
10	H_2O (6)	3.5	58	6 : 94	28	0.6	4.8
11	H_2O (10)	1.8	47	4 : 96	44	0.9	0.3

*Reaction conditions : Styrene (0.1 M) in DMF and $TBABF_4$ (0.1 M), Ni cathode, Mg anode, j = 10 mA cm^{-2}, charge passed = 20 C, room temperature and P_{CO2} = 1 atm.

†Yields were determined by ^1H NMR after acidification with HCl (2 M) and ether extraction.

‡Yields were determined by gas chromatography after electrolysis.

FE, Faradaic efficiency; **1**, 2-phenylsuccinic acid; **2**, hydrocinnamic acid.

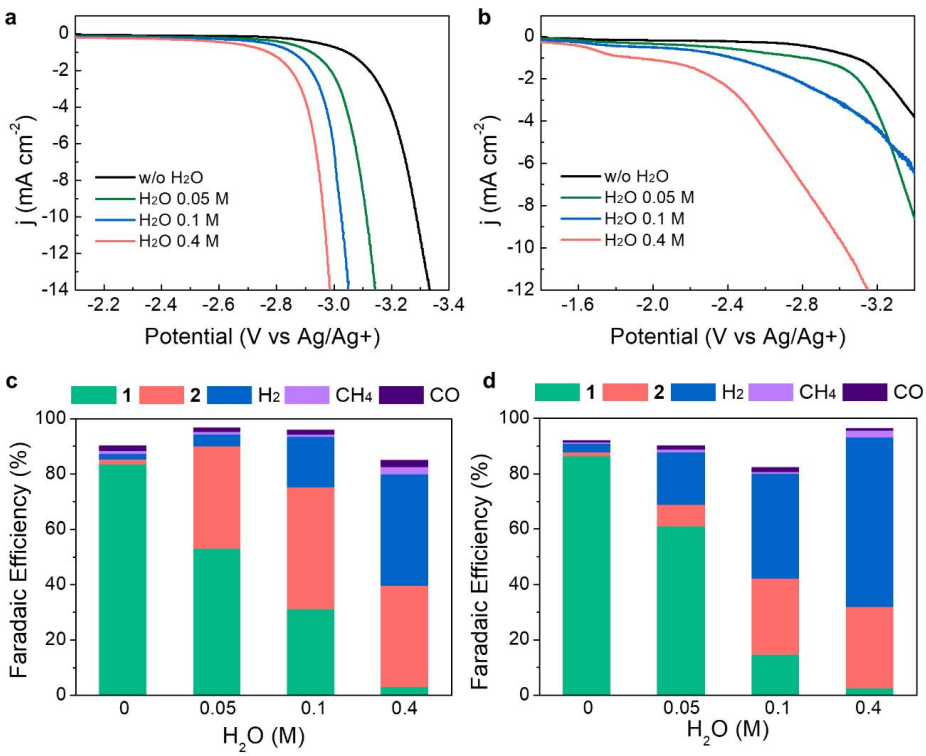

Figure 5.10. Effect of cathode electrodes. The electrochemical measurements and electrolysis were conducted in CO_2-saturated DMF and $TBABF_4$ (0.1 M) electrolyte with various concentrations of H_2O (0 to 0.4 M) at room temperature and 1 atm CO_2. Cathodic linear sweep voltammetry data of 0.1 M styrene at 20 mV s^{-1} on (a) Ti electrode and (b) Pt electrode. Faradaic efficiency (%) of products from electrochemical carboxylation of 0.1 M styrene on (c) Ti electrode and (d) Pt electrode. Electrolysis was conducted with j = 10 mA cm^{-2} and charge passed = 20 C.

Table 5.2. Effect of proton source type on the electrochemical carboxylation of styrene*.

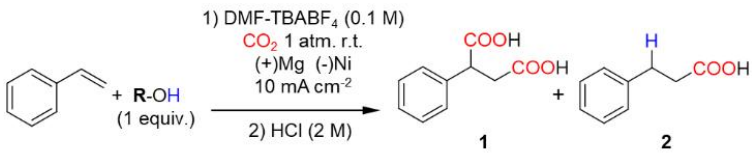

entry	Proton additive (**R-**)	pK_a†	FE of acids (%)‡		**1** : **2**	FE of gas products (%)§		
			1	**2**		H_2	CO	CH_4
1	Acetic acid (CH_3CO-)	12.6 [36]	1	0.3	77 : 23	70	0.9	1.1
2	Phenol (C_6H_5-)	16.47 [37]	40	19	67 : 33	17	1.2	0.2
3	Methanol (CH_3-)	29.0 [38]	68	5	93 : 7	1	0.9	0.1
4	*tert*-Butanol ($(CH_3)_3C$-)	32.2 [38]	53	23	69 : 31	4	0.7	0.4

*Reaction conditions : Styrene (0.1 M) with proton additives (R-OH, 0.1 M) in DMF and $TBABF_4$ (0.1 M), Ni cathode, Mg anode, j = 10 mA cm^{-2}, charge passed = 20 C, room temperature and P_{CO2} = 1 atm.

†pKa values in dimethyl sulfoxide are given based on the referred literature.

‡Yields were determined by ^1H NMR after acidification with HCl (2 M) and ether extraction.

§Yields were determined by gas chromatography after electrolysis.

FE, Faradaic efficiency; **1**, 2-phenylsuccinic acid; **2**, hydrocinnamic acid.

Table 5.3. Influence of current density on electrochemical carboxylation of styrene*.

entry	*j* (mA cm^{-2})	η (mV)	TOF† (s^{-1})	FE of acids (%)‡		**1 : 2**	FE of gas products (%)§		
				1	**2**		H_2	CO	CH_4
1	2	100	0.018	0.3	0.6	31 : 69	37	1.4	0.5
2	5	170	0.85	9	11	46 : 54	36	1	0.3
3	10	220	10	26	65	29 : 71	3	0.4	0.1
4	35	450	34	22	63	26 : 74	5	1.2	0.3
5	50	660	38	19	50	28 : 72	3	0.6	0.2

*Reaction conditions : Styrene (0.1 M) with H_2O (0.1 M) DMF and $TBABF_4$ (0.1 M), Ni cathode, Mg anode, charge passed = 20 C, room temperature and P_{CO2} = 1 atm.

†TOF of *β*-hydrocarboxylation based on the FE of **2**

‡ Yields were determined by ^1H NMR after acidification with HCl (2 M) and ether extraction.

§ Yields were determined by gas chromatography after electrolysis.

TOF, turnover frequency; FE, faradaic efficiency; **1**, 2-phenylsuccinic acid; **2**, hydrocinnamic acid.

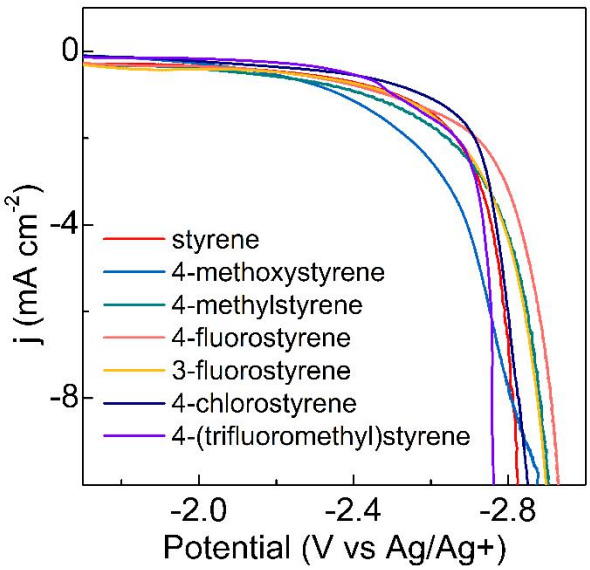

Figure 5.11. Cathodic linear sweep voltammetry data of 0.1 M styrene derivatives with 0.1 M H_2O at 50 mV s^{-1}. The electrochemical carboxylation of styrene derivatives (0.1 M) was conducted on Ni electrode in CO_2 saturated DMF and $TBABF_4$ (0.1 M) electrolyte, room temperature and P_{CO2} = 1 atm in the presence of 0.1 M H_2O.

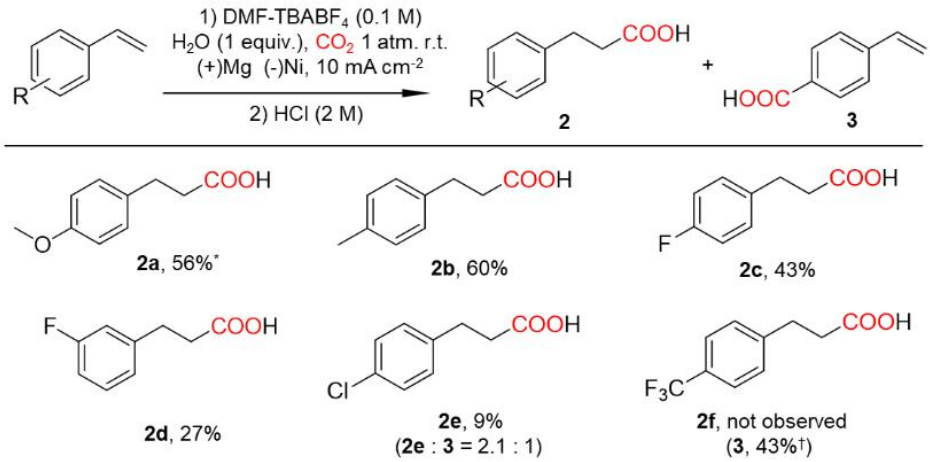

Figure 5.12. Scope of styrene derivatives for electrochemical *β*-hydrocarboxylation. The electrochemical carboxylation of styrene derivatives (0.1 M) was conducted on Ni electrode in CO_2 saturated DMF and $TBABF_4$ (0.1 M) electrolyte with j = 10 mA cm^{-2}, charge passed = 20 C, room temperature and P_{CO2} = 1 atm in the presence of 0.1 M H_2O.

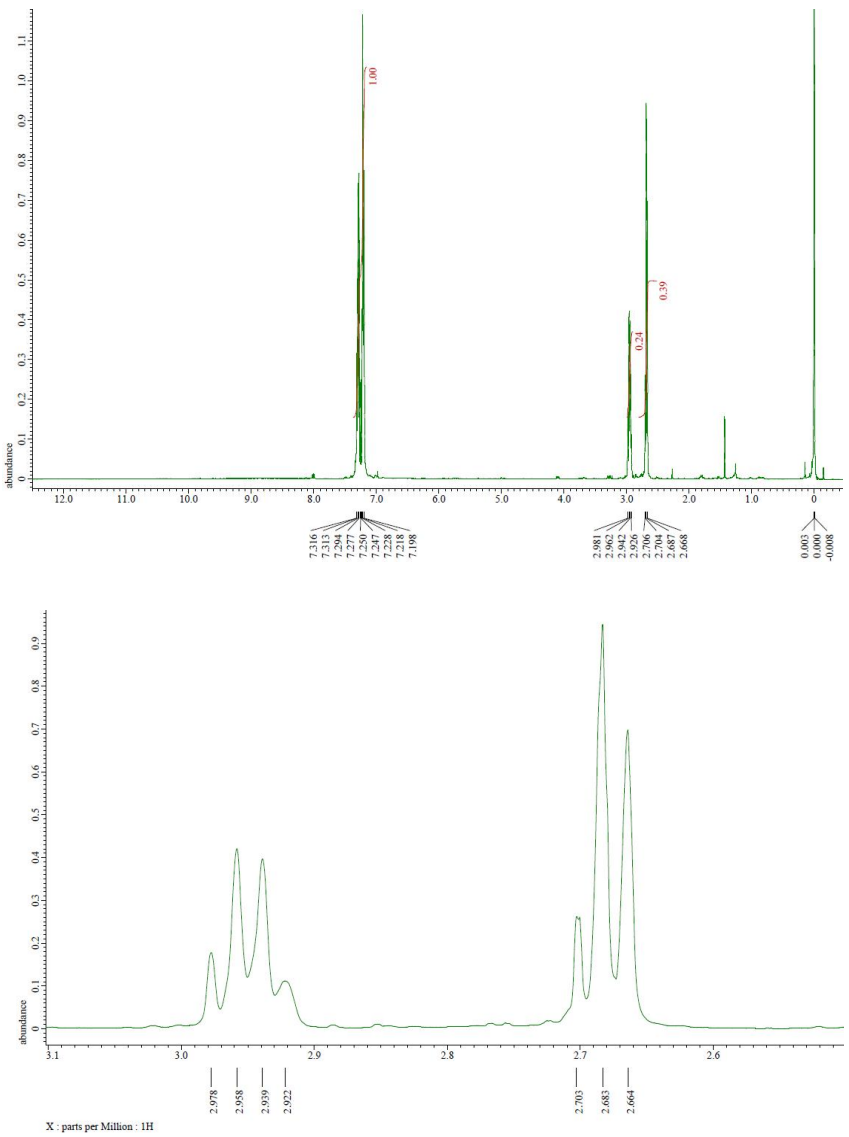

Figure 5.13. NMR results of the deuterium-labeled hydrocinnamic acid (400 MHz, $CDCl_3$).

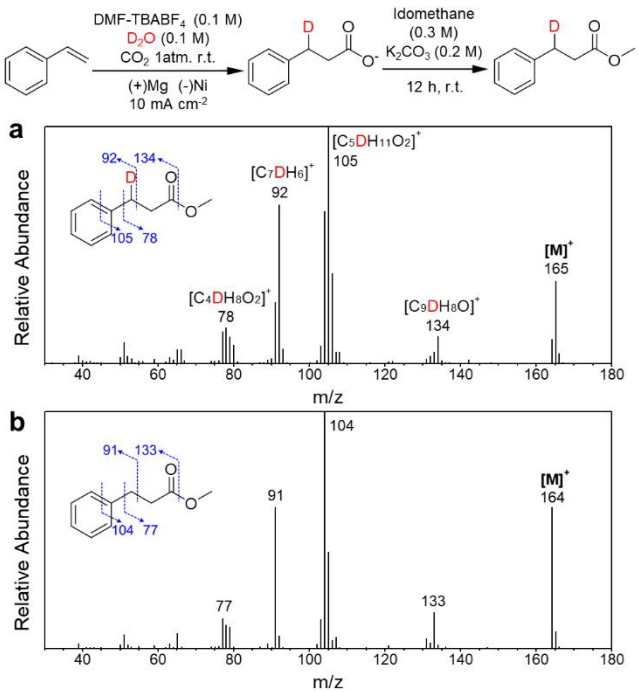

Figure 5.14. Gas chromatography-mass spectrometry (GC-MS) results from deuterium labeling experiments using D_2O. The mass spectra of (a) deuterium labeled methyl-3-phenylpropanoate obtained from the case using D_2O and (b) methyl-3-phenylpropanoate from the case using H_2O are shown. Electrochemical carboxylation of styrene (0.1 M) was conducted on a Ni electrode in CO_2-saturated DMF and $TBABF_4$ (0.1 M) electrolyte with j = 10 mA cm^{-2}, charge passed = 20 C, room temperature and P_{CO2} = 1 atm. The molecular ion peaks ($[M^+]$) of deuterium labeled methyl-3-phenylpropanoate and methyl-3-phenylpropanoate were observed at m/z 165 and 164, respectively.

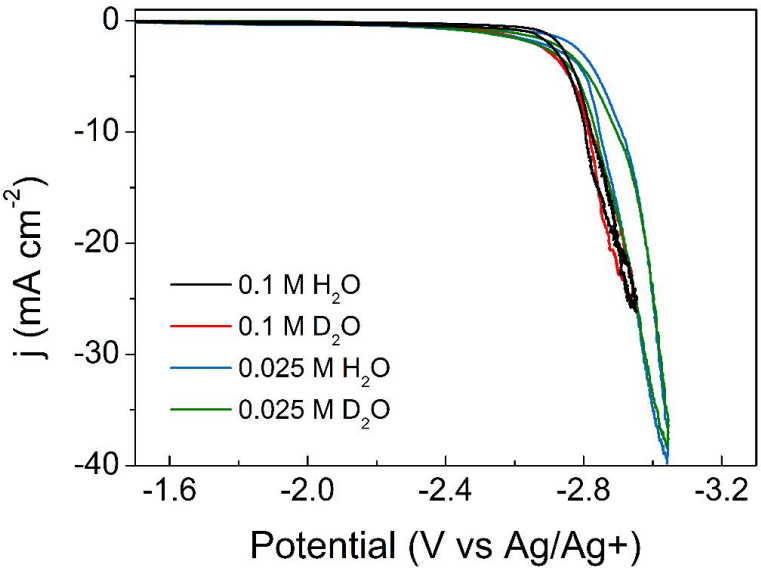

Figure 5.15. Cyclic voltammetry scans of styrene (0.1 M) at 0.1 V s^{-1} with H_2O (0.1 M) / D_2O (0.1 M) / H_2O (0.025 M) / D_2O (0.025 M). The electrolysis was conducted on a Ni electrode in CO_2-saturated DMF and $TBABF_4$ (0.1 M) electrolyte at room temperature and under 1 atm CO_2.

Table 5.4. Effect of deuterium labeled proton source on the product yield of the electrochemical carboxylation of styrene*.

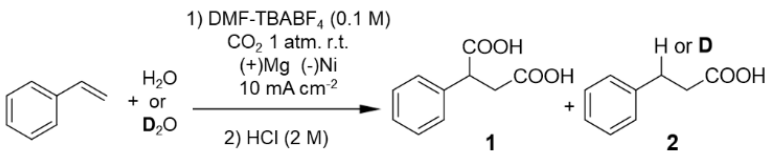

entry	Proton additive (equiv.)	FE of acids (%)†		**1** : **2**	FE of Gas Products (%)‡		
		1	**2**		H_2	CO	CH_4
1	0.025 M H_2O (0.25)	55	33	62 : 38	2.6	0.8	1.3
2	0.025 M $\mathbf{D}_2O$ (0.25)	65	20	76 : 24	3.7	0.8	0.3
3	0.1 M H_2O (1)	26	65	29 : 71	3.2	0.4	0.3
4	0.1 M $\mathbf{D}_2O$ (1)	42	44	49 : 51	4.4	0.9	0.4

*Reaction conditions : Styrene (0.1 M) with proton additives (H_2O or D_2O) in DMF and $TBABF_4$ (0.1 M), Ni cathode, Mg anode, j = 10 mA cm^{-2}, charge passed = 20 C, room temperature and P_{CO2} = 1 atm.

†Yields were determined by ^1H NMR after acidification with HCl (2 M) and ether extraction.

‡Yields were determined by gas chromatography after electrolysis.

equiv., equivalent; FE, Faradaic efficiency; **1**, 2-phenylsuccinic acid; **2**, hydrocinnamic acid.

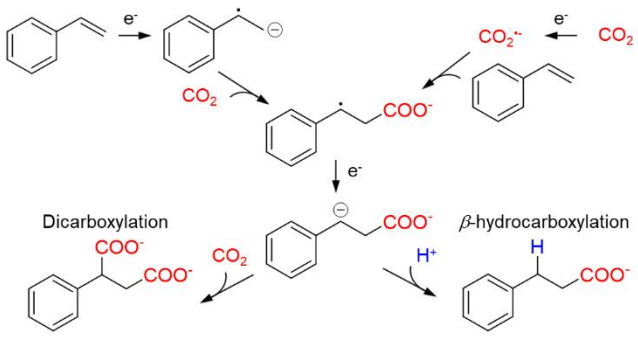

Figure 5.16. Proposed mechanism of the electrochemical carboxylation of styrene.

For the product characterization, we observed each products by using NMR and GC-MS. Reaction conditions were as follows. Electrolysis of reactant styrenes (0.1 M) with water (0.1 M) in 4 mL of CO_2-saturated DMF and $TBABF_4$ (0.1 M) electrolyte was conducted on a Ni cathode-Mg anode for total charge of 20 C at room temperature and under atmospheric pressure of CO_2. Then, reactants were treated with HCl (2 M, aq) for 3 h and extracted with diethyl ether (3 × 20 mL). The organic layer was washed with distilled water and evaporated. The obtained products were re-dissolved in diethyl ether (10 mL) and extracted with of 1 M NaOH (3 × 20 mL). The aqueous solution was washed with diethyl ether, acidified with HCl (2 M, aq) and extracted with diethyl ether (3 × 20 mL). The organic layer was washed with distilled water, dried with $MgSO_4$, and evaporated to give the final product.

The resulted ^{1}H NMR and ^{13}C NMR spectra of 2-Phenylsuccinic acid (**1**), Hydrocinnamic acid (**2**), 3-(4-Methoxyphenyl)propanoic acid (**2a**), 3-(p-Tolyl)propanoic acid (**2b**), 3-(4-Fluorophenyl)propanoic acid (**2c**), 3-(3-Fluorophenyl)propanoic acid (**2d**), 3-(4-Chlorophenyl)propanoic acid (**2e**) and 4-Vinylbenzoic acid (**3**) are shown in **Figure 5.17 – 24**.

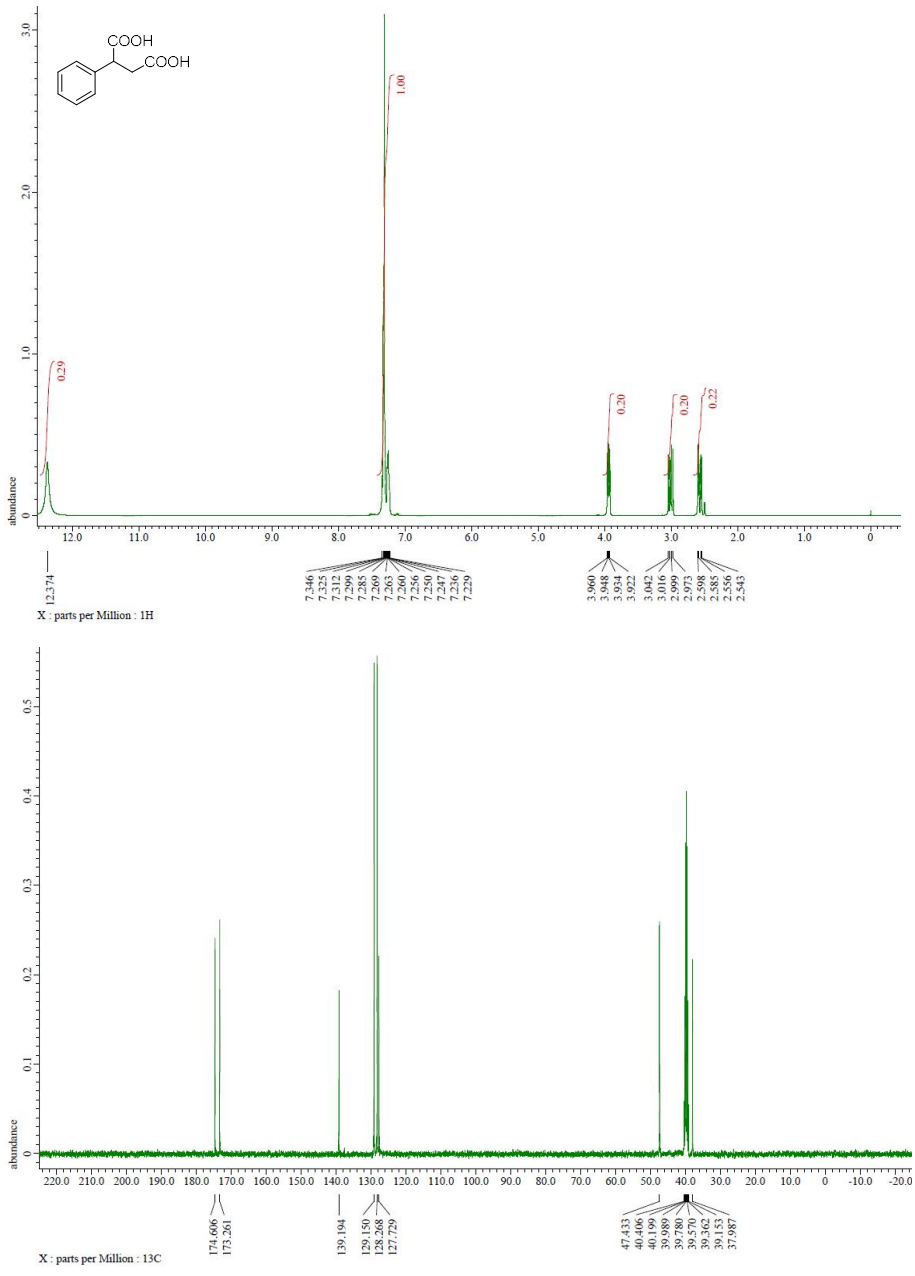

Figure 5.17. NMR spectra of 2-Phenylsuccinic acid.

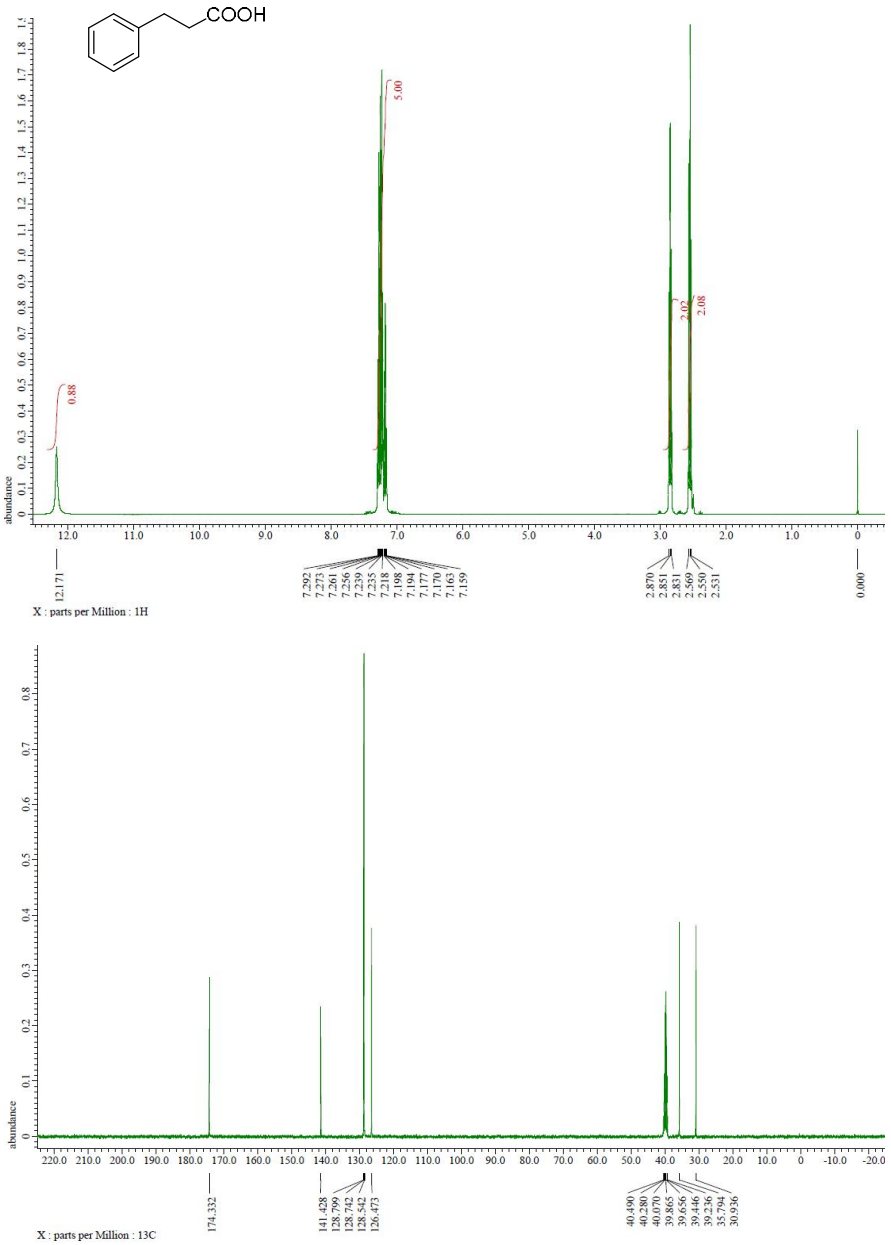

Figure 5.18. NMR spectra of Hydrocinnamic acid.

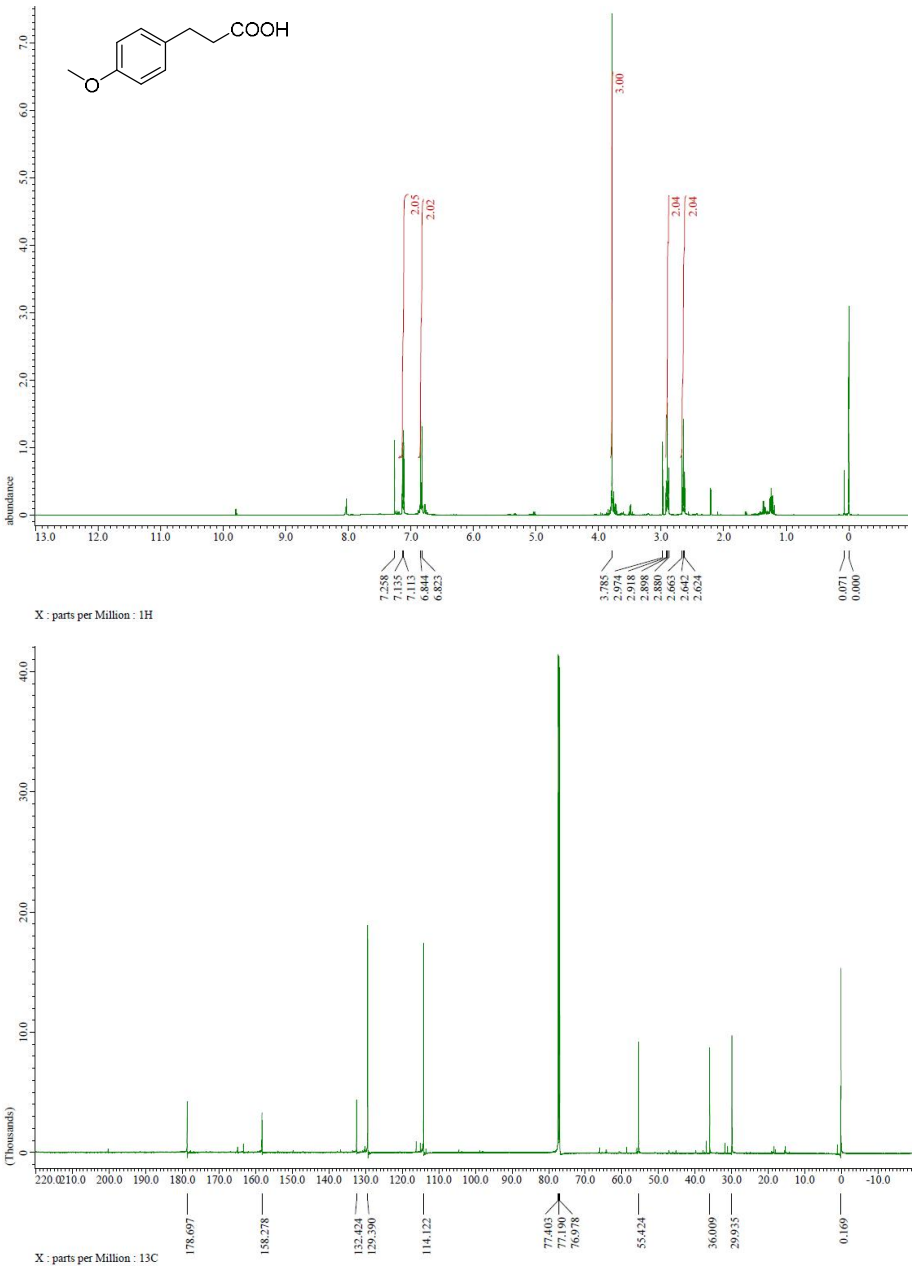

Figure 5.19. NMR spectra of 3-(4-Methoxyphenyl)propanoic acid.

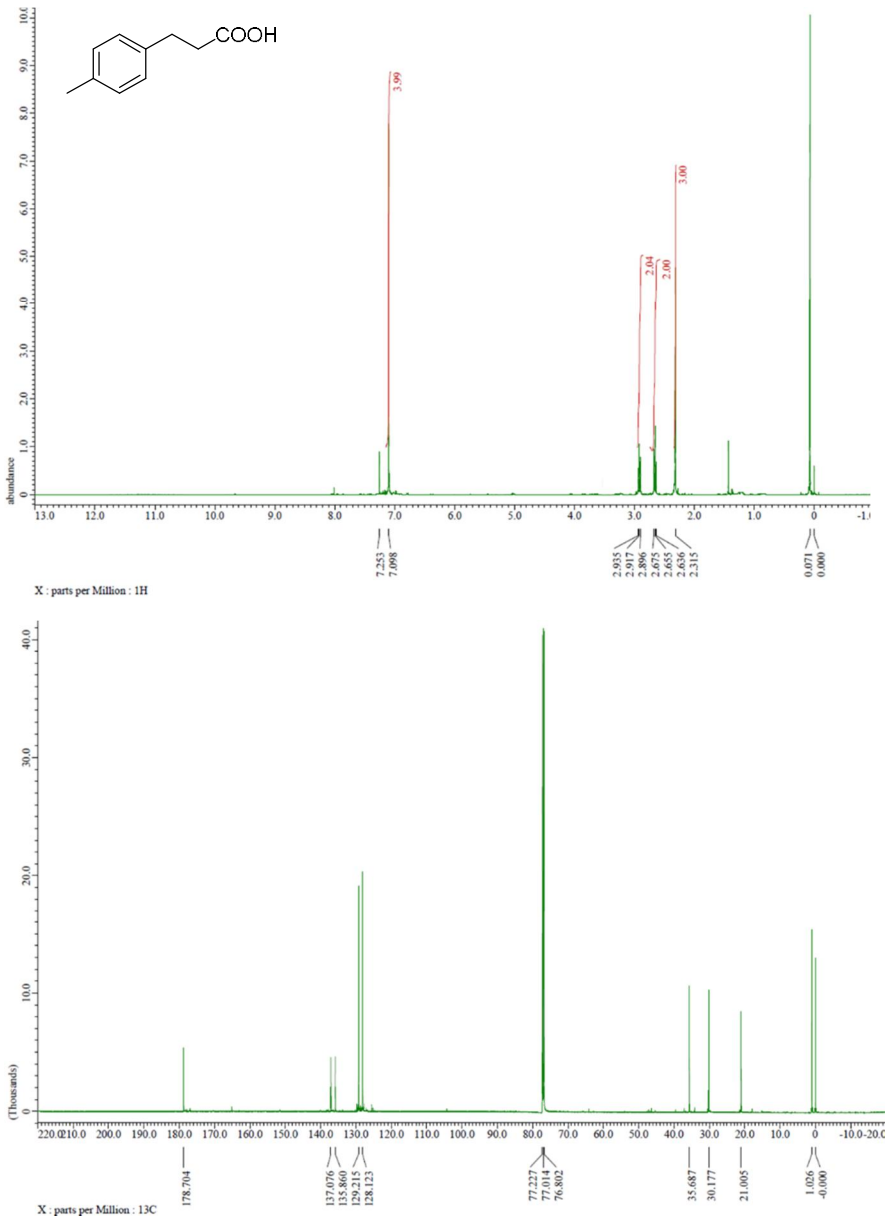

Figure 5.20. NMR spectra of 3-(p-Tolyl)propanoic acid.

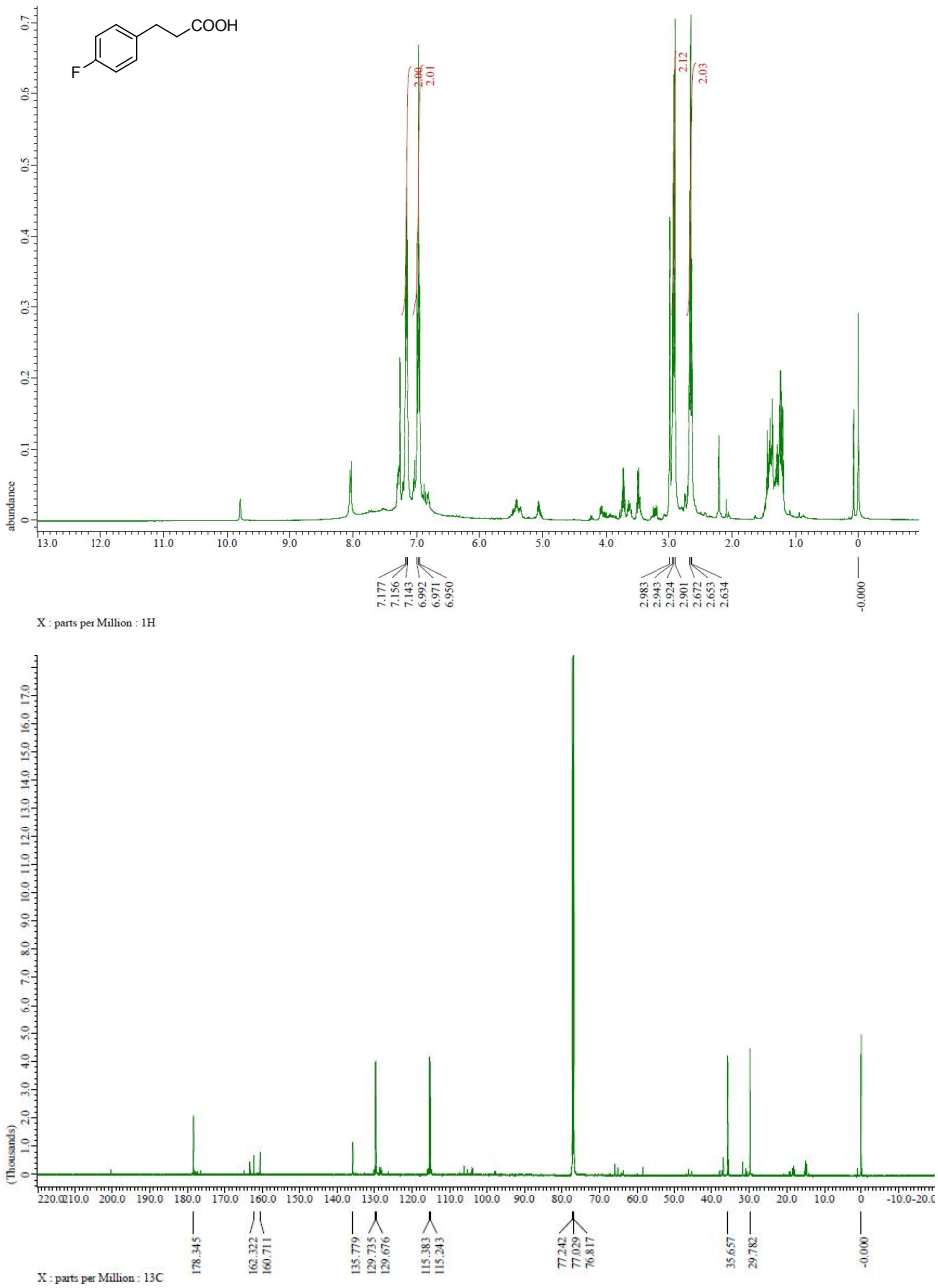

Figure 5.21. NMR spectra of 3-(4-Fluorophenyl)propanoic acid.

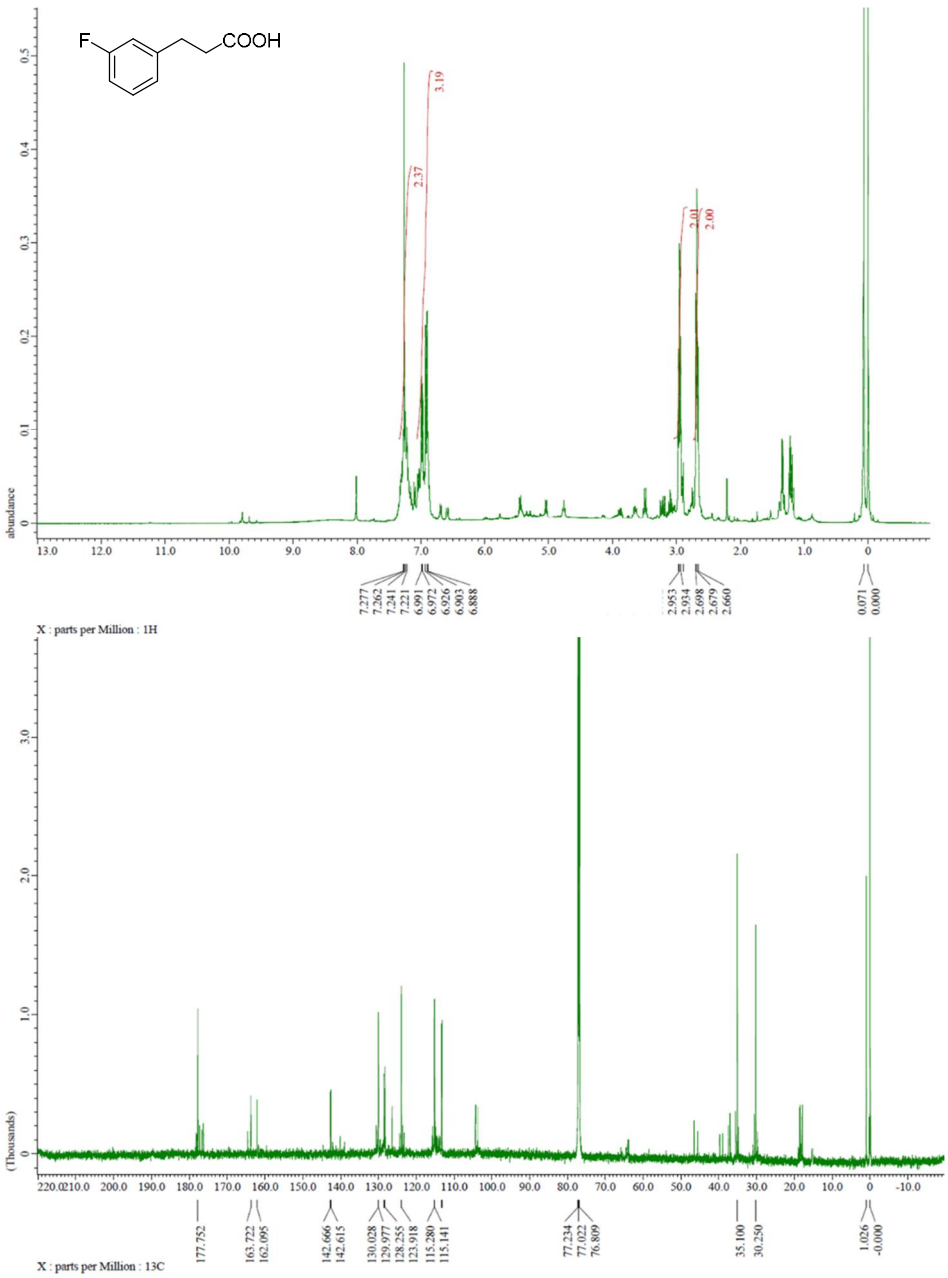

Figure 5.22. NMR spectra of 3-(3-Fluorophenyl)propanoic acid.

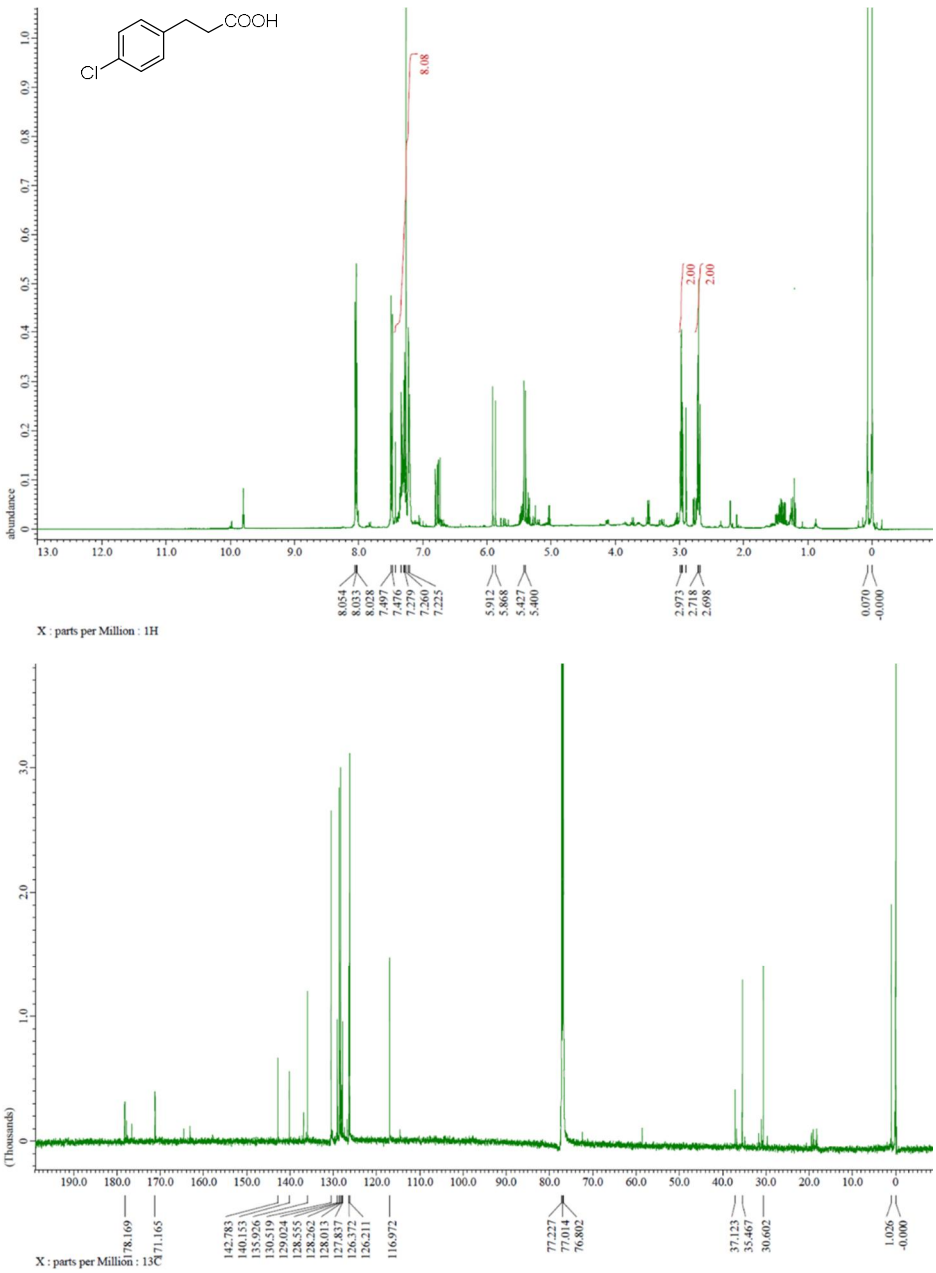

Figure 5.23. NMR spectra of 3-(4-Chlorophenyl)propanoic acid.

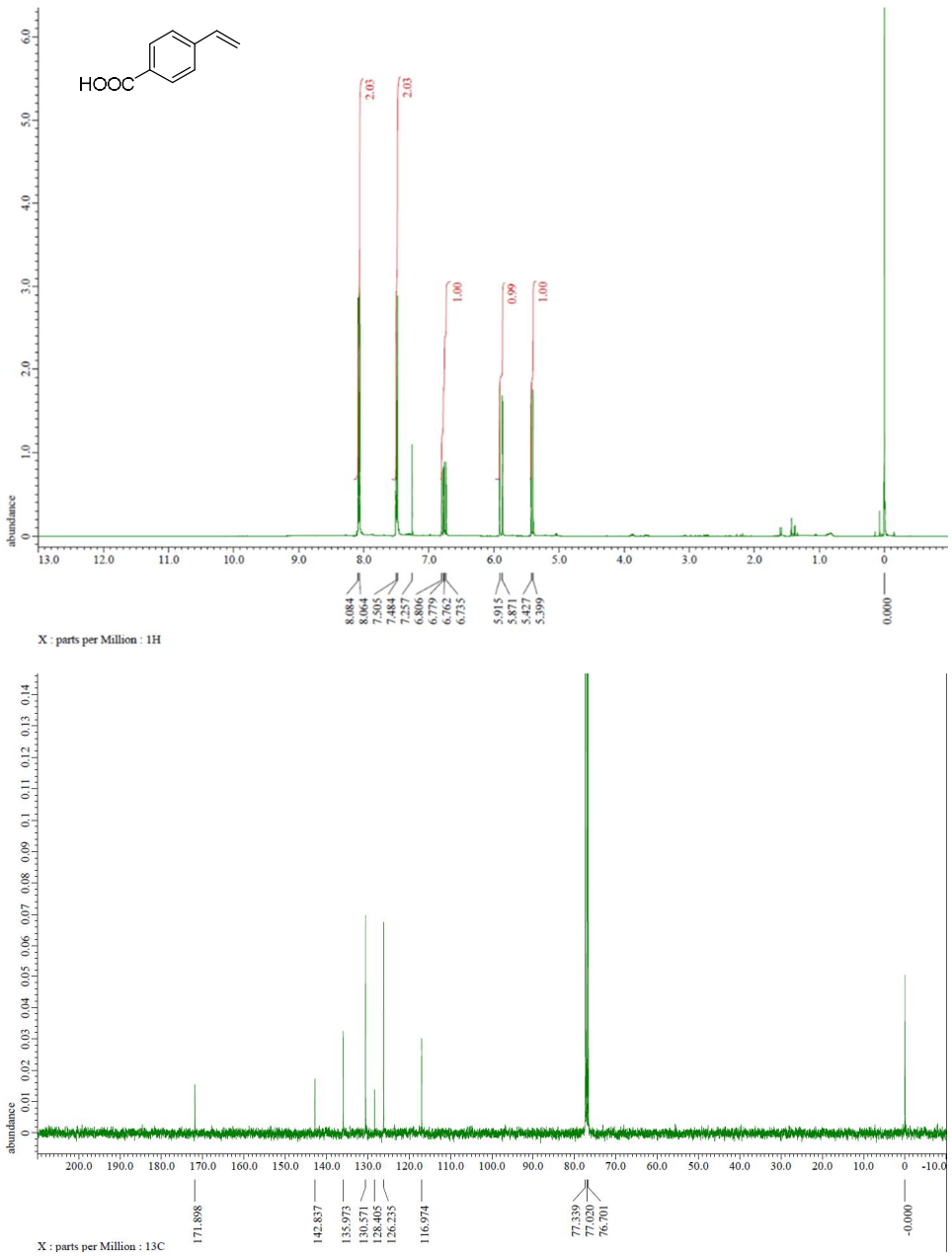

Figure 5.24. NMR spectra of 4-Vinylbenzoic acid.

5.3.2 Electrochemical carboxylation of aliphatic α-olefins

After the successful demonstration of electrochemical carboxylation for styrene, we extended the substrate to aliphatic α-olefins. First, electrochemical carboxylation of aliphatic dienes were conducted. Similar as the case of styrene, previous studies on the electrochemical carboxylation of dienes without proton source reported dicarboxylation as the major pathway. Because the carbon diene bond exists in both substrates, we expected that the carboxylation pathway may be also similar in both cases as illustrated in **Figure 5.25**. Thus, we investigated the effect of water on the product selectivity.

We selected isoprene as the target substrate due to its liquid phase and simple chemical structure. (**Figure 5.26**) As we conducted electrochemical carboxylation on Ni foil in CO_2-saturated DMF and $TBABF_4$ (0.1 M) electrolyte, dicarboxylation mainly occurred by FE of 64%. Then by adding 0.1 M water, the selectivity of hydrocarboxylation towards dicarboxylation increased from 7% to 35%. Basis on the result of styrene, the change of selectivity can also be explained by additional protonation step from water molecule. Furthermore, we also employed Ni foam as an electrode which is expected to have larger surface area. Surprisingly, the foam electrode exhibited enhanced yield of carboxylation for both hydrocarboxylation and dicarboxylation. When Ni foam was used, the total yield of carboxylation in the presence of 0.1 M water enhanced from 55% to 89%, while the selectivity towards hydrocarboxylation slighty reduced from 35% to 28%. The result indicates the foam shape of the electrode facilitates the activation of isoprene which may due to the large surface area that can interact with substrate.

We additionally extended the substrate to general aliphatic α-olefins. In the case of styrene and diene, the substrate can be easily reduced due to the stable radical anion intermediate on the other unsaturated carbon site. However, in the case of α-olefins in the absent of diene structure, the radical anion is comparably unstable.

First, 1-octene was selected as the target substrate. We conducted electrochemical carboxylation in CO_2-saturated DMF and $TBABF_4$ (0.1 M) electrolyte on Ni, Ti and Pt electrodes (**Figure 5.27**). As a result, we observed two main product, non-3-enoic acid and 2-hexylsuccinic acid. These carboxylic acids can be produced through the pathway illustrated in **Figure 5.28**. While 2-hexylsuccinic acid is the product from dicarboxylation that occurred in the case of styrene and diene, reaction pathway for non-3-enoic acid is different from the hydrocarboxylation. During the reaction, alkene bond moved to the adjacent carbon and remained its form without reduction. To accomplish the shift of alkene bond, proton extraction step should be involved during the reaction. In the result of electrode screening, Ti showed the best yield towards the carboxylation while Pt exhibited the lowest yield. We think that the high binding energy of Ti facilitated the proton extraction from 1-octene and resulted in high activity. On the other hand, Pt has the weakest binding energy to proton, which may resulted in low selectivity towards the carboxylation.

We also tested Ni foam electrode to investigate the effect of electrode shape. As a result, we observed increased yield of overall carboxylation reaction, which was also detected in the case of isoprene. This indicates clear effect of foam shape on the increase of carboxylation yield. Furthermore, we observed few

amounts of heptadecenoic acids and heptadecanoic acids in GC-MS analysis which may be produced from the conjugation between 1-octene and non-3-enoic acid. This implies that the tangled structure and large surface area of foam electrode enabled effective binding of hydrocarbon substrates or intermediates on the electrode surface so that can facilitated to undergo carboxylation and even conjugation between hydrocarbons with high yield (**Figure 5.29**). Moreover, on the basis of these results, we think that the reduction reaction of the hydrocarbon substrate on the electrode surface is necessarily required in this electrochemical carboxylation platform.

To further explore the effect of proton source on the carboxylation of 1-octene, we added 0.1 M water. However, the overall yield of carboxylation decreased, especially for the carboxylation towards non-3-enoic acid. This additionally supports the claim that the carboxylation requires proton extraction step rather than proton insertion.

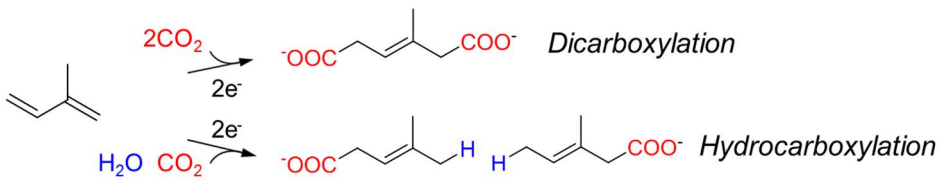

Figure 5.25. Proposed reaction pathway of electrochemical carboxylation of isoprene.

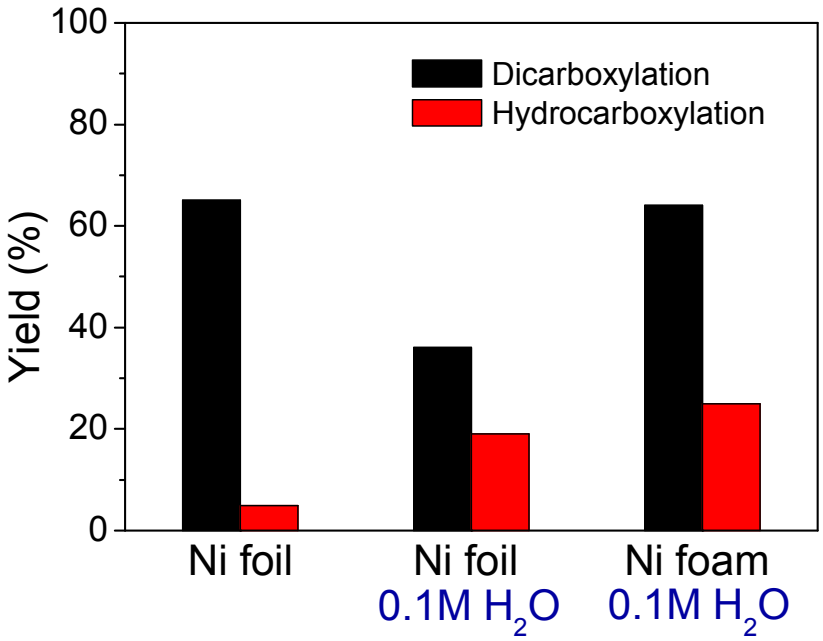

Figure 5.26. Electrochemical carboxylation of isoprene on Ni electrode in CO_2-saturated DMF and $TBABF_4$ (0.1 M) electrolyte.

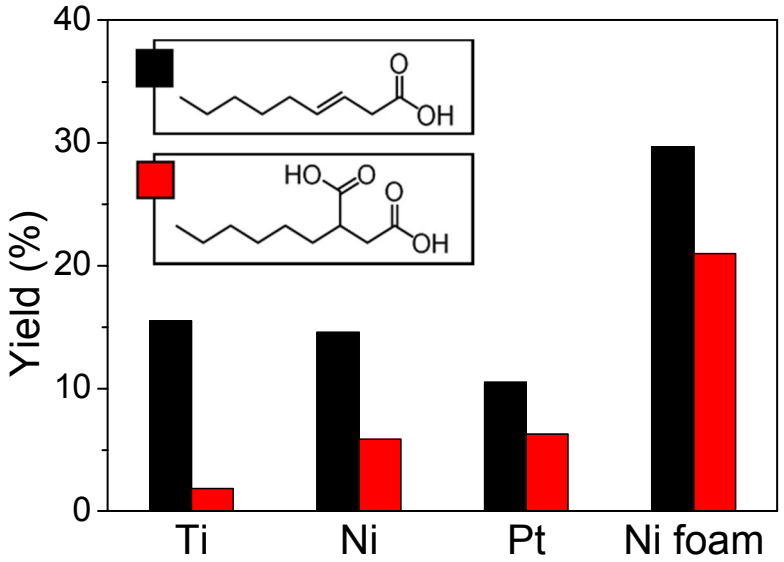

Figure 5.27. Electrochemical carboxylation of 1-octene on Ti, Ni and Pt electrode in CO_2-saturated DMF and $TBABF_4$ (0.1 M) electrolyte.

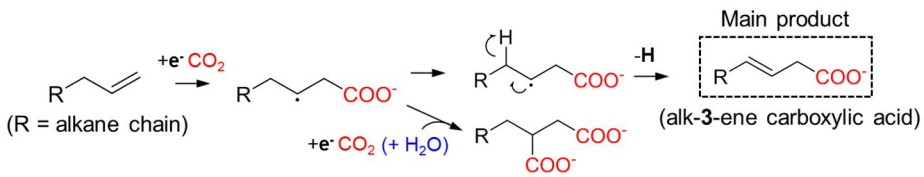

Figure 5.28. Proposed reaction pathway of electrochemical carboxylation of aliphatic α-olefins.

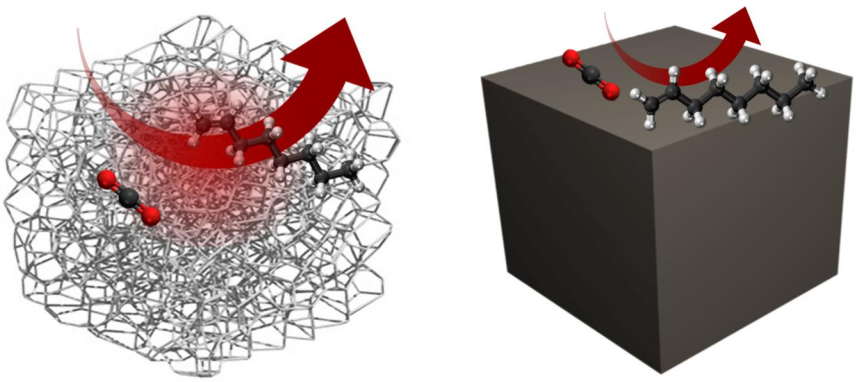

Figure 5.29. The scheme of carboxylation reaction on the foam electrode (left) and foil electrode (right). The foam structure facilitates to bind hydrocarbon substrates more effectively compared to the foil structure.

5.4 Conclusion

In summary, a new electrochemical carboxylation of unsaturated hydrocarbon with CO_2 was demonstrated. First we focused on styrene to build up the electrochemical platform. In the present work, β-hydrocarboxylation of styrene using an electrochemical platform was first demonstrated, and this process exhibited a superior faradaic efficiency of 65% with atmospheric CO_2 and a small amount of water. Solely because of the addition of water, without any other reagents or catalysts, the reaction selectivity of styrene towards this pathway was enhanced up to 96%. Furthermore, from the deuterium labeling experiments, we revealed that a proton from water is directly used in the protonation at the benzylic position of styrene. In this context, we thought that providing a suitable proton source would change the reaction pathway of carboxylation in the desired direction using electrochemical methods.

To precisely explore the pathways of electrochemical reactions, the selectivity of products from styrene carboxylation was investigated under various proton source conditions. Interestingly, we discovered that dicarboxylation, β-hydrocarboxylation and gas production reactions such as hydrogen, carbon monoxide and methane production are carried out competitively depending on the proton source. The major reaction dramatically changed from dicarboxylation to β-hydrocarboxylation as the water concentration increased, and hydrogen production was notably favored over the carboxylation reaction in the presence of excess water. The trend in the change of selectivity also affected by electrode catalysts. Among the used metals, Ni electrode showed the highest selectivity towards β-hydrocarboxylation while Pt electrode exhibited high activity for hydrogen

production instead of carboxylation reaction. In the case of Ni electrode, the maximum yield of β-hydrocarboxylation was observed when we used 1 equivalent of water relative to styrene. In addition to the amount, the type and acidity of proton sources also influenced the control of the reaction selectivity. This result clearly shows a pivotal role of the proton source in tuning the reaction pathway. We revealed that the water molecule is directly consumed as a proton source in β-hydrocarboxylation by deuterium labeling experiments. Moreover, on the basis of the kinetic study, we suggested that the protonation and incorporation of CO_2 on the benzylic position of styrene competitively occurs after the formation of the β-carboxylate intermediate.

We also extended the substrate to aliphatic olefins to apply the electrochemical platform to general hydrocarbons. In the case of dienes, the site selectivity could be controlled between dicarboxylation and hydrocarboxylation by inducing protonation using water. The trend of selectivity change correlates with the case of styrene. While the styrene and aliphatic diene exhibited analogical tendency in the control of selectivity, electrochemical carboxylation of aliphatic α-olefins occurred in different pathway. The major product was alk-3-ene-carboxylic acid where the selectivity enhanced in the absence of proton source. Because the overall reaction requires proton extraction for the intermediate step, electrodes having high binding energy with proton such as Ti electrode exhibited excellent yield for the carboxylation reaction.

We believe this study provides valuable strategies for achieving controllable selectivity in heterogeneously catalyzed electrochemical reactions and provides opportunities to use this platform in a wide range of organic syntheses.

Furthermore, we envision that this method can be used in hybridizing the electrochemical reduction of CO_2 and carbon fixation to long-chain hydrocarbons as photosynthetic carbon cycle.[40, 41]

Reference

1. Bassham, J. A. *et al*. The Path of Carbon in Photosynthesis. 21. The Cyclic Regeneration of Carbon Dioxide Acceptor. *J. Am. Chem. Soc.* **76**, 1760-1770 (1954).

2. Lorimer, G. H. The Carboxylation and Oxygenation of Ribulose 1,5-Bisphosphate - the Primary Events in Photosynthesis and Photo-Respiration. *Annu. Rev. Plant Phys.* **32**, 349-383 (1981).

3. Li, S., Yuan, W. & Ma, S. Highly Regio- and Stereoselective Three-Component Nickel-Catalyzed syn-Hydrocarboxylation of Alkynes with Diethyl Zinc and Carbon Dioxide. *Angew. Chem. Int. Ed.* **50**, 2578-2582 (2011).

4. Fujihara, T., Xu, T., Semba, K., Terao, J. & Tsuji, Y. Copper-Catalyzed Hydrocarboxylation of Alkynes Using Carbon Dioxide and Hydrosilanes. *Angew. Chem. Int. Ed.* **50**, 523-527 (2011).

5. Wang, X. Q., Nakajima, M. & Martin, R. Ni-Catalyzed Regioselective Hydrocarboxylation of Alkynes with CO_2 by Using Simple Alcohols as Proton Sources. *J. Am. Chem. Soc.* **137**, 8924-8927 (2015).

6. Yu, B., Xie, J. N., Zhong, C. L., Li, W. & He, L. N. Copper(I)@Carbon-Catalyzed Carboxylation of Terminal Alkynes with CO_2 at Atmospheric Pressure. *Acs Catal.* **5**, 3940-3944 (2015).

7. Tanaka, S., Watanabe, K., Tanaka, Y. & Hattori, T. EtAICI(2)/2,6-Disubstituted Pyridine-Mediated Carboxylation of Alkenes with Carbon Dioxide. *Org. Lett.* **18**, 2576-2579 (2016).

8. Huguet, N. *et al*. Nickel-Catalyzed Direct Carboxylation of Olefins with CO2: One-Pot Synthesis of alpha,beta-Unsaturated Carboxylic Acid Salts. *Chem. Eur. J.* **20**, 16858-16862 (2014).

9. Ostapowicz, T. G., Schmitz, M., Krystof, M., Klankermayer, J. & Leitner, W. Carbon Dioxide as a C-1 Building Block for the Formation of Carboxylic Acids by Formal Catalytic Hydrocarboxylation. *Angew. Chem. Int. Ed.* **52**, 12119-12123 (2013).

10. Wu, L., Liu, Q., Fleischer, I., Jackstell, R. & Beller, M. Ruthenium-catalysed alkoxycarbonylation of alkenes with carbon dioxide. *Nat. Commun.* **5** (2014).

11. Ishida, N., Masuda, Y., Uemoto, S. & Murakami, M. A Light/Ketone/Copper System for Carboxylation of Allylic C-H Bonds of Alkenes with CO_2. *Chem. Eur. J.* **22**, 6524-6527 (2016).

12. Juliá-Hernández, F., Moragas, T., Cornella, J. & Martin, R. Remote carboxylation of halogenated aliphatic hydrocarbons with carbon dioxide. *Nature* **545**, 84-88 (2017).

13. Liu, Q., Wu, L., Jackstell, R. & Beller, M. Using carbon dioxide as a building block in organic synthesis. *Nat. Commun.* **6** (2015).

14. Luan, Y. X. & Ye, M. Transition metal-mediated or catalyzed

hydrocarboxylation of olefins with CO_2. *Tetrahedron Lett.* **59**, 853-861 (2018).

15. Zhang, Y. & Riduan, S.N. Catalytic Hydrocarboxylation of Alkenes and Alkynes with CO_2. *Angew. Chem. Int. Ed.* **50**, 6210-6212 (2011).

16. Kirillov, E., Carpentier, J. F. & Bunel, E. Carboxylic acid derivatives via catalytic carboxylation of unsaturated hydrocarbons: whether the nature of a reductant may determine the mechanism of CO_2 incorporation? *Dalton Trans.* **44**, 16212-16223 (2015).

17. Gaydou, M., Moragas, T., Juliá-Hernández, F. & Martin, R. Site-Selective Catalytic Carboxylation of Unsaturated Hydrocarbons with CO_2 and Water. *J. Am. Chem. Soc.* **139**, 12161-12164 (2017).

18. Matthessen, R., Fransaer, J., Binnemans, K. & De Vos, D. E. Electrocarboxylation: towards sustainable and efficient synthesis of valuable carboxylic acids. *Beilstein J. Org. Chem.* **10**, 2484-2500 (2014).

19. Senboku, H. & Katayama, A. Electrochemical carboxylation with carbon dioxide. *Curr. Opin. Green Sustain. Chem.* **3**, 50-54 (2017).

20. Silvestri, G., Gambino, S. & Filardo, G. Use of Sacrificial Anodes in Synthetic Electrochemistry - Processes Involving Carbon-Dioxide. *Acta Chem. Scand.* **45**, 987-992 (1991).

21. Filardo, G., Gambino, S., Silvestri, G., Gennaro, A. & Vianello, E. Electrocarboxylation of Styrene through Homogeneous Redox Catalysis. *J. Electroanal. Chem.* **177**, 303-309 (1984).

22. Dérien, S., Clinet, J. C., Dunach, E. & Perichon, J. Electrochemical Incorporation of Carbon-Dioxide into Alkenes by Nickel-Complexes. *Tetrahedron* **48**, 5235-5248 (1992).

23. Ballivet-Tkatchenko, D., Folest, J. C. & Tanji, J. Electrocatalytic reduction of CO_2 for the selective carboxylation of olefins. *Appl. Organomet. Chem.* **14**, 847-849 (2000).

24. Senboku, H., Komatsu, H., Fujimura, Y. & Tokuda, M. Efficient electrochemical dicarboxylation of phenyl-substituted alkenes: Synthesis of 1-phenylalkane-1,2-dicarboxylic acids. *Synlett*, 418-420 (2001).

25. Wang, H., Lin, M. Y., Fang, H. J., Chen, T. T. & Lu, J. X. Electrochemical dicarboxylation of styrene: Synthesis of 2-phenylsuccinic acid. *Chinese J. Chem.* **25**, 913-916 (2007).

26. Yuan, G. Q., Jiang, H. F., Lin, C. & Liao, S. J. Efficient electrochemical synthesis of 2-arylsuccinic acids from CO(2) and aryl-substituted alkenes with nickel as the cathode. *Electrochim. Acta* **53**, 2170-2176 (2008).

27. Yatham, V. R., Shen, Y. & Martin, R. Catalytic Intermolecular Dicarbofunctionalization of Styrenes with CO_2 and Radical Precursors. *Angew. Chem. Int. Ed.* **56**, 10915-10919 (2017).

28. Seo, H., Liu, A. & Jamison, T. F. Direct beta-Selective Hydrocarboxylation of Styrenes with CO_2 Enabled by Continuous Flow Photoredox Catalysis. *J. Am. Chem. Soc.* **139**, 13969-13972 (2017).

29. Williams, C. M., Johnson, J. B. & Rovis, T. Nickel-Catalyzed Reductive

Carboxylation of Styrenes Using CO_2. *J. Am. Chem. Soc.* **130**, 14936-14937 (2008).

30. Greenhalgh, M. D. & Thomas, S. P. Iron-Catalyzed, Highly Regioselective Synthesis of alpha-Aryl Carboxylic Acids from Styrene Derivatives and CO_2. *J. Am. Chem. Soc.* **134**, 11900-11903 (2012).

31. Shao, P., Wang, S., Chen, C. & Xi, C. Cp_2TiCl_2-Catalyzed Regioselective Hydrocarboxylation of Alkenes with CO_2. *Org. Lett.* **18**, 2050-2053 (2016).

32. Meng, Q. Y., Wang, S., Huff, G. S. & König, B. Ligand-Controlled Regioselective Hydrocarboxylation of Styrenes with CO_2 by Combining Visible Light and Nickel Catalysis. *J. Am. Chem. Soc.* **140**, 3198-3201 (2018).

33. Aghmiz, A., Giménez-Pedrós, M., Masdeu-Bultó, A. M. & Schmidtchen, F. P. Hydrocarboxylation of styrene in aqueous media with Pd-guanidinumphosphine systems. *Catal. Lett.* **103**, 191-193 (2005).

34. Kawashima, S., Aikawa, K. & Mikami, K. Rhodium-Catalyzed Hydrocarboxylation of Olefins with Carbon Dioxide. *Eur. J. Org. Chem.*, 3166-3170 (2016).

35. Chen, Y., Li, C. W. & Kanan, M. W. Aqueous CO_2 Reduction at Very Low Overpotential on Oxide-Derived Au Nanoparticles. *J. Am. Chem. Soc.* **134**, 19969-19972 (2012).

36. Bordwell, F. G. & Algrim, D. Nitrogen Acids. 1. Carboxamides and Sulfonamides *J. Org. Chem.* **41**, 2507-2508 (1976).

37. Roy, K. & Popelier, P. L. A. Predictive QSPR modeling of the acidic dissociation constant (pK_a) of phenols in different solvents *J. Phys. Org. Chem.* **22**, 186-196 (2009).

38. Olmstead, W. N., Margolin, Z. & Bordwell, F. G. Acidities of Water and Simple Alcohols in Dimethyl Sulfoxide Solution *J. Org. Chem.* **45**, 3295-3299 (1980).

39. Sim, B.A., Milne, P.H., Griller, D. & Wayner, D.D.M. Thermodynamic significance of .rho.+ and .rho.- from substituent effects on the redox potentials of arylmethyl radicals. *J. Am. Chem. Soc.* **112**, 6635-6638 (1990).

40. Yang, K.D., Lee, C.W., Jin, K., Im, S.W. & Nam, K.T. Current Status and Bioinspired Perspective of Electrochemical Conversion of CO_2 to a Long-Chain Hydrocarbon. *J. Phys. Chem. Lett.* **8**, 538-545 (2017).

41. Kim, Y., Lee, J.H., Ha, H., Im, S.W. & Nam, K.T. Material science lesson from the biological photosystem. *Nano Convergence* **3**, 19 (2016).

Chapter 6. Concluding remarks

In this thesis, we developed new energy harvesting and conversion pathway for sustainable carbon cycle. The fundamental design of system was inspired by natural photosynthesis, which is the only existing natural carbon storage pathway from the atmosphere to the ground. Through the natural pathway, gaseous CO_2 and water molecules are converted into hydrocarbon fuel where the reaction is mainly driven by solar light. We developed three artificial energy conversion systems inspired from the discrete process during the natural photosynthesis: light harvesting complex, hybrid Z-scheme and electrochemical carboxylation platform.

The initial step of photosynthesis occurs by harvesting solar light. Here, photosystem proteins absorb the light and transfer the energy to the reaction center. Thus, the elaborate construction of light harvesting complex of photosystem determines the light absorption and energy transfer ability. Inspired from the structure of photosystem protein where the chlorophyll dye molecules are aligned on the peptide backbone, new artificial light harvesting complex was developed. First, the porphyrin molecules were conjugated on synthetic peptoid scaffold with precisely controlled intermolecular distance. Then, the dyes were additionally decorated on the gold nanoparticle template to be stably fixed on support and suppress the aggregation among dyes. The gold nanoparticle template also facilitate to analyze the energy transfer ability between dyes by amplifying the fluorescence of dyes due to the plasmon effect. This enabled to enhance both excitation and

emission of light harvesting complex and to directly measure the intramolecular light-energy interaction. Consequently, we succeeded to observe efficient energy transfer between porphyrin dyes aligned by 6Å, which is in the same range of intermolecular chlorophyll distance in photosystem protein.

Followed by light harvesting, electron transfer via Z-scheme takes place crossing over photosystem proteins. In detail, the collected light energy consumed in the electron excitation at the reaction center and the produced electron-hole pair respectively participate in NADP reduction and water oxidation reactions. The natural Z-scheme is composed of two photosystem proteins, PSI and PSII. The sequential excitation of electron through two photosystem enables to excite electron to high energy by using only visible light. To apply this Z-schematic pathway in the production of hydrogen, new hybrid Z-scheme between PSI and semiconductor $BiVO_4$ were constructed. Metal particle such as Au and Ag were introduced to physically integrate protein and semiconductor part and facilitate the electron transfer between them. Each materials were selected based on the optimal energy level for the oxidation and reduction reaction. As a result, hydrogen was produced from water in our hybrid Z-scheme without any redox chemical under visible light. Our hybrid Z-scheme exhibited 5 times higher hydrogen evolution efficiency compared to the previous hydrogen evolution system that used PSI and chemical reductant. Furthermore, the photo-reaction stably maintained its high efficiency over 72 h although the degradation of photo-activity of PSI is often reported. We believe that these exceeding activity and stability is resulted from the hybridized structure between the protein and semiconductor.

The final goal of photosynthesis is to produce valuable hydrocarbon fuel.

This reaction is mainly driven by electrochemical power obtained from the light reaction and CO_2 as a one-carbon building block. In the analogous manner, we demonstrated electrochemical carboxylation of unsaturated hydrocarbons using CO_2 and water. The idea of CO_2 insertion into unsaturated carbon bond of substrate was inspired from the carbon fixation process in Calvin cycle of dark reaction. In one circulation, one CO_2 molecule binds to enediolate intermediate via carboxylation and form carboxylic acid group to add carbon to the substrate. This carboxylation reaction using CO_2 has been also adopted in organic synthesis to make carboxylate and carboxylic acid products from hydrocarbon feedstocks. Previously, electrochemical carboxylation platform has received less attention than homogeneously catalyzed system due to the lack of strategy to control the site-selectivity of the reaction. In this study, we firstly introduced water as proton source in the electrochemical reaction to induce new protonation pathway. As a result, we virtually observed shift of site-selectivity of styrene carboxylation from dicarboxylation to β-hydrocarbonxylation. The overall carboxylation resembles the natural carbon fixation in Calvin cycle which also uses water and CO_2 as proton and carbon source for the production of glucose. We discovered that the water molecule is used as proton source during the protonation process in β-hydrocarbonxylation by using deuterium exchange experiment. On the basis of the successful demonstration of electrochemical carboxylation platform using styrene, we extended the substrate to aliphatic α-olefins. In the case of diene, the change of reaction pathway was changed from dicarboxylation to hydrocarboxylation by adding water which is similar trend with the case of styrene. However, α-olefins without diene bond exhibited different carboxylation pathway where alk-3-enoic

acids were mainly produced. Furthermore, we investigated the effect of electrode structure by using foam electrode instead of foil electrode. As a result, higher yield towards carboxylation was observed on foam electrode. This indicates that the tangled structure and large surface area of the foam structure can enable to bind hydrocarbons on the surface strongly so that can undergo further reaction effectively for long-hydrocarbons. We envision that this work will aid to practically use electrochemical platform in carboxylation reaction to produce valuable long-hydrocarbon fuels.

In conclusion, we demonstrated energy harvesting and conversion pathway from solar energy to hydrocarbon fuel. The demonstrated artificial systems were respectively inspired from the sequential energy conversion steps in natural photosynthesis. We envision that new sustainable carbon cycle can be finally realized by integrating the light-catalytic part and electrochemical CO_2 conversion part into one successive system.

국문 초록

자연계의 모든 자유에너지들은 태양에너지로부터 얻어지며 이는 광합성을 통해 흡수된다. 매년 4.2×10^{17} kJ 의 에너지가 광합성을 통해 흡수되며 이는 물과 이산화탄소를 산소와 포도당으로 전환하는데 사용된다. 이러한 과정을 통해 대기중의 이산화탄소는 지상에서 탄소화합물을 형성하는 구성 요소로 사용되며, 이로 인해 지구상의 탄소 순환이 그 균형을 유지할 수 있다. 그러나 인류의 산업 시대 이후 무분별한 화석 연료의 사용은 대기 중으로 과량의 탄소를 배출시켰으며 이는 지구 탄소 순환을 깨뜨리는 결과를 야기하였다. 따라서 이를 해소하기 위해서는 새로운 인공적인 탄소 고정 경로가 개발되어야 한다. 본 학위 연구에서는 자연계의 광합성을 모델로 한 인공 에너지 전환 시스템을 개발하였다. 각각의 시스템은 광합성에서 연속적으로 일어나는 에너지 전환 과정들, 빛 에너지의 흡수 / 전자 전달 / 탄소의 고정, 을 모사하였다.

자연계가 이미 정교한 디자인과 훌륭한 기능들을 보유하고 있음에도 불구하고, 이를 인공 장치에 적용하기 위해서는 개선이 필요하다. 먼저 단백질과 같이 안정성이 떨어지는 생체 재료들을 보완하기 위해 안정한 합성 물질들을 추가적인 지지체 혹은 대체제로 사용해야 한다. 또한 광합성 반응에 의해 생성된 에너지 혹은 연료는

유기물의 신진대사가 아닌 엔진을 작동시키는데 사용될 수 있어야 한다. 본 학위 연구에서는 이들을 해결하기 위한 새로운 전략을 세우기 위해 먼저 인공광합성 개발에 대한 선행 연구들을 조사하였다. Chapter 2 에서는 지금까지 연구되었던 인공적인 광합성 시스템들인 인공 집광복합체 개발, 인공 전자전달계 개발, 전기화학적 이산화탄소 고정에 대해 다루었다. 선행 연구들로부터 얻은 교훈을 발판 삼아 본 학위 연구에서는 유용한 연료 개발을 위한 세 가지의 에너지 전환 경로를 개발하였다.

광합성은 광활성 단백질인 광계가 태양빛을 흡수하며 그 반응이 개시된다. 광계는 집광복합체와 반응중심체로 그 구조가 이루어지며, 집광복합체는 태양빛을 흡수하고 흡수된 광 에너지를 반응중심체로 전달하는 역할을 수행한다. 이때, 색소 분자들의 효율적인 배열이 전체 집광복합체의 광-흡수, 광-에너지 전달 특성을 좌우하게 된다. 본 학위 연구에서는 이러한 광계 내의 정교한 색소 분자 배열을 모사하여 포르피린 색소 분자를 기반으로 하고 금 나노입자를 지지체로 사용한 인공 집광복합체를 개발하였다. 이때 색소 분자들 간의 배열을 정밀하게 조절하기 위해 펩토이드를 사용하여 나노 입자의 가지 지지체로 사용하였다. 포르피린 분자들 간의 거리는 6 Å 에서 12 Å 으로 조절하였으며 이는 실제 광계 단백질에서 엽록소 분자들이 배열되어 있는 거리와 같은 범위이다. 더불어 금 나노입자의 플라즈몬 효과로 인해 색소 분자의 형광을 증폭시킬 수 있다. 그 결과, 색소의 형광

신호가 최대 20배까지 증가하였으며 이로써 집광복합체의 광특성을 더욱 정밀하게 분석할 수 있었다. 구체적으로, 서로 다른 색소 분자의 배열로부터 구분되는 형광 스펙트럼이 얻어졌다. 이는 본 연구에서 개발된 집광복합체가 색소 집합체의 분자간 에너지 전달 특성을 조사할 수 있는 플랫폼으로 사용될 수 있음을 보여준다.

빛 흡수에 의해 모아진 광-에너지는 반응 중심체에서 전자를 여기시키는 과정에 사용된다. 여기된 전자는 두 개의 광계로 이루어진 Z-체계의 전자전달계로 전달되어 광계II 에서의 물 산화반응과 광계I 에서의 NADP 환원 반응에 참여한다. 두 번의 연속적인 전자 여기를 통해 전체 산화 환원 과정은 가시광선-적외선 영역의 작은 에너지만을 이용해 이루어진다. 인공적인 Z-체계에서는 광계를 대신하여 광활성 반응체의 역할을 대체할 수 있는 반도체 물질을 사용한다. 반도체 물질은 구현하고자 하는 산화 환원 반응과 최적 전자 전달 효율을 달성할 수 있는 에너지 준위를 고려하여 선정되고 제작된다. 본 학위 연구에서는 광계I 과 반도체 물질을 결합한 새로운 하이브리드 Z-체계를 개발하였다. 본 시스템에서는 광계I과 반도체가 금 또는 은 금속 중간체 물질로 직접 연결되어 합쳐진 구조를 이루고 있으며, 가시광선 영역의 빛을 받아 물로부터 수소를 생산한다. 이때 수소 발생 반응의 효율과 안정성은 광계I을 화학 환원제를 사용하여 수소를 생산한 경우에 비하여 모두 증가하였다. 이러한 뛰어난 활성은 안정한 반도체 물질과 단백질의 하이브리드 구조에서 기인한 것으로 보여진다.

자연계의 광합성에서는 광반응으로부터 생산된 전기화학 에너지를 이용하여 최종적으로 이산화탄소로부터 포도당을 합성한다. 인공적인 전기화학 장치에서 이산화탄소는 가해준 전위에 의해 환원된다. 이로 인해, 이산화탄소는 고부가가치의 연료로 직접 전환될 수 있으며 또는 카르복실화 반응을 통해 탄화수소 반응물에 삽입 될 수 있다. 본 연구에서는 자연계의 탄소 고정 과정에서 영감을 받아 불포화 결합이 있는 탄화수소물질에 이산화탄소를 카르복실화 시키는 전기화학적 플랫폼을 새롭게 개발하였다. 본 플랫폼에서는 광합성에서 환원을 위해 화학 환원제인 NADPH를 사용하는 것을 대체하여 직접 전기에너지를 가해 환원 반응을 진행시키고자 하였으며 이를 통해 빠르고 안정적으로 대량의 연료를 생산하고자 하였다. 결론적으로 스타이렌, 다이엔, 알파 올레핀과 같은 불포화 탄화수소 원료로부터 이산화탄소와 물을 사용하여 카르복실산 연료를 생산하였다. 이러한 전기화학 플랫폼을 통해 유용한 탄화수소 연료를 이산화탄소와 물로부터 생산하는 새로운 탄소 고정 경로를 열어줄 수 있을 것으로 기대된다.

본 학위 연구에서는 지속가능한 탄소 순환을 위해 하이브리드 형태의 에너지 전환/전달 시스템을 개발하였다. 시스템의 디자인은 자연계의 광합성에 기반하였으나, 실제 구조는 생체 유기재료와 합성 재료들을 적절히 배합한 하이브리드 구조체를 사용하여 개선된 형태로 제작하였다. 이를 통해 자연계에 비해 향상된 특성과 안정성을 가지는 시너지 효과를 확인하였다. 본 연구는 광합성을 재료과학의 관점에서

깊이 이해할 뿐 아니라 이를 유용한 연료 생산 과정에 적용할 수 있는 방향을 제시하고 있다. 더 나아가 본 연구를 기반으로 광반응과 암반응을 결합한 진정한 인공 광합성을 개발할 수 있을 것으로 기대한다.

주요어: 인공광합성, 광합성, 물분해, 이산화탄소 전환, 탄소 순환, 전기화학

학번: 2013-20587